

**Using Electrons and Photons to
Estimate Passive Material Before the
ATLAS Electromagnetic Calorimeter**

by

André Hupé

A thesis submitted to the
Faculty of Graduate and Postdoctoral Affairs
in partial fulfillment of the requirements
for the degree of

Master of Science, Particle Physics

Ottawa-Carleton Institute for Physics
Department of Physics
Carleton University
Ottawa, Ontario
November 20, 2017

Abstract

The ATLAS detector is a large, general-purpose particle detector designed to observe high-energy particle collisions on the Large Hadron Collider at CERN. This study uses electrons and photons from Run 2 proton-proton collision data (2015 – 2016) to check for differences between real and simulated detector material in the region before the first layer of the electromagnetic (EM) calorimeter. The main probe is the ratio of energies deposited in the first and second layers of the EM calorimeter.

The measured material differences are compared against results from similar studies performed using Run 1 data. Deviations between Run 1 and Run 2 results are observed, primarily in regions where detector hardware was upgraded before Run 2. The material differences are well accounted for by combining the existing Run 1 material systematic uncertainties with additional Run 2 uncertainties related to the new inner tracking layer (the IBL) and the modified PP0 service region.

Acknowledgements

This thesis would not have been completed without the help of several people. I will try to name some of them:

I'd first like to thank my supervisor, Dr. Manuella Vincter. I know now, without a doubt, that next to brilliant, rigorous science, there is always room for genuine humanity. Thank you for the patience and thorough guidance. Thank you for the kindness. Thank you for this immense adventure.

I would like to thank Jaymie Maddox: Thank you for the support, thank you for the generosity, and thank you for the countless hours you've spent in an uncomfortable seat somewhere, on a bus, in a plane, or aboard a train, coming to sit up for hours with this goofy stammering boy, laughing together about our lives.

Thank you to my ATLAS office- (and occasionally room-!) mates: Graham, Steven, Rob, Stephen, Matthew, and David. Thank you for the fun conversations and good advice. Thank you to all of my friends, old and new, for keeping me sane.

Thank you to the EGamma and EGamma Calibration Groups at CERN for guiding my research and always providing helpful advice when I got stuck.

Finally, I would like to thank my family. I would certainly not be who I am today without their generous support. Thank you to my parents, Pierre and Georgina, and my sisters, Solange, Ginette, and Natasha. Thank you to my extremely cool nieces and nephews: Hudson, Lilian, Violet, Daxton, and Theo. Thank you to Anna, thank you to Willow, and last, but certainly not least, thank you to Snowball, who, despite everything, is still a very good boy.

Statement of Originality

To give context to the author's work, this thesis contains several chapters dedicated to providing an overview of the scientific field (experimental high-energy physics) and specific experimental conditions in which the research was conducted. Chapters 1 – 3 and Sections A.1 – A.3 in the Appendix use material from several published sources to summarize the necessary scientific background.

The author's original research is documented in Chapter 4. Where tables and figures are not created by the author, it is explicitly noted.

The author spent several extended periods on-site at CERN in Geneva, working in close collaboration with the ATLAS electron and photon performance group. Early results were presented to the performance group at-large at a November 2016 workshop in Thessaloniki. Regular updates were delivered in the form of short oral presentations (either in person, or when not local to CERN, over video conferencing software) to the electron and photon calibration subgroup. Results from this thesis were used to provide electron and photon calibration recommendations for physics analyses presenting results at summer 2017 conferences. Figure 37 appeared on the ATLAS electron and photon calibration poster shown at the 2017 EPS conference [1]. An ATLAS publication on the Run 2 calibration effort, which will include results from this work, is currently in production. Sections of Chapter 4 of this thesis have been assembled by the author into an ATLAS internal support note for the upcoming paper. The work presented in this thesis earned the author formal qualification as a listed author on all ATLAS publications released after the date of qualification.

This thesis is the author's original work, and documents research completed while working towards the completion of an M.Sc. degree as a graduate student at Carleton University.

Contents

Abstract	ii
Acknowledgements	iii
Statement of Originality	iv
Contents	v
List of Tables	vii
List of Figures	viii
1 Introduction	1
1.1 The Standard Model	4
1.1.1 Particles of the Standard Model	5
1.1.2 Particle Interactions	9
1.2 The Large Hadron Collider	12
1.2.1 Overview	12
1.2.2 LHC Operation	13
2 The ATLAS Experiment	16
2.1 The ATLAS Detector	16
2.1.1 Overview	16
2.1.2 Coordinate System	21
2.1.3 Subdetectors	23
2.2 The ATLAS Electromagnetic Calorimeter	29
2.2.1 ATLAS Electromagnetic Calorimetry	30
2.2.2 EM Calorimeter Geometry	33
3 Electrons and Photons in ATLAS	39
3.1 Electromagnetic Showers	39
3.1.1 Electromagnetic Interactions with Matter	39
3.1.2 Characteristics of Electromagnetic Showers	44
3.2 Electron and Photon Reconstruction	50
3.2.1 Identifying Electrons and Photons	51
3.2.2 Selection Criteria	56
3.3 Electron and Photon Calibration	61

3.3.1	Energy Reconstruction	61
3.3.2	Summary of EM Calibration	64
4	Passive Material Estimation	67
4.1	Passive Material Estimates with E_1/E_2	67
4.1.1	Layer 1 and 2 Intercalibration	71
4.2	Technique Using Distorted Geometries	72
4.2.1	Description of the Procedure Using Electrons	73
4.2.2	Description of the Procedure Using Photons	77
4.3	Description of Simulation Geometries	82
4.3.1	Nominal Run 2 Simulation Geometry	82
4.3.2	Development of "2016" Geometries	84
4.3.3	Distorted Geometry Configurations	85
4.4	Selection and Samples	88
4.4.1	Selection Criteria	88
4.4.2	Kinematic Distributions	90
4.5	Passive Material Determination with Electrons	95
4.5.1	Sensitivity Results	95
4.5.2	Passive Material Estimates	98
4.5.3	Systematic Uncertainty Checks	99
4.5.4	Results in ϕ	100
4.6	Passive Material Determination with Photons	103
4.6.1	E_1/E_2 Results	103
4.6.2	Sensitivity Results	105
4.6.3	Passive Material Estimates	108
4.7	Impact on Energy Scale Uncertainty	110
4.7.1	Material Contribution to Uncertainties	110
4.7.2	Data-Driven Uncertainties	115
5	Summary and conclusions	120
A	Appendix	123
A.1	Discriminating Variables	123
A.2	Distorted Geometry Schematics	125
A.3	Distorted Geometry $E_{1/2}$ Profiles	128
	References	134

List of Tables

1	Summary of Standard Model fermion properties	7
2	Summary of Standard Model boson properties	8
3	Summary of EM barrel calorimeter geometry	37
4	Summary of EM end-cap calorimeter geometry	38
5	Summary of presampler calorimeter geometry	38
6	Description of distorted simulation geometries	86
7	Electron selection	89
8	Radiative photon selection	90
9	Inclusive photon selection	91
10	Regions defined for the calculation of systematic uncertainties	112
11	Photon discriminating variables	123
12	Electron discriminating variables	124

List of Figures

1	ATLAS luminosity summary	15
2	Cut-away view of the ATLAS detector	17
3	Summary of pile-up in ATLAS for Run 2	20
4	Schematic of the inner detector	24
5	Dimensions of the inner detector	25
6	Cut-away view of the calorimeter systems	26
7	Cut-away view of the muon systems	29
8	Material in the electromagnetic calorimeter	31
9	Cut-away view of the ATLAS liquid argon calorimeters	33
10	Schematic of the EM calorimeter read-out plates	35
11	Representative section of the EM barrel calorimeter	36
12	Bremsstrahlung interaction	41
13	Electron energy loss in material	42
14	Photon interaction cross sections in material	43
15	Pair production interaction	43
16	Electromagnetic shower schematic	45
17	Electromagnetic shower longitudinal energy loss profile	49
18	Representative electron path through the ATLAS subdetectors	54
19	Run 1 calibration $Z \rightarrow ee$ mass peak	66
20	Run 1 simulation material budget in the inner detector	68
21	Run 1 simulation material budget up to the EM calorimeter	69
22	Shower behaviour of electrons, unconverted photons, and muons	70
23	Run 1 layer intercalibration results	72
24	Representative $E_{1/2}$ distribution	74
25	Electron $E_{1/2}$ profiles in $ \eta $ for data and nominal simulation	75
26	$p_{T,\text{truth}}$ distributions and weights for full and photon-gun simulation samples	81
27	Photon-gun example sensitivity curve	82
28	Run 1 material difference estimate	83
29	2016 candidate geometry material difference	84
30	Distorted simulation geometry material differences	87
31	Electron kinematic distributions	92
32	Radiative photon kinematic distributions	93
33	Photon p_T distributions	94
34	Relative $E_{1/2}$ difference in data and simulation as measured by electrons	96
35	$E_{1/2}$ sensitivity curve for electrons	97

36	Passive material difference estimate using electrons	98
37	Material systematic uncertainty check	101
38	2016 candidate geometry check	102
39	Material difference estimation in η and ϕ	103
40	Photon $E_{1/2}$ profiles in $ \eta $ for data and nominal simulation	104
41	Relative $E_{1/2}$ difference in data and simulation as measured by photons	105
42	Relative $E_{1/2}$ difference in distorted and nominal inclusive photon simulation samples	106
43	Relevant material differences in configuration G	107
44	Photon $E_{1/2}$ sensitivity curve	107
45	Passive material difference estimate using photons	109
46	Passive material difference estimate using electrons and photons	109
47	Data-driven uncertainties for material up to PS	117
48	Total uncertainties from Run 1 for material up to PS	117
49	Data-driven uncertainties for material up to L1	118
50	Total uncertainties from Run 1 for material up to L1	118
51	Data-driven uncertainties for material between PS and L1	119
52	Total uncertainties from Run 1 for material up between PS and L1	119
53	Distorted material schematic: s2763	125
54	Distorted material schematic: s2764	126
55	Distorted material schematic: s2765	126
56	Distorted material schematic: s2766	127
57	Distorted material schematic: s2767	127
58	Distorted geometry $E_{1/2}$ profile comparison for s2763	129
59	Distorted geometry $E_{1/2}$ profile comparison for s2764	130
60	Distorted geometry $E_{1/2}$ profile comparison for s2765	131
61	Distorted geometry $E_{1/2}$ profile comparison for s2766	132
62	Distorted geometry $E_{1/2}$ profile comparison for s2767	133

Introduction

This thesis presents work done in the context of the ATLAS Collaboration [2], one of several experimental collaborations studying high-energy particle collisions at the Large Hadron Collider (LHC) [3] at the CERN laboratory in Switzerland. The LHC accelerates protons and heavy ions to speeds within a fraction of a percent of the speed of the light, then sends the particles to collide with each other in view of several particle detectors. The detectors are used to search the remnants of the collisions for particles and phenomena that are otherwise difficult (or impossible) to observe or study in detail.

Dating back to the earliest years of its design, a major physics goal of the accelerator and the associated experiments was to observe the long-hypothesized Higgs boson [4, 5]. The Higgs boson is an important part of the *Standard Model of Particle Physics*, which summarizes our current understanding of the universe's most fundamental particles and their interactions. In the Standard Model, the Higgs boson arises out of the mechanism by which the other fundamental particles gain their masses. When the LHC was first switched-on in 2008, the Higgs boson was the last remaining Standard Model particle that had not yet been observed experimentally. With such an important role in the theory, failing to observe the Higgs at the LHC would have cast significant doubt on the validity of the Standard Model.

In 2012, a particle with mass 125 GeV and features matching the Standard Model Higgs boson was independently discovered in the LHC proton-proton collisions at two of

the experiments [6, 7]. Further investigation has not challenged the discovery. It seems clear that the Higgs boson has finally been discovered.

With the Higgs boson discovered, the LHC and its four experiments still provide an excellent laboratory for precision measurements of the Standard Model, and an undoubtedly fertile ground for the discovery of new physics. Searches are ongoing for supersymmetry, dark matter, and numerous other exotic phenomena. Where no new physics is discovered, exclusions are placed on theoretical models, creating a need for brand new solutions to the many unsolved problems that permeate modern physics. In order for these investigations to continue, the LHC detectors must be maintained and, inevitably, upgraded to improve their experimental reach for new searches.

When particles collide in the LHC (this thesis focuses exclusively on data obtained from proton-proton collisions), a number of new particles are created. These new particles propagate through the LHC detectors and leave recognizable signatures that can be used to identify particle type and measure key kinematic and energetic quantities. Measurements from the detector are inevitably distorted by imperfections in detector instrumentation. To account for this and model the effect it has on recorded data, a full Monte Carlo simulation of the detector is required.

The main idea of the work presented in this thesis is to investigate the detector as simulated in the ATLAS Monte Carlo and search for any possible discrepancies with the true geometry of the detector. Specifically, this study uses proton-proton collision data from 2015 and 2016 to check for differences in the materials that constitute the detector and its infrastructure between true and simulated detectors. The investigation is limited to material in the region between the LHC beam-line and electromagnetic calorimeter. Special emphasis is made on how these differences affect electron and photon energy calibration. The main probe used to check for material differences is the ratio of energies deposited in

the first and second layers of the electromagnetic calorimeter. Layer energy ratios resulting from both electron and photon interactions with the detector are used.

Much of the methodology for the study follows from a similar study performed after the first LHC run period (2010 – 2013) [8]. New detector components have since been introduced into ATLAS for Run 2 (2015 – today), so it was required to perform a new analysis to check for simulation material discrepancies arising from these new components. Results from the work documented in this thesis were key to determining the applicability of a number of calibration systematic uncertainties used in ATLAS results presented at summer 2017 high-energy physics conferences. The electron results were also used to confirm several improvements made to the simulation geometry for the "2016" Monte Carlo campaign and served to identify a detector support structure that was missing from the simulation geometry.

This chapter serves as an introduction, briefly outlining the Standard Model of Particle Physics and some basic principles of relativistic particle interactions. This topic is followed by a short summary of the Large Hadron Collider and its main detectors.

Chapter 2 details the ATLAS detector specifically, with an emphasis on detector geometry and material. A survey of the detector as a whole is followed by a description of each ATLAS subdetector. Special attention is paid to the electromagnetic calorimeter, which is directly relevant to the material studies performed in Chapter 4.

Chapter 3 begins with a discussion of electromagnetic showers, then moves on to describe how calorimeter showers are used to "reconstruct" electrons and photons. Standard procedures are outlined for selecting sets of reconstructed particles that satisfy physics analysis requirements. The chapter closes with a brief summary of electron and photon energy calibration in ATLAS.

Chapter 4 contains the material studies work, which represents the author's primary contribution to the material covered in this thesis. A case is made for the need of a precision understanding of detector material in simulation, followed by a description of a technique that can be used to probe for differences between real and simulated detector geometry. The set of distorted simulation samples required for the analysis is covered next, followed by an outline of the criteria used to select the particle probes. Next, estimates using electron and photon probes are presented, giving a measurement of the material differences in data and simulation. Finally, the last section shows the effect these differences have on the total calibration energy scale uncertainty of electrons and photons. The study uses data from the 2015-2016 ATLAS proton-proton collision dataset.

Chapter 5 closes with a short summary of the preceding chapters.

1.1 The Standard Model

In very broad terms, particle physicists try to understand the interactions of matter via the fundamental forces of the universe. Researchers ask: are there fundamental "units" of matter— singular elements of the universe that can't be divided into smaller, composite elements? If there are, how many of these elements are there? What are they like? How do they interact with each other to form all of the large scale phenomena we're familiar with in day-to-day life? Far from a comprehensive history of the subject, the following example of a noteworthy period of discovery in particle physics is included with the hope that it gives some context to the modern theory by showing how our picture of matter's most fundamental pieces can change over time.

After over a century of advancements in theoretical and experimental physics, researchers in the early 1960's found themselves faced with an ever-increasing number of

particles to catalogue and study [9]. Some of the particles discovered in experiments neatly confirmed predictions of theorists (the existence of the antielectron (or *positron*) for example, was proposed by Paul Dirac [10, 11] well before the announcement of its discovery in 1933 [9, 12]). Many more, though, came as a surprise. With no reason to believe otherwise, newly-discovered particles were assumed fundamental and added to the growing set of apparently indivisible particles. The long list of "fundamental" particles was famously dubbed the *particle zoo*. Seeking a better understanding of these widely-varying, unexpected particles, many physicists sought to find any kind of symmetry or sign of higher-order structure within the zoo. Several particles were successfully grouped by shared interaction behaviours and properties like charge or intrinsic spin, but the origin of these qualities remained a mystery.

An appealing solution to the problem was provided by the introduction of *quarks* [13, 14]. The quark model posited that the majority of particles under investigation weren't indivisible after all, but instead, they were composite particles made of various combinations of just a few fundamental quarks. Controversial at first, quarks now form a significant part of the widely-accepted *Standard Model* of Particle Physics, which is the theory describing the consensus understanding of all known fundamental particles and their interactions. Also in the model are *leptons* (like the electron) and the force-carrying *bosons* (like the photon). The particles of the Standard Model are described in Section 1.1.1. Section 1.1.2 then briefly introduces some important ideas about how we study the interactions between these particles.

1.1.1 Particles of the Standard Model

Fundamental particles in the Standard Model can be divided into two categories: fermions (which include quarks and leptons, forming the fundamental substructure of matter) and

bosons (which are involved in the mediation of forces between particles). Standard Model fermions have an intrinsic spin of $1/2$, while bosons have an integer spin (0 or 1). The fermions are summarized in Table 1, and the bosons are summarized in Table 2.

Fermions in the Standard Model come in three generations. Particle mass generally increases with generation number (so the first generation particles are the least massive, and the third generation particles the most massive.) There are six quarks (two in each generation) and six leptons (again, with two in each generation). The three generations of quarks are *up* and *down* quarks (first generation), *charm* and *strange* quarks (second generation), and *top* and *bottom* quarks (third generation). The "up"-type quarks (up, charm, and top) have a charge of $+2/3e$ (where e is the elementary charge $e = 1.602 \times 10^{-19}$ C), and the "down" type quarks (down, strange, and bottom) a charge of $-1/3e$. Quarks carry a *colour* charge (one of three: red, green, or blue), which plays a significant role in their interactions. Each quark has a corresponding antiparticle with the opposite set of charges.

Quarks are never found in isolation. They combine to form composite particles called *hadrons* (these hadrons forming the bulk of the previously mentioned "particle zoo"). Laws that govern quark interactions restrict the kinds of hadrons that are allowed. Two kinds of hadrons are observed: baryons, which are composed of three quarks, and mesons, which contain just a quark and an antiquark. Important examples of baryons are the proton (two up quarks and one down quark) and the neutron (one up quark and two down quarks). The positively charged pion π^+ (an up quark and an anti-down quark) and its antiparticle π^- (an anti-up quark and a down quark) are examples of light mesons built from up and down quarks.

The remaining fermions are leptons. The three charged leptons (with a charge of $-e$) are the electron, muon, and tau. Each lepton has a corresponding neutrino, which is uncharged and has a small but nonzero mass. The muon and the three neutrinos are significantly more

Table 1: The Standard Model fermions: three generations of quarks and leptons. In all cases the particles have a spin of $1/2$. All particles have antiparticle partners which are not shown here. Quark masses cannot be measured directly and their determination is not trivial. Masses quoted in the table are taken from the 2016 Particle Data Book [15], given to three significant figures in natural units ($c = \hbar = 1$) without uncertainties. Note the frequent changes in mass units (eV– GeV). Neutrinos propagate in mass states that are superpositions of several flavour (e, μ, τ) states. The absolute scale of the neutrino masses is not known, so they are listed as small (eV scale) but non-zero.

Quarks		
1 st Generation	2 nd Generation	3 rd Generation
Up (u) Charge: $2/3e$ Mass: 2.15 MeV	Charm (c) Charge: $2/3e$ Mass: 1.28 GeV	Top (t) Charge: $2/3e$ Mass: 173 GeV
Down (d) Charge: $-1/3e$ Mass: 4.70 MeV	Strange (s) Charge: $-1/3e$ Mass: 93.8 MeV	Bottom (b) Charge: $-1/3e$ Mass: 4.18 GeV
Leptons		
1 st Generation	2 nd Generation	3 rd Generation
Electron (e) Charge: $-e$ Mass: 0.511 MeV	Muon (μ) Charge: $-e$ Mass: 106 MeV	Tau (τ) Charge: $-e$ Mass: 1.78 GeV
Electron Neutrino (ν_e) Charge: 0 Mass: $\sim eV$	Muon Neutrino (ν_μ) Charge: 0 Mass: $\sim eV$	Tau Neutrino (ν_τ) Charge: 0 Mass: $\sim eV$

penetrating that the electron (i.e. they are less likely to experience interactions with matter as they pass through it). At current energies available to experiments, this has a significant effect on how well a detector can record the passage of these particles [15].

The remaining fundamental particles are bosons. In the Standard Model, bosons mediate three of the four fundamental forces of nature: the electromagnetic force, strong nuclear force, and weak nuclear force. The fourth force, gravity (the weakest of the fundamental forces), is not encompassed by the Standard Model. No mediating particle has yet been discovered¹. The electromagnetic force is mediated by the *photon* (commonly

¹ General relativity, the dominant modern theory of gravity, requires that the particle mediating the gravitational force is a massless spin-2 boson. Particles posited to mediate the force of gravity are commonly dubbed the *graviton* [16, 17].

Table 2: The Standard Model bosons [9, 15]. These bosons are the carriers of three of the four fundamental forces: electromagnetism, the weak nuclear force, and the strong nuclear force. The fourth (and weakest) force, gravity, is not accounted for by the Standard Model.

Bosons		
Particle	Properties	Force Mediated
Photon (γ)	<i>Spin</i> : 1 <i>Charge</i> : 0 <i>Mass</i> : 0	Electromagnetic
Gluon (g)	<i>Spin</i> : 1 <i>Charge</i> : 0 <i>Mass</i> : 0	Strong Nuclear Force
W^\pm	<i>Spin</i> : 1 <i>Charge</i> : $\pm e$ <i>Mass</i> : 80.4 GeV	Weak Nuclear Force
Z	<i>Spin</i> : 1 <i>Charge</i> : 0 <i>Mass</i> : 91.2 GeV	Weak Nuclear Force
H	<i>Spin</i> : 0 <i>Charge</i> : 0 <i>Mass</i> : 125 GeV	-

represented by the character γ). The strong force is mediated by the *gluons* (g), which come in eight varieties, each differing in their colour content. Colour physics defines the set of interactions gluons can participate in, so they interact exclusively with other particles that carry a colour charge (quarks and other gluons). Unlike the massless photon and gluon, the three bosons involved in weak force, the Z, W^+ , and W^- , all have a large, non-zero mass. The W^\pm bosons are a particle/antiparticle pair.

The Higgs boson (which also has a large mass) is the most recently discovered particle in the Standard Model. Unlike the other fundamental bosons, the Higgs boson does not mediate a force. The Higgs boson is introduced to the Standard Model as a consequence of electroweak symmetry breaking, the mechanism by which all of the massive fundamental particles gain their mass [9, 18, 19].

1.1.2 Particle Interactions

The way particles interact with one another is a crucial component of the Standard Model. Particles may scatter elastically in a simple exchange of kinetic energy. They can also interact with one another to generate a set of new particles, or decay spontaneously into lighter particles.

Every interaction (or decay) involves at least one of the fundamental bosons. The set of possible interactions are limited to those which satisfy a number of symmetries in nature. (Symmetries lead, via Emmy Noether's famous theorem [9, 18], to familiar conservation principles like the conservation of energy, or the conservation of electric charge.)

For instance, a fairly common process is the annihilation of an electron with its corresponding antiparticle, the positron. Since the electron and positron have opposite charges, the net charge before the annihilation is zero. Conservation of electric charge then requires that the final products of the annihilation have a net zero electric charge. The case where the annihilation produces photons will be considered here. Since photons travel at the same speed in every reference frame (this is one of the postulates of special relativity), the conservation of linear momentum requires the production of at least two photons². The process can be written as $e^- + e^+ \rightarrow \gamma + \gamma$.

Conservation of energy places further requirements on the kinematics of the final particles. For each particle in the interaction, the total energy of the particle E is given by

² This follows from the fact that it is always possible to define a frame of reference where two particles have a combined momentum of zero. Working in the frame where the initial particles have zero net momentum, the net momentum in the final state (after the annihilation) should have zero net momentum as well. One possible solution to this is a single stationary particle. Since the speed of light is the same (and definitely non-zero) in all reference frames, a single photon is not a permitted final state. At least two photons are required to allow for the cancellation of momentum in every direction, resulting in zero net momentum overall.

the relation:

$$E^2 = |\vec{p}|^2 c^2 + m^2 c^4, \quad (1)$$

where \vec{p} is the particle's momentum and m is the rest mass. The speed of light constant c appears twice here and in many other frequently used equations in particle physics, so it is common to work in "natural units", where $c = \hbar = 1$. Rewriting the equation in natural units yields:

$$E^2 = |\vec{p}|^2 + m^2. \quad (2)$$

It can be seen from this equation that, working in natural units, both mass and momentum can be expressed in units of energy. Values are normally given in electronvolts ($\text{eV} \approx 1.6 \times 10^{-19} \text{ J}$) and associated units (keV, MeV, etc.). Natural units are used throughout this document unless stated otherwise.

In the center of momentum frame of the electron and positron, the two initial particles have the same energy: $E_e = \sqrt{|\vec{p}_e|^2 + m_e^2}$. The total energy available for the production of new particles, then, is $2E_e$. (Since energy is conserved, this means that each of created photons also has energy E_e .) If particle momentum is increased, more energy is available for the production of new particles after the annihilation occurs. In the electron-positron example, one of the requirements for the resulting particles is that the net-zero electric charge is conserved. This is satisfied by a number of processes, like $e^- + e^+ \rightarrow Z$ or $e^- + e^+ \rightarrow W^+ + W^-$, for example. (Interactions often proceed via a number of intermediate steps, which are governed by conservation laws that are not detailed here.) The W and Z bosons are quite heavy (see Table 2), so the initial particles must be accelerated significantly to ensure that there is enough energy available for their production (recall that Equation 2 contains a mass term).

This is the basic principle by which a particle collider operates. Particles are accelerated to extremely high energies, then sent into collision at various interaction points. The

interaction points are equipped with sophisticated particle detectors to observe the particles created during the collision. Many of the high-energy particle colliders built for physics research in the last century were electron-positron (e^+e^-) colliders, their design based on many of the principles of e^+e^- interaction given here as examples. Other accelerators collide much heavier particles. The Large Hadron Collider at CERN, which is the focus of this thesis, collides proton pairs or heavy ions such as lead nuclei.

Protons are composite particles, so colliding pairs of protons can involve interactions between individual constituent particles in each proton. This leads to a number of additional challenges that aren't encountered with lepton colliders. To name one: proton-proton interactions depend considerably on the distribution of the proton's total momentum among the constituent quarks and gluons, making them more difficult to model than interactions between the point-like electrons and positrons. Additionally, the presence of strong-force processes between quarks and gluons leads to events that are, on average, more complicated than e^+e^- events. This can make it more challenging to extract any signal of interest from the collision products. Despite these complications, hadron colliders are often preferable to lepton colliders, especially at the energy frontier. Electrons lose significant amounts of energy when accelerating. The proportion of energy lost increases dramatically with the energy of the particle, making them poor choices for very high-energy circular accelerators [20]. Using hadrons also has the effect of greatly increasing the frequency of colour interactions, increasing the likelihood of observing events that rarely occur as the result of e^+e^- collisions.

1.2 The Large Hadron Collider

1.2.1 Overview

The Large Hadron Collider is a particle accelerator and collider located at CERN along the border of France and Switzerland, near Geneva. Housed approximately 100 metres underground in the 26.7 km long circular tunnel that originally contained the LEP (Large Electron-Positron) collider [21], the LHC accelerates beams of protons and heavy ions to TeV-scale energies before colliding them at the heart of several large particle detectors.

At LHC design specifications, two proton beams are accelerated in opposite directions around the ring to an energy of 7 TeV, yielding collisions with a combined 14 TeV center of mass energy at a luminosity³ of $10^{34} \text{ cm}^{-2}\text{s}^{-1}$. The LHC boasts the highest yet achieved energy in a particle collider, significantly improving on the previous record (set by the Tevatron [22] at Fermilab, which ran protons and antiprotons at a beam energy of approximately 1 TeV).

Protons for the collision are injected into the LHC having already been accelerated to an energy of 450 GeV by a series of smaller accelerators. Throughout the accelerator chain, the proton beams are contained in a beam-pipe under ultra-high vacuum. This is required to minimize particle interactions prior to the intended collision. Once in the ring, "Radio-Frequency" (RF) cavities continue accelerating the protons up to their maximum speed. Steering around the LHC ring is accomplished using more than one thousand 15 m long superconducting dipole magnets. Other sets of magnets precisely focus the proton beam, which is necessary for collisions to occur.

³ Luminosity is used as a measurement of how frequently events of interest are produced in particle collisions. Multiplying the interaction cross section (a measure of the probability for the process to occur) by the luminosity yields the number of times that an interaction is expected to occur over an interval of time (one second, with the units given).

Protons travel around the ring and collide in "bunches" containing a large number of particles (on the order of 10^{11} [3]). When bunches from the opposing beams cross at the interaction point, only a small fraction of the protons interact. Of those that interact, an even smaller subset is likely to have interacted in a way that might produce an interesting signal. The majority of protons will experience "glancing blows", where the protons simply deflect via mutual repulsion due to their like-charges. These are elastic collisions, where the only effect of the interaction is to modify each particle's kinetic energy such that the net kinetic energy remains the same. In "hard-scatter" interactions, the constituent quarks and gluons of each proton interact directly. The energy is "lost" to the creation of new particles (making these inelastic collisions) which are possible candidates for new or interesting physics.

Four primary detectors are situated at interaction points around the LHC ring where the particle beams collide. Two of the detectors, ATLAS (A Toroidal LHC ApparatuS [2]) and CMS (Compact Muon Solenoid [23]), are enormous "general-purpose" detectors, designed to capture as complete a picture of the collision as possible. LHCb (LHC beauty [24]) is specifically designed for b-quark (bottom, or "beauty" quark) physics. b-quark physics is a popular avenue for investigating charge-parity (CP) violation, which may offer hints into the problem of matter-antimatter asymmetry in the universe. The last of the four detectors, ALICE (A Large Ion Collider Experiment [25]), is designed primarily for observing heavy-ion collisions. The ALICE physics program has a strong emphasis on colour physics, particularly the quark-gluon plasma phenomenon.

1.2.2 LHC Operation

The LHC has so far seen two data-taking periods: "Run 1", which ran from 2010 to 2013 (with the bulk of the collisions occurring in 2011 and 2012), and "Run 2", which began in 2015 and is scheduled to continue through until the end of 2018. The superconducting

magnets that steer particles around the LHC ring need to be "trained" with increasing currents before they can operate at their designed strength. As a consequence of the time required for training the magnets, collisions in Run 1 were performed at reduced energies relative to the design value. The center of mass energy of 7 TeV (or 3.5 TeV per proton beam) was used for 2010 and 2011 operation. This was increased to 8 TeV in 2012.

During the "long shutdown" period between Run 1 and Run 2, the LHC and its four detectors were serviced and a number of upgrades were installed to improve performance. In 2015, the LHC began colliding protons at 13 TeV, the center of mass energy used throughout Run 2. In 2016, the bunch spacing (i.e. the time between successive beam bunch crossings) was reduced to 25 ns, half of the 50 ns value used in 2015 and all of Run 1. Although this results in a "messier" interaction point (see Section 2.1.1 for a description of *pile-up*) it has the effect of increasing the luminosity, which is useful for observing rare processes. The luminosity was further increased throughout Run 2. The top plot in Figure 1 shows the luminosity throughout 2016 as read by the ATLAS detector. The peak luminosity, $1.38 \times 10^{34} \text{ cm}^{-2}\text{s}^{-1}$, exceeds the design value of $10^{34} \text{ cm}^{-2}\text{s}^{-1}$. The increased luminosity in Run 2, combined with excellent LHC and detector uptime, resulted in a significant increase in yearly integrated luminosities compared to Run 1 (see bottom plot in Figure 1).

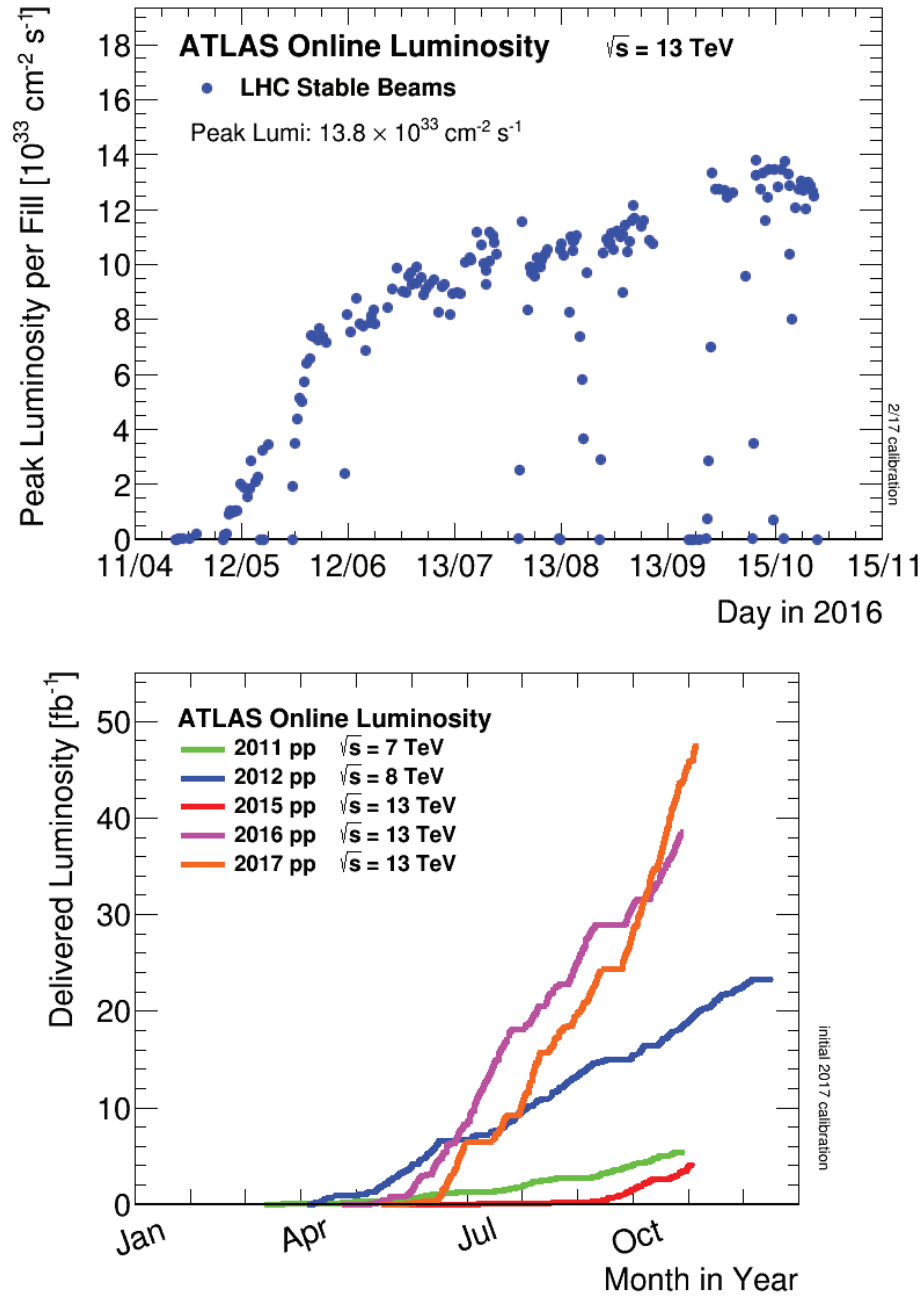


Figure 1: **Top:** Peak luminosity per fill as recorded by ATLAS throughout 2016. The luminosity regularly exceeded the design value of $10^{34} \text{ cm}^{-2} \text{ s}^{-1}$. **Bottom:** Integrated luminosity for all Run 1 and Run 2 ATLAS proton-proton data-taking up to November 2017. Both figures from [26].

The ATLAS Experiment

The ATLAS detector is one of two general-purpose particle detectors designed for the study of the proton-proton and heavy-ion collisions generated by the LHC. This chapter begins with an overview of the detector and a brief survey of its numerous subdetectors, then moves into a more thorough discussion of the system most relevant to the material studies performed in this work: the electromagnetic calorimeter.

2.1 The ATLAS Detector

2.1.1 Overview

Assembled underground on the LHC ring in a large cavern at the CERN Meyrin site, the ATLAS detector is a large, multi-layered particle detector containing several calorimeters, semiconductor charged particle trackers, superconducting magnets, and more, weighing in altogether at approximately 7000 tonnes. Installation of the detector was completed in 2008 after more than a decade of work from thousands of scientists, engineers, students, and technicians collaborating internationally [2]. The detector surrounds one of four interaction points on the LHC with a roughly cylindrical geometry (25 m in diameter and 44 m in length, see Figure 2) containing a number of detection systems that are used to collect as much information about the collisions as possible. Designed, along with CMS, with a broad set of physics goals in mind, the detector is probably most well-known for its role in the previously mentioned 2012 discovery of the Standard Model Higgs boson [6]. Since then,

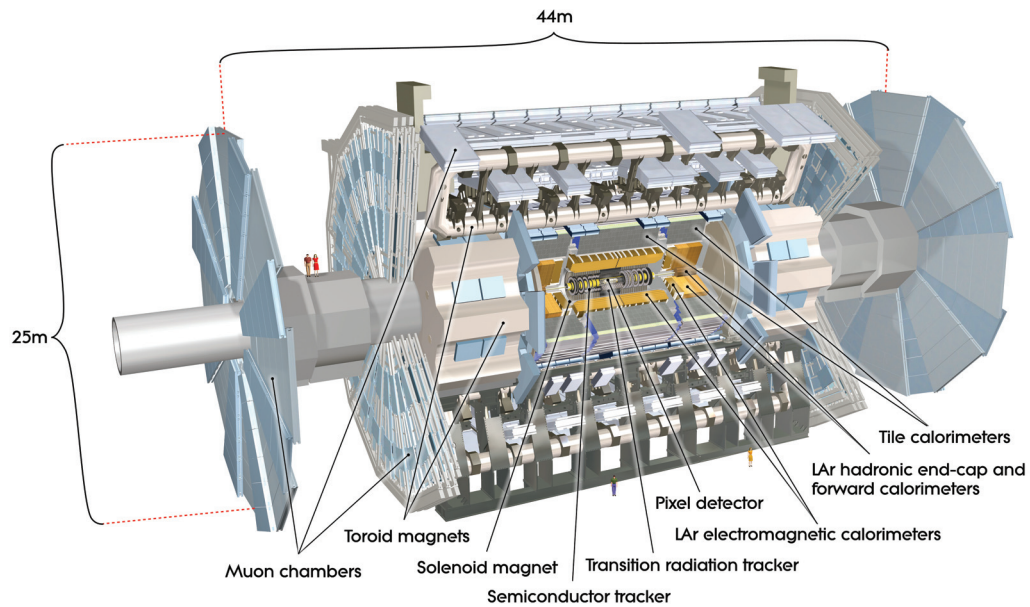


Figure 2: Cut-away three-dimensional schematic of ATLAS, showing the detector's scale and numerous subdetectors. Figure from [2].

the detector has continued collecting data with several upgrades to detector hardware (and the suite of associated software tools necessary for data analysis), at the significantly higher Run 2 collision energy. The search for new physics continues.

In order to capture a reasonably complete picture of the proton-proton collisions produced by the LHC, the ATLAS detector needs to measure the energies and trajectories of a wide variety of particle types, both charged and uncharged, with energies that span from 100s of MeV up to a few TeV. This is accomplished by layering several subdetectors around the interaction point, each designed to track the trajectory or measure the energy of most of the particles emanating from the LHC collisions. The major subdetectors are described in Section 2.1.3.

The detector offers nearly full 4π solid angle coverage for energy measurement, coupled with a large precision charged particle tracking volume in the central region. Several theoretical models predict the existence of particles that would have low interaction cross-

sections with matter and so would likely escape the detector without being measured. This means that "new physics" models often predict significant amounts of *missing energy* as observed by ATLAS. Without hermetic coverage, there would be no way to total up the energies of all particles produced in a collision and check for evidence of something gone missing. Thus it is an important design goal to capture as much of the energy of a collision as possible. Despite good solid angle coverage, a certain amount of lost energy is expected due to small gaps in subdetector systems and the creation of highly penetrative Standard Model particles like neutrinos, which can carry non-negligible amounts of energy and always escape the detector without registering a signal. Energy may also be lost as particles continue down the beam-pipe, invisible to any subdetectors. These effects must be taken into account when searching for new physics via missing energy.

The Trigger

At design luminosity, proton-proton interactions in the LHC occur at a rate of about 1 GHz, which far exceeds the detector's read-out and storage rate capabilities. Most of these interactions are relatively mundane; the cross sections for many of the most interesting "new physics" interactions are small, so they occur relatively infrequently. A *trigger* system is used to quickly save events that are likely-candidates for containing interesting physics processes, reducing the final rate of data-taking. Updates to the trigger system during the long shutdown between Run 1 and Run 2 increased the average final output rate of the trigger from the Run 1 value of 400 Hz to ~ 1 kHz (as reported during 2015 data taking) [27].

The trigger functions in two steps (reduced from three in Run 1): the Level 1 (L1) trigger and the High-Level Trigger (HLT). In a nutshell, the hardware-based L1 trigger (located on or very near the detector) searches for coarse "regions of interest" in the calorimeters (which measure particle energy) or muon systems for signals that are suggestive of events relevant to the ATLAS physics program. The L1 trigger also selects events with a significant amount

of missing energy. Events that satisfy the L1 trigger requirements are passed through to the HLT, which checks events against a more sophisticated set of criteria using the full detector granularity. Events that pass the HLT are stored and sent for further processing for use by physics analyzers. (The trigger is quite complicated; this section summarized the L1 and HLT in very brief detail only. See e.g. [2, 27, 28] for more information.)

Pile-up

The LHC collides bunches of protons instead of single particles to increase the chances of hard-interactions between the two beams. It is common for multiple interactions to occur during the same bunch crossing. Since multiple collisions happen at the same time (known as *pile-up*), and the chances of an interesting (or "relevant to the physics goals of the experiment") collision are less than an uninteresting one, events that pass the trigger requirements typically contain signals from a number of background collisions. It is crucial to distinguish signal from the interesting, hard-scatter collisions from the background pile-up signals. Techniques for doing this on an analysis level are described in Section 3.2.2. Figure 3 shows the number of interactions per crossing from two years of Run 2 operation.

Pile-up from interactions occurring within the same bunch crossing is referred to as "in-time pile-up". In some cases, pile-up interference is caused by particles from neighbouring bunch crossings. This is likely to occur when, for instance, a detector component has a signal-integration period (i.e. the time it takes for a signal to propagate through the detector and its electronics) significantly longer than the 25 ns bunch spacing. This is the case for a number of the subdetectors [29] (the electromagnetic calorimeter, for example, has a signal integration time on the order of several hundred ns [30]), so this effect, called "out-of-time pile-up", should also be accounted for.

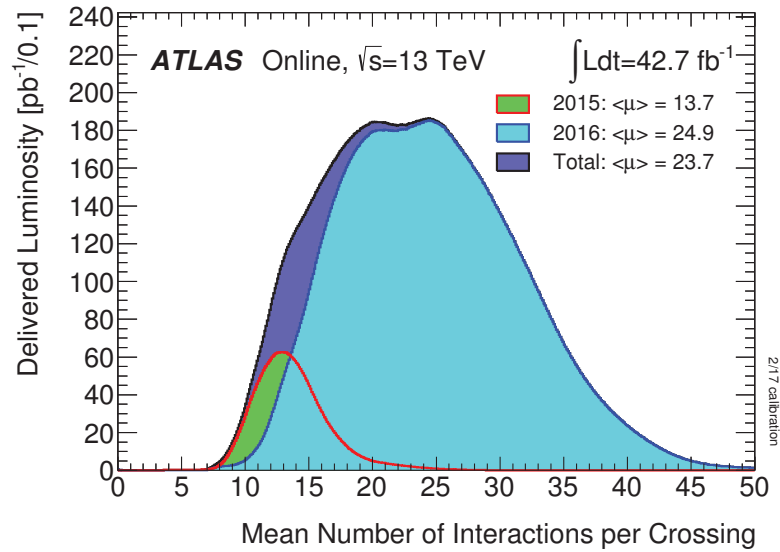


Figure 3: Pile-up rates over two years of ATLAS Run 2 operation. The number of interactions per crossing (x-axis) is typically given by μ , so the mean values $\langle \mu \rangle$ in the legend give the average pile-up over a given time span. Figure from [26].

Monte Carlo Simulation

A full simulation is necessary to interpret detector response. The ATLAS Monte Carlo simulation [31] is based on a set of event generators which feed proton-proton physics events into a full Geant4 [32] simulation of the detector. The simulation includes the full suite of subdetectors, pile-up effects, and read-out electronics to model the experimental conditions at ATLAS as closely as possible. The simulation can be output into a format identical to the read-out format of the detector, so that trigger and particle "reconstruction" (i.e. grouping detector signal patterns into physics objects like particles and determining their kinematic properties) algorithms can be applied identically to the simulated interactions and real, observed data from the detector. The simulation chain can be very broadly broken down into three steps:

- **Event generation/detector hits:** Physics events are generated (proton-proton collisions and all immediate decays), usually using a combination of external Monte Carlo

generators. The events propagate through the detector in a Geant4 simulation, and the interactions with detector material are stored as detector hits.

- **Digitization:** The simulated detector hits are digitized, simulating the real read-out process. A number of additional corrections are applied here, like accounting for pile-up or detector regions with temporary status issues.
- **Reconstruction:** Detector signals are converted into software particle objects for use in analysis. This is covered in some detail for electrons and photons in Section 3.2.

Particles from simulation are tagged with two kinds of kinematic/energetic quantities. "Reconstructed" quantities are the values as measured by the detector and determined from reconstruction algorithms. "Truth" quantities are the values as determined by the event generators and Geant4 simulation. The reconstructed quantities are useful for comparing with quantities measured from real data. Truth quantities are crucial to understanding the detector response and reconstruction algorithm performance, since a perfect detector and object reconstruction technique would consistently reconstruct the true values of a particle's energy and trajectory. Since no detector is perfect, the differences between reconstructed and truth values are carefully studied and either corrected for as best as possible, or taken as experimental uncertainties.

2.1.2 Coordinate System

Given the geometry of the ATLAS detector, it is useful to work in a cylindrical coordinate system. The z -axis is defined along the beam-line with the origin at the center of the detector at the nominal interaction point. ATLAS is designed to be symmetric about $z = 0$, with the symmetric halves of the detector referred to as the "A-" (positive z) and "C-" (negative z) sides of the detector. The remaining cylindrical coordinates are useful as well: r , the

distance away from the beam-line, and ϕ , the azimuthal angle around the beam-line. Many subdetectors are approximately uniform in ϕ . The polar angle θ away from the beam-line (in the positive z direction) is occasionally used as well.

A common quantity in high-energy physics is the *rapidity*:

$$y = \frac{1}{2} \ln \frac{E + p_z}{E - p_z}. \quad (3)$$

Differences in this quantity are invariant under Lorentz boosts in the z -direction (unlike the polar angle, which is not). This makes it very useful for hadronic accelerator conditions where the energies of the colliding protons are variably distributed to the proton's constituent partons, shifting the collision center-of-mass frame away from the detector frame [33]. Calculating this quantity requires full knowledge of an object's four-momentum (i.e. the total energy and momentum in three cartesian directions), which can be difficult or impractical to calculate for every particle produced in a collision. For light, high-energy objects, the expression for rapidity simplifies to a function of θ alone. This quantity is the *pseudorapidity*, denoted as η :

$$\eta = -\ln \tan \frac{\theta}{2}. \quad (4)$$

This quantity is frequently used as a detector coordinate in place of θ . η is zero in the $z = 0$ plane. Moving away from the $z = 0$ plane (down towards the beam-line), $|\eta|$ increases: at an angle of $\pi/6$ radians (30°) away from the $z = 0$ plane, $|\eta| \approx 0.549$, and at an angle of $\pi/3$ radians (60°) away from the $z = 0$ plane, $|\eta| \approx 1.317$. As the angle away from the $z = 0$ plane approaches $\pi/2$ radians (90° , i.e. running parallel to the LHC beam-line) $|\eta|$ tends towards infinity. A two-dimensional area in (η, ϕ) space defined by intervals $\Delta\eta$ and $\Delta\phi$ is commonly defined as $\Delta R = \sqrt{\Delta\eta^2 + \Delta\phi^2}$.

With the coordinate system origin at the nominal interaction point, the two Cartesian

coordinates x and y (positive x directed towards the centre of the LHC ring, and positive y directed upwards) define a transverse plane orthogonal to the z -axis and beam-line. Since the net momentum in the transverse plane is expected to be zero, it is typical to consider energy and momentum in this transverse plane (E_T and p_T , respectively).

2.1.3 Subdetectors

ATLAS consists of many smaller subdetectors. They mostly can be divided into three classes, each with a different purpose: the **inner detector** is used for general precision charged particle tracking, the **calorimeters** destructively measure the energy of particles, and the **muon spectrometer** records the passage of muons. For practical reasons (ease of construction, assembly, and detector maintenance), detector systems in general tend to be broken into a *barrel* section, which is coaxial with the beam-line and centered on the nominal interaction point, and two *end-cap* sections, which extend the pseudorapidity coverage of the detector with (typically) disk or wheel shaped sections oriented perpendicular to the beam-line. These subdetectors are also complimented by a number of smaller detector components, used for special purpose measurements (e.g. recording luminosity, or observing particles passing through small gap regions between subdetectors).

Inner Detector

The inner detector (ID) is a set of four subdetectors used for the precision tracking of charged particles. Crucial to the operation of the trackers in the ID is a large 2T solenoid magnet that encloses the region and bends (charged) particle trajectories, allowing for momentum measurement. The pseudorapidity coverage of the innermost layers of the ID, $0 < |\eta| < 2.5$, defines the "precision measurement" region for ATLAS [2]. Figure 4 shows three of the ID subdetectors in detail: the pixel detector, the semiconductor tracker (SCT), and the

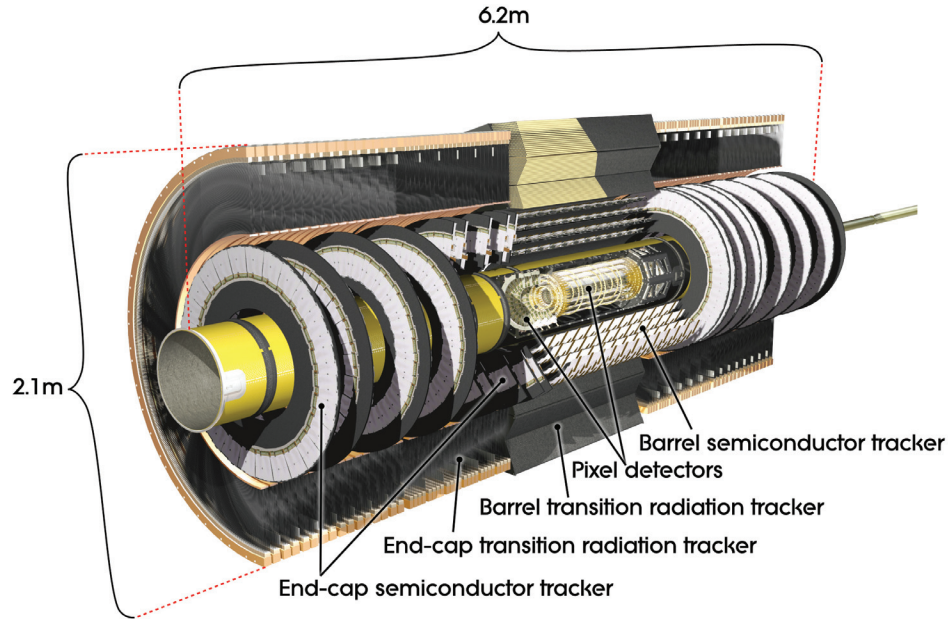


Figure 4: Schematic showing some of the inner tracking detectors. The insertable B-layer is not shown here. Note the relative diameter of the beam-pipe, visible at the far right side of the image. Figure from [2].

transition radiation tracker (TRT). Not shown is the insertable B-layer (IBL), which was added between the pixel detector and the beam-pipe in the long shutdown period between Run 1 and Run 2 [34]. Figure 5 shows several of the detectors in more detail, emphasizing their position relative to the beam-line and nominal interaction point.

The IBL, pixel detector, and SCT are silicon tracking detectors, designed to register the passage of a particle through the detector while minimizing any significant loss of the particle's energy. The barrel pixel detector covers $|z| < 400.5$ m and is comprised of three concentric layers of fine-grained silicon modules. To give an idea of the granularity of the detector, each barrel layer is composed of several hundred $16.4 \text{ mm} \times 60.8 \text{ mm}$ modules, each of which contains over 46,000 pixels of size $50 \mu\text{m} \times 400 \mu\text{m}$ [35]. The small pixel size results in a position resolution for a given module of $12 \mu\text{m}$ for particles at normal incidence (as measured in test-beam experiments) [2]. The closest layer to the beam-line is located at radial distance $r = 50.5$ mm; the furthest layer at $r = 150$ mm. The IBL falls

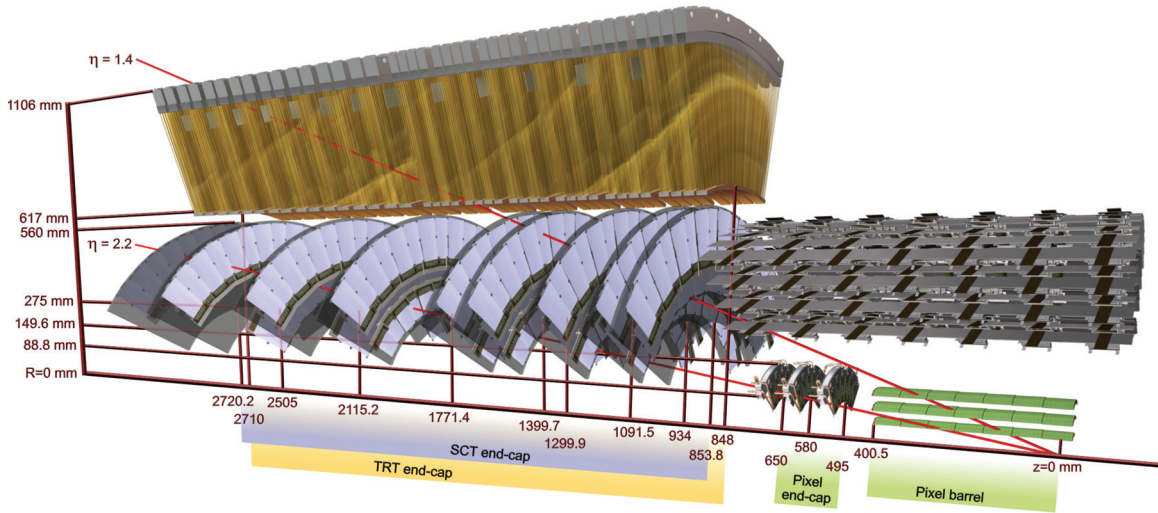


Figure 5: Several elements of the inner detector are shown here along with their positions relative to the nominal interaction point (and coordinate origin), shown in the bottom right corner of the image. The IBL and barrel TRT are not shown. Two example pseudorapidity rays, $\eta = 1.4$ and $\eta = 2.2$, are shown emanating from the origin. Figure from [2].

even closer to the beam-line, with an average radius of $r = 33$ mm, effectively functioning as a fourth layer of the pixel detector [34]. A pixel end-cap detector (of which there are two) consists of three silicon module disks oriented perpendicular to the beam-line, extending the coverage of the pixel detector out to cover the rest of the precision measurement region.

The SCT is arranged similarly to the pixel detector: four cylindrical barrel layers of silicon detectors surround the beam-line at the nominal interaction point, and two end-caps (each containing nine disks) extend the coverage of the detector out to $|\eta| = 2.5$. Each layer and disk contains strip silicon modules arranged in pairs. Modules in a pair are oriented at slight angles relative to each another, providing a stereo (two-dimensional) measurement.

Unlike the other trackers in the inner detector, the TRT is not a silicon detector. The bulk of the TRT is comprised of a large array of straw drift tubes, running parallel to the beam-line in the barrel TRT and radially in the end-cap TRT. A charged particle moving within pseudorapidity coverage of the TRT ($|\eta| < 2$) and with sufficient energy can easily cross 30 (or more) straws [35], providing a significant number of detector hits for track

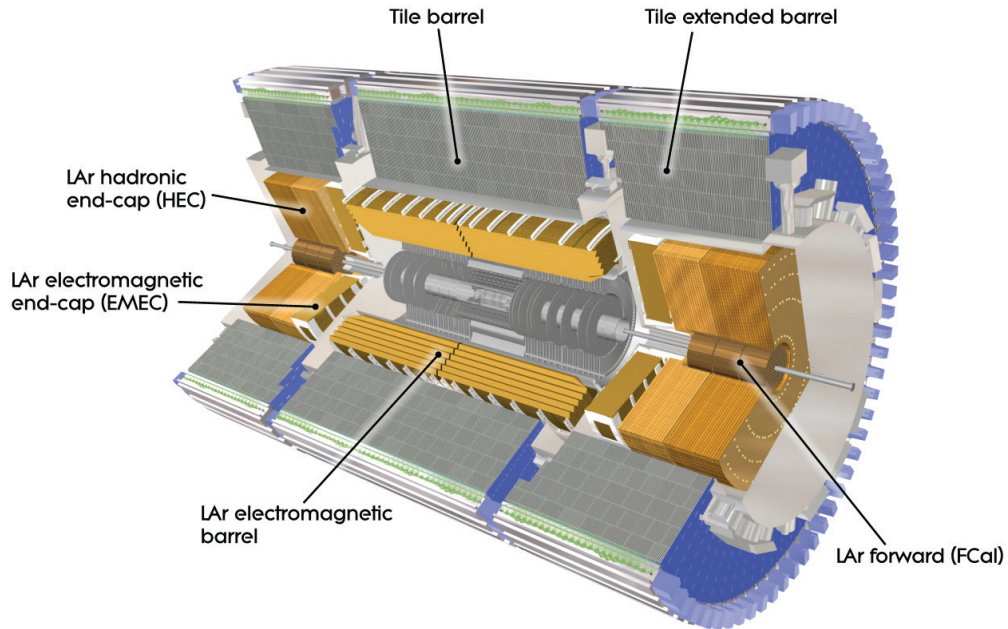


Figure 6: Calorimeters in ATLAS. The figure shows the three calorimeter systems: electromagnetic (liquid argon barrel and end-caps), hadronic (tile barrel sections and liquid argon end-caps), and forward (one electromagnetic and two hadronic sections, all of which use liquid argon as the active medium). Figure from [2].

reconstruction. The area between straws in the TRT contains polypropylene material, which causes the emission of transition radiation when a charged particle passes through with enough energy. In transition radiation detectors, the amount of energy emitted depends strongly on γ (unlike many other particle detectors, which depend on β [36]), making the TRT critical for electron identification in ATLAS⁴ [37].

Calorimeters

Surrounding the solenoid magnet and inner detector are the calorimeters (see Figure 6).

ATLAS has three calorimeter systems: the electromagnetic calorimeter (or "EM calori-

⁴ $\beta = v/c$ and $\gamma = \frac{1}{\sqrt{1-v^2/c^2}}$ are common quantities in special relativity. For massive particles, the Lorentz factor γ can be used to relate the total energy of a moving particle to its rest mass: $E = \gamma m_0$ (in natural units). Consider an electron and a negatively charged pion with the same total energy $E = 10$ GeV. With rest masses $m_{0,e} \approx 0.511$ MeV and $m_{0,\pi^-} \approx 140$ MeV, the Lorentz factors can be calculated: $\gamma_e \approx 19600$ and $\gamma_{\pi^-} \approx 71.4$. Thus, with a detector response that depends strongly on γ , electrons and pions will leave easily distinguishable signal patterns.

meter"), the hadronic calorimeter, and the forward calorimeter. In all three cases, the role of the calorimeter is to measure the energy of particles via the creation of particle showers. All of the calorimeters in ATLAS are sampling calorimeters that operate on very similar principles. Showers are initiated with a *passive* heavy absorber material, and the energy of the shower is sampled with an *active* sampling material. This is described in more detail in Section 2.2, which covers the electromagnetic calorimeter in detail, and in Section 3.1, which is focused on the physics of electromagnetic showers.

Most of the Standard Model particles produced in ATLAS do not make it past the calorimeters. Exceptions to this are muons, which are measured by their own system located beyond the calorimeters, and neutrinos, which are very difficult to observe and are not expected to interact with the detector. Altogether, the calorimeters offer energy measurement coverage over the pseudorapidity range $0 \leq |\eta| < 4.9$.

The first calorimeter layer is the **electromagnetic calorimeter**, which uses alternating layers of lead to initiate electromagnetic showers and liquid argon (LAr) to sample the energies of electrons and photons. Sampled energies are translated into original particle energies using detector response information from previous test-beam experiments. Together, the barrel and end-cap EM calorimeters cover $0 \leq |\eta| < 3.2$. The calorimeter is segmented in η and ϕ , providing the means to measure shower size and position and, if necessary, tie calorimeter signals back to ID tracks. The calorimeters are housed inside a set of large cryostat vessels, which are necessary for the use of liquid argon.

The hadronic calorimeters in ATLAS are more varied. The **hadronic tile calorimeter** is located immediately behind the EM barrel and end-cap calorimeters in the r direction. Hadronic showers (or jets) are initiated by particles moving through steel in the calorimeter. The shower particles pass through scintillating tiles, which produce a signal that is amplified by photomultiplier tubes and sent for read out. Behind the EM end-cap calorimeters along

the z -axis are the **LAr hadronic end-cap calorimeters**. These calorimeters also use liquid argon, and so are kept in the same cryostats as the EM calorimeters. They function similarly to the EM end-cap calorimeters, but copper is used instead of lead for shower development. The hadronic calorimeters have pseudorapidity coverages of $0 \leq |\eta| < 1.7$ (tile) and $1.5 \leq |\eta| < 3.2$ (hadronic LAr end-cap), respectively [2].

Finally, the calorimeter system is completed by the **forward calorimeters**, which finish the nearly-hermetic energy seal by covering electromagnetic and hadronic energy measurement in the range $3.1 < |\eta| < 4.9$ [2]. Each forward calorimeter has three modules, arranged one behind the other in increasing $|z|$. Each module has a similar design, built to withstand the high levels of particle flux that occur close to the beam-line. A matrix of tubes spans the 45 cm length of the module, running parallel to the beam-line. Each tube contains a heavy material for shower propagation, a liquid-argon gap for energy sampling, and an electrode for read-out. The first module (closest to the interaction point) uses copper for shower propagation and functions as an electromagnetic calorimeter. The remaining two modules function as hadronic calorimeters, using tungsten in place of copper to increase the stopping power of the detector and ensure that hadronic shower energy is contained.

Muon Spectrometer

Muons are significantly more penetrative than many other particles ATLAS must detect. The muon spectrometer, which surrounds all other detectors in ATLAS (see Figure 7), is dedicated solely to the purpose of tracking muons. The system relies on a set of powerful magnets which create toroidal magnetic fields around the outer barrel (at large r , just beyond the tile calorimeter) and end-cap (at large $|z|$, just beyond the forward calorimeter) regions of ATLAS. Monitored drift tubes (MDTs) in the toroidal magnetic field form the heart of the muon precision tracking system. Several layers of MDTs provide coverage over the region $0 < |\eta| < 2.7$, tracking muons as their trajectories curve due to the influence of the

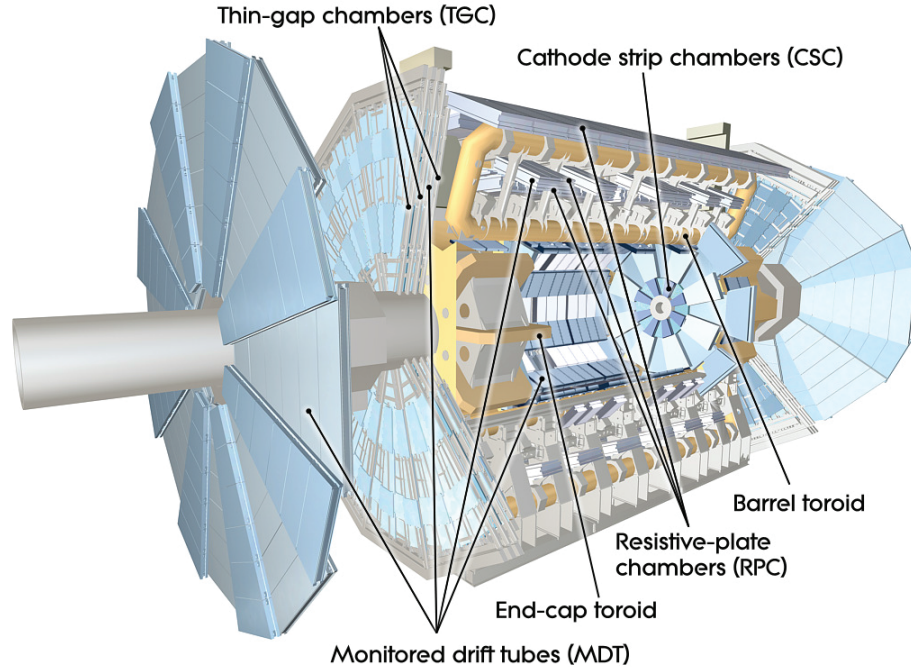


Figure 7: Muon detectors in ATLAS. The calorimeters and ID have been removed from the detector model (compare with Figure 2). Labelled in the diagram are: the toroid magnets, the muon precision tracking detectors (MDT, CSC), and the muon triggering detectors (RPC, TGC). Figure from [2].

field. In the region $2 < |\eta| < 2.7$, a layer of MDTs is replaced with cathode-strip chambers (CSC) (a variant on the classic multi-wire proportional chamber) to better deal with the higher particle flux in forward detector regions [2].

The precision tracking detectors are complimented by dedicated fast-triggering detectors. This muon triggering system consists of resistive plate chambers (RPCs) in the barrel region from $0 < |\eta| < 1.05$, and thin gap chambers (TGCs) in the end-cap region $1.05 < |\eta| < 2.4$ [2].

2.2 The ATLAS Electromagnetic Calorimeter

To reiterate, the measurement of energy in a calorimeter relies on the development of electromagnetic and hadronic showers caused by interactions between the particle and the

significant amount of material it encounters inside the device. A high-energy particle of the appropriate species (not all high-energy particles initiate significant showers) traversing some significant amount of matter is likely to experience an interaction that results in the creation of new (or additional) particles, each with an energy that is necessarily lower than the original. These lower energy particles continue propagating through the material and eventually (provided they have not lost too much energy) produce yet more particles. The shower grows in this way until the energies of the particles fall below a critical level.

Electromagnetic showers are initiated by high-energy electrons and photons, and they propagate via a small set of electromagnetic interactions. Hadronic showers propagate via both strong and electromagnetic forces, making them more difficult to model. The shower formation process is described in more detail for electromagnetic showers in Section 3.1. Hadronic showers (and the calorimeter designed to measure them) are not relevant to this analysis, and so are not covered here.

2.2.1 ATLAS Electromagnetic Calorimetry

This section summarizes how the ATLAS electromagnetic calorimeter makes energy measurements. To give the discussion a bit of context, it is useful to first broadly summarize the layout of the EM calorimeter as a whole. The full geometry of the calorimeter is covered in detail in Section 2.2.2.

The ATLAS electromagnetic calorimeter is divided into one "barrel" and two "end-cap" sections. Each section is segmented in two or three depth layers to allow for the observation of shower development as particles cascade through the calorimeter. Each layer is further divided into cells, which provide granularity in η and ϕ . The dimensions of the cells define the spatial resolution of energy measurements in the calorimeter. A

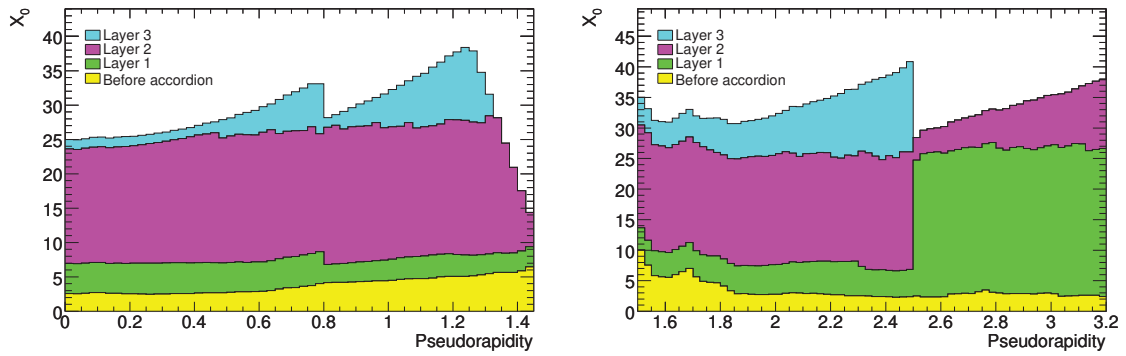


Figure 8: Material in ATLAS up to the last layer of electromagnetic calorimeter. The plot on the **left** concerns material in the barrel EM calorimeter; the plot on the **right** the end-cap EM calorimeters. The amount of material is given in number of radiation lengths X_0 . "Accordion" refers to the shape of EM calorimeter electrodes in layers 1-3, so material "before the accordion" refers to material between the beam-line and first layer of the EM calorimeter. In the precision measurement region ($|\eta| < 2.5$), the calorimeter is divided into three layers, with most of the material located in the second layer. Figure from [2].

presampler also functions as part of the EM calorimeter system, complementing the barrel EM calorimeter with an additional "zeroth" layer over a limited pseudorapidity region.

An important design consideration in a calorimeter is the amount of material in the device. Without sufficient material, particles from the shower might escape the calorimeter without being measured. Since the energy of the original particle is entirely contained within the numerous shower particles, not being able to fully contain the electromagnetic shower means not being able to make an accurate energy measurement. Figure 8 shows the material inside and before the calorimeter (i.e. between the beam-line and the first layer of the calorimeter). The material measurement is given in units of *radiation length* X_0 . The radiation length, loosely defined, is the mean length in a material over which an electron will lose all but $1/e$ of its initial energy. The concept of the radiation length is explored in more detail in Section 3.1.

Propagating and containing a shower is obviously not enough, since the energy of the particles must be measured if the device is to be useful. In addition to providing the

necessary amount of material, the calorimeter should also provide a medium for reliable energy measurement. Measurement in electromagnetic calorimeters can be carried out using familiar particle detection tools like, for example, scintillators and photomultiplier tubes [20]. In ATLAS, energy measurement in the EM calorimeter is carried out using a liquid medium under high voltage [2]. Electrons and photons traversing through an appropriate liquid or gas will tend to ionize it [15]. If the region is under an electric potential difference, the ionized charges drift and create a measureable current.

Using a substance that satisfies both the material and energy-measurement requirements can be prohibitively expensive or difficult to work with. A common alternative is to use two different substances in a heterogenous *sampling* calorimeter design [36]. One of the substances, the *absorber*, provides the bulk of the interaction material. The other, the *sampling* material, is used for energy measurement. The ATLAS electromagnetic calorimeter is a sampling calorimeter which uses lead plates as the absorber material and liquid argon (a radiation-hard noble gas) as the active sampling material.

In a sampling calorimeter, only a fraction of the energy is deposited into the active layer. For the device to be useful, the sampled energy must be proportional to the total energy. The relationship between sampled and total energy can be estimated from simple shower models or Monte Carlo simulations, but a more reliable technique is to perform a test-beam experiment, where particles of a known energy are fired into the calorimeter and the response is measured. Since shower development is based on probabilistic processes, there can be significant fluctuations in the shower shape, which will lead to fluctuations in sampled energy. This has the effect of limiting the energy resolution of the detector (see the discussion on calibration in Section 3.3).

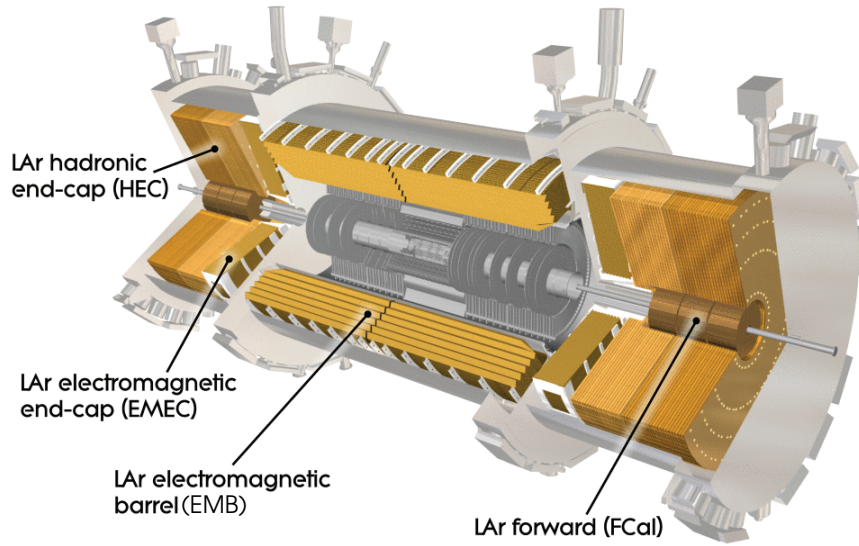


Figure 9: Cut-away view of the liquid argon calorimeters in ATLAS. The two half-barrels and two end-cap electromagnetic calorimeter sections are shown here, closest to the inner detector. The accordion plate geometry is visible in the barrel calorimeter. Also shown are the hadronic end-cap and forward calorimeters, along with the three cryostat vessels that house all of the liquid argon calorimeters. Figure from [38].

2.2.2 EM Calorimeter Geometry

Figure 9 shows a three-dimensional schematic of the ATLAS liquid argon calorimeters. The electromagnetic barrel calorimeter wraps around the central beam-line with full 2π coverage in the azimuthal direction ϕ . The two half-barrel devices extend out to $\eta = 1.475$ (or $\eta = -1.475$) and meet at $\eta = 0$. The electromagnetic end-cap calorimeters (or EMEC) are wheel-shaped devices that flank the barrel calorimeter on both sides and extend coverage of the EM calorimeter system out to $|\eta| = 3.2$. Each EMEC contains an "inner" and "outer" wheel section. The inner and outer wheels meet along $|\eta| = 2.5$, which is the upper limit of the ATLAS precision-measurement region as defined by the coverage of the inner tracking detectors.

The region where the barrel and end-cap calorimeters overlap in pseudorapidity (commonly referred to as the transition or "crack" region) is notoriously difficult to model in simulation, as it is full of inner detector read-out services and other kinds of passive material. Precision analyses often avoid using particles detected in this region. The barrel and end-cap calorimeters formally overlap in $1.375 < |\eta| < 1.475$, but in practice, a larger pseudorapidity range of $1.37 < |\eta| < 1.52$ around the overlap region is excluded from the analysis. (The region excluded from an analysis may be larger to satisfy strict precision requirements. As an example, in a 2014 $H \rightarrow \gamma\gamma$ Higgs mass measurement [39], no photons are used from the region $1.37 < |\eta| < 1.56$.)

Lead plates are stacked in ϕ around the calorimeter with regular spacing between plates. The gap between the plates is bisected with with an electrode plate for readout, and the remaining space is filled with liquid argon. In order to keep the argon in liquid state, the calorimeter is housed in a cryostat, which maintains a cold temperature just under 89 K [40].

With flat absorber and electrode readout plates, particles could traverse the calorimeter without ever encountering the absorber material. The gap regions between plates would create periodic holes in the ϕ coverage of the calorimeter. To remedy this, the plates are folded in ϕ into an accordion shape. (The folding angle varies with radius to maintain a constant gap between plates.) This provides complete coverage in ϕ and ensures that particles moving through the calorimeter traverse alternating layers of absorbing and sampling material.

In both the barrel and end-caps, the read-out electrode plates are segmented into layers. The layers are visible in the electrode plate schematics shown in Figure 10. The plates are divided into three layers through most of the barrel and outer wheel sections, and into two layers in the inner wheel. The electrodes are segmented further in η and ϕ to individual

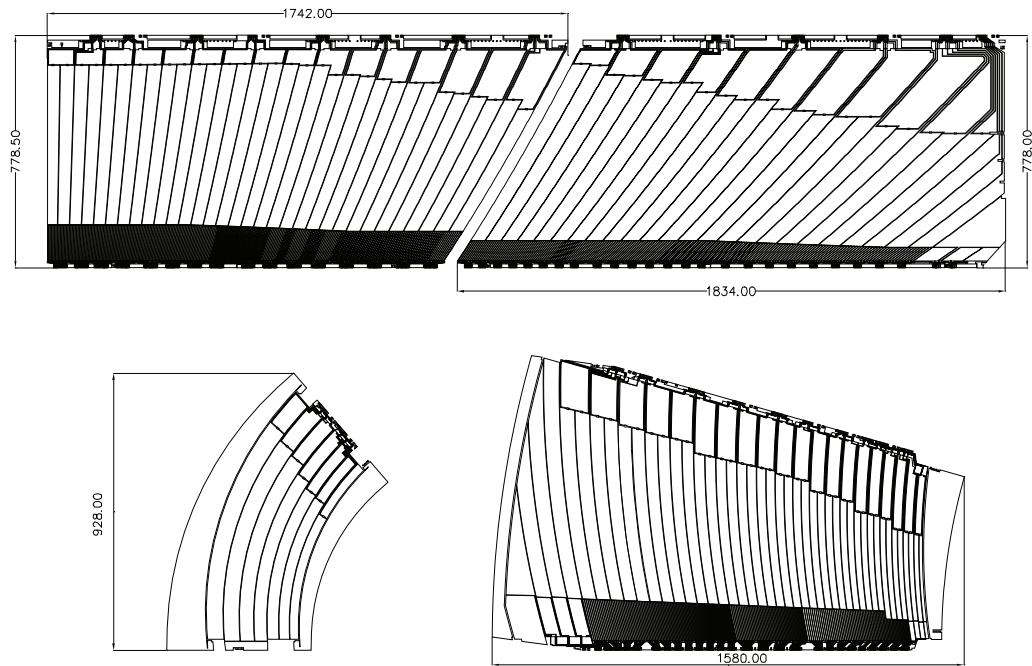


Figure 10: Schematic of the EM calorimeter read-out plates before accordion folding, showing the division into two or three layers. Dimensions are given in millimetres. **Top:** EM barrel calorimeter. **Bottom left:** EMEC inner wheel. **Bottom right:** EMEC outer wheel. Installed in the detector, the orientation of the plates is such that the layer with the finest segmentation is always closest to the center of ATLAS. The plates are folded such that the final depth of the calorimeter is less than the vertical dimension given here (i.e. the accordion oscillations run from top to bottom of the schematics, with folds rising in and out of the page). Figure from [2].

cells with layer-dependent dimensions. Energy measurements from each cell are read out through the electrode to detector-mounted front-end boards where the signals are processed and sent off for further processing by back-end electronics [2].

The schematic in Figure 11 shows a representative section of the barrel calorimeter. The shallow first layer is segmented into strips that are skinny in η , allowing for precision measurements of shower pseudorapidity. The second layer is the largest and contains most of the absorber material. Ideally, most of the shower energy is deposited in this layer. The third layer has the largest cell size, and is useful mostly to capture late shower development and measure any leakage out of the back the calorimeter. Tables 3 and 4 summarize important geometric properties of the barrel and end-cap electromagnetic calorimeters.

Table 3: Summary of EM barrel calorimeter geometry. Length and number of absorbers are given for half-barrels. The full barrel calorimeter is comprised of two half-barrels that meet at $\eta = 0$. Properties summarized from [2].

Barrel calorimeter properties		
Pseudorapidity coverage	$0 < \eta < 1.475$	
Length (m)	3.2	
Inner radius (m)	1.4	
Outer radius (m)	2	
Number of absorbers	1024	
Thickness of absorbers (mm)	$0 < \eta < 0.80$	1.53
	$0.80 < \eta < 1.475$	1.13
Cell dimensions		
All cell dimensions given as $\Delta\eta \times \Delta\phi$. $\Delta\eta$ and $\Delta\phi$ measurements given in units of size 0.025		
Layer 1	$0 < \eta < 1.40$	$1/8 \times 4$
	$1.40 < \eta < 1.475$	1×1
Layer 2	$0 < \eta < 1.40$	1×1
	$1.40 < \eta < 1.475$	3×1
Layer 3	$0 < \eta < 1.35$	2×1

Table 4: Summary of EM end-cap calorimeter geometry. Properties summarized from [2].

EMEC outer wheel properties		
Pseudorapidity coverage	$1.375 < \eta < 2.50$	
Length (m)	0.63	
Outer radius (m)	2.098	
Number of absorbers	768	
Thickness of absorbers (mm)	1.70	
EMEC inner wheel properties		
Pseudorapidity coverage	$2.50 < \eta < 3.20$	
Length (m)	0.63	
Inner radius (m)	0.330	
Number of absorbers	256	
Thickness of absorbers (mm)	2.20	
Cell dimensions		
All cell dimensions given as $\Delta\eta \times \Delta\phi$.		
$\Delta\eta$ and $\Delta\phi$ measurements given in units of size 0.025		
Layer 1	$1.375 < \eta < 1.425$	2×4
	$1.425 < \eta < 1.50$	1×4
	$1.50 < \eta < 1.80$	$1/8 \times 4$
	$1.80 < \eta < 2.00$	$1/6 \times 4$
	$2.00 < \eta < 2.40$	$1/4 \times 4$
	$2.40 < \eta < 2.50$	1×4
	$2.50 < \eta < 3.20$	4×4
Layer 2	$1.375 < \eta < 1.425$	2×1
	$1.425 < \eta < 2.50$	1×1
	$2.50 < \eta < 3.20$	4×4
Layer 3	$1.50 < \eta < 2.50$	2×1

Table 5: Summary of presampler geometry. Cell dimension $\Delta\eta$ and $\Delta\phi$ measurements are given in units of size 0.025. Properties summarized from [2, 38].

Presampler properties		
Barrel presampler	Pseudorapidity coverage	$0 < \eta < 1.52$
	Depth (mm)	11
	Cell dimensions ($\Delta\eta \times \Delta\phi$)	1×4
End-cap presampler	Pseudorapidity coverage	$1.50 < \eta < 1.80$
	Depth (mm)	9.5
	Cell dimensions ($\Delta\eta \times \Delta\phi$)	1×4

Electrons and Photons in ATLAS

The purpose of this chapter is to describe how electrons and photons are detected by ATLAS. Specifically, the chapter begins with a short discussion of electron/photon interactions with matter and the electromagnetic particle showers that result at high energies. Following this is a description of how signals from these showers in the electromagnetic calorimeter are combined with signals from the inner detector and built (or "reconstructed") into software particle objects which contain all the relevant kinematic and energetic quantities that might be useful in a physics analysis. Finally, the EM calorimeter calibration, which is necessary for accurate measurement of particle energy, is covered in brief, with special emphasis on the elements of calibration that are directly relevant to the material studies described in Chapter 4.

3.1 Electromagnetic Showers

3.1.1 Electromagnetic Interactions with Matter

A particle moving through matter will gradually lose energy as it interacts with the atoms that constitute the material. The interactions depend significantly on the identity and kinematics of the travelling particle as well as the physical properties (density and element composition, for example) of the material being traversed. The following discussion surveys the kinds of interactions an electron (and, almost equivalently, a positron) can undergo in passing through matter. This is followed by a similar discussion for photons. Special attention

is paid to interactions relevant to the energy scales used in the bulk of ATLAS physics analysis.

At low energies (< 10 MeV in lead [15]), electron and positron energy loss in material is dominated by excitation and ionization, where the travelling electron loses energy to the material by either exciting atomic electrons into higher states or ionizing the atom entirely [20]. Various additional interactions contribute to the total electron energy loss at these energies, namely: Møller scattering ($e^-e^- \rightarrow e^-e^-$), Bhabha scattering ($e^-e^+ \rightarrow e^-e^+$), and electron/positron annihilation ($e^-e^+ \rightarrow \gamma\gamma$). (Møller and Bhabha scattering proceed via exchange of a virtual photon between the given initial and final states.)

It is a well known result of electrodynamics that the acceleration of a charged particle produces electromagnetic radiation [9, 41]. An electron (or positron) travelling through matter is slowed by the presence of charged particles in the material, and photons are emitted as a result of the deceleration. At high energies, the likelihood of previously discussed effects (excitation, scattering, annihilation) are diminished, and the energy loss is dominated instead by radiative losses of this sort. This phenomenon (the production of electromagnetic radiation due to the deceleration of an electron moving through matter) is known commonly as *bremsstrahlung*. See Figure 12 for diagrammatic representations of the process.

Having introduced bremsstrahlung, the definition of a radiation length X_0 (covered briefly in Section 2.2.1) can be restated with a bit more precision: X_0 is the mean length in a material over which an electron (in the appropriate energy range) loses all but $1/e$ of its energy due to bremsstrahlung. The radiation length is usually given in either $\text{g} \cdot \text{cm}^{-2}$ or cm ,⁵ and is, for an element with atomic number Z and atomic mass A , roughly proportional

⁵ The first set of units, $\text{g} \cdot \text{cm}^{-2}$, allows for comparison between materials with different densities. The second, cm , takes material density into account and gives the radiation length X_0 as an actual *length*.

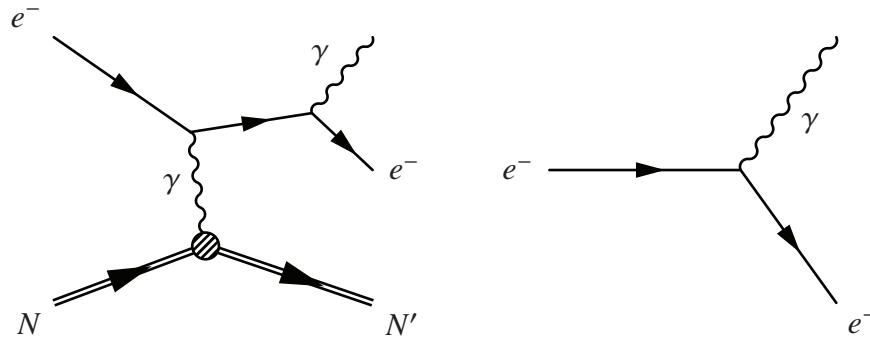


Figure 12: Diagrams showing the bremsstrahlung process for electrons travelling in matter. **Left:** Example of a Feynman diagram showing a first-order bremsstrahlung interaction. The travelling electron exchanges a photon with a nucleus in the material, which decelerates the particle and initiates the emission of a photon. **Right:** A simplified schematic that removes explicit interaction with the material and highlights only the initial and final states of the process. This helps to illustrate the role bremsstrahlung plays in the formation of electromagnetic showers, which is discussed in more detail in Section 3.1.2.

to A/Z^2 [20]. (See references for more exact models [15, 42].) For lead, the radiation length is ~ 0.56 cm [15].

The energy at which the leading source of energy loss for electrons/positrons in a material switches from excitation/ionization to bremsstrahlung is called the critical energy E_c . The 2016 Particle Data Group *Passage of Particles Through Matter* Review [15] gives Rossi's definition of the critical energy as "the energy at which the ionization loss per radiation length is equal to the electron energy." For lead, the primary absorber in the ATLAS electromagnetic calorimeter, the critical energies for electrons and positrons using this definition are, respectively, 7.43 and 7.16 MeV [15]. This is easily visible in Figure 13, which summarizes the various processes undergone by electrons in lead by giving the fractional energy loss per radiation length due to each kind of interaction as a function of the particle's energy.

Likewise, Figure 14 summarizes the interactions for photons in lead. From this it is easily visible that the photon experiences a different set of interactions than the electron as a function of energy. At low energies (< 1 MeV, again in lead), the interactions are

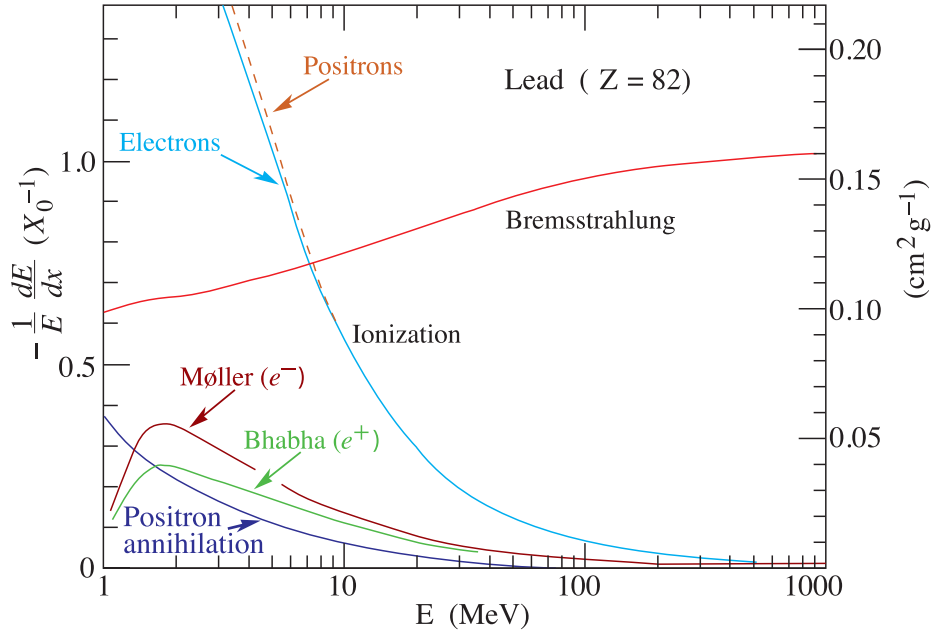


Figure 13: Energy loss due to interaction process as a function of electron or positron energy in lead. Where no explicit difference is noted, the rate is the same for electrons and positrons. Specifically, the left y-axis gives the rate of change in fractional electron energy (i.e. dE/E) over penetration depth (dx) in units of inverse radiation length. The right y-axis gives the same quantity translated into more familiar units. Figure from [15].

dominated by the photoelectric effect (ionization via photon) and Rayleigh scattering. Compton scattering becomes the dominant process for a short energy range around 1 MeV. Further above this energy (above ~ 100 MeV) the dominant process becomes pair production (an interaction that results in the creation of an electron/positron pair: $\gamma \rightarrow e^+e^-$), which remains the leading source of energy loss well up into the highest energies relevant for the majority of photons produced at the LHC ($< \sim 1$ TeV). Figure 15 gives the Feynman diagram for the process.

The bremsstrahlung and pair production processes are closely related [43]. There is a relationship between their cross sections at high energies, namely $\sigma_{pair} = 7/9\sigma_{brem}$. This leads to another useful definition for the radiation length X_0 , equivalent to the last: the radiation length for a material is equal to 7/9ths of the mean free path for high-energy photons before the production of an electron/positron pair. This similarity in scale length

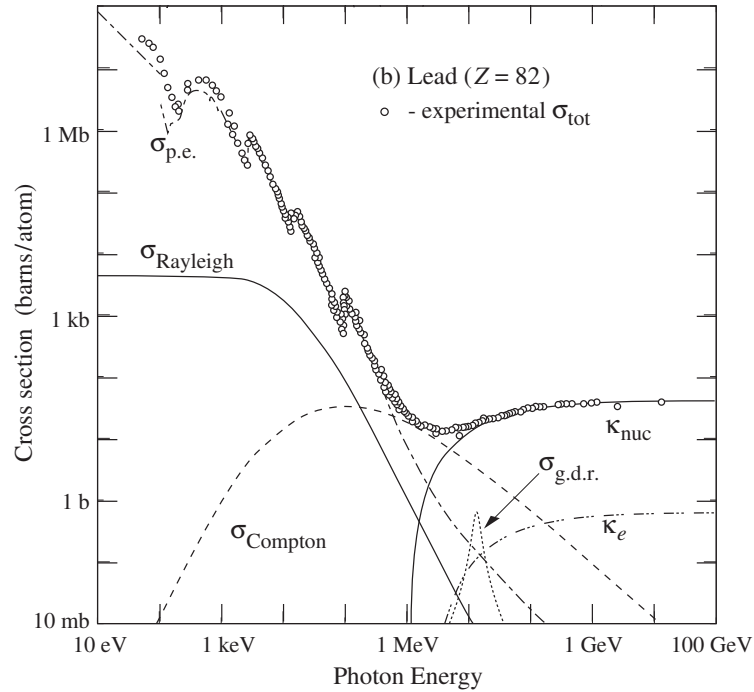


Figure 14: Cross sections for a variety of photon interactions in lead given as a function of the photon energy. The hollow dots give the total cross section. $\sigma_{p.e.}$ gives the cross section for the photoelectric effect and $\sigma_{g.d.r.}$ for photonuclear interactions like the 'Giant Dipole Resonance'. κ_{nuc} and κ_e label the cross section curves for pair production from interactions with the nuclear and electron fields, respectively. Figure from [15].

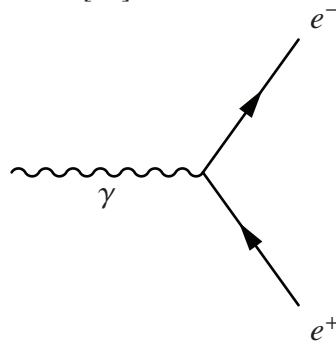


Figure 15: Simplified Feynman diagram for pair production, showing a high-energy photon converting into an electron/positron pair.

for bremsstrahlung and pair production will be useful in the discussion of electromagnetic showers.

At very high energies, the cross sections for both bremsstrahlung and pair production are suppressed by the Landau-Pomeranchuk-Migdal (LPM) effect [15, 20, 44]. For lead,

the energy at which this significantly alters the behaviour of showers ($> 1 \sim \text{PeV}$) is far above what is possible for electrons and photons produced at the LHC [45]. LPM effects in ATLAS are only relevant in showers produced by (relatively infrequent) high-energy particles. Even then, the effects are limited to the very beginnings of the showers, where particles are still at their most energetic. The following section describes a number of standard electromagnetic shower features that are derived without these minor LPM effects in mind.

3.1.2 Characteristics of Electromagnetic Showers

Above the critical energy, electrons (or positrons) interact primarily via bremsstrahlung. The net effect of this process is the electron losing energy via the emission of a photon. Above roughly the same threshold energy, photons primarily undergo pair production and convert to electron/positron pairs. Thus, high-energy electrons produce photons, and high-energy photons produce electrons. As long as the energies of these new particles are high enough, they too will undergo pair production or bremsstrahlung. If the energy of the inciting particle is high enough, a significant chain reaction develops, and the resulting phenomenon is called an electromagnetic shower (or cascade). Figure 16 gives an example of the initiation of a shower via bremsstrahlung. The process, initiated by a single electron or photon, continues down through generations of particles, with electrons and photons producing yet more electrons and photons, until the energies of the new particles are too low to radiate via bremsstrahlung or create electron/positron pairs. The cascade stops, and the remaining energy is expended via lower energy processes like ionization.

Since the emission angle for electrons and photons is small at high energies [20], the shower propagates largely in the direction of the initial particle. Thus the discussion of

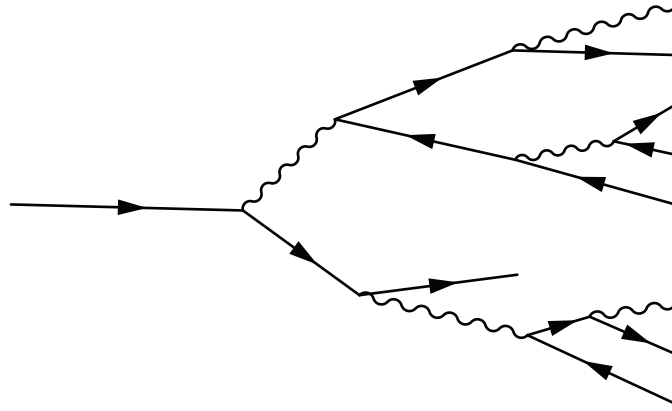


Figure 16: Schematic showing the beginning of an electromagnetic shower as initiated by an electron. Electrons and positrons are indicated by solid lines with arrows (right-facing for electrons and left-facing for positrons). Photons are indicated by wavy lines. Note that each vertex in the shower describes a bremsstrahlung (Figure 12, right) or pair production (Figure 15) interaction. The cascade continues via these two interactions until the particle energies are too low for the processes to dominate.

electromagnetic shower development often refers separately to development in the *longitudinal* (parallel to the initial particle trajectory) and *lateral* (in the plane perpendicular to the initial particle trajectory) directions. Some properties of the longitudinal profile of electromagnetic showers can be explored by considering a standard simplified model of shower development.

Qualitative Model

Consider an idealized shower initiated by a high-energy electron [20, 36, 42]. After one radiation length, the electron undergoes bremsstrahlung and emits a photon with half the energy of the original electron (the rest of the energy going to the electron). The emitted photon travels one radiation length more, then converts into an electron/positron pair, again with each daughter particle taking half the energy of the original photon. The shower continues in this tidy, statistically-averaged way. In this model, each particle travels one radiation length, then "produces" two new particles (either via bremsstrahlung or pair

production), each with half the energy of the original. Thus, the particle number doubles with each radiation length.

If t is the number of radiation lengths travelled by the shower ($t = x/X_0$, with x being the distance travelled in conventional units), the number of particles in the shower as a function of X_0 travelled $N(t)$ is given by:

$$N(t) = 2^t. \quad (5)$$

Let the energy of the initial particle be E_0 . If the energy is divided evenly after each process, the energy of each particle after t radiation lengths $E(t)$ is:

$$E(t) = \frac{E_0}{N(t)} = \frac{E_0}{2^t}. \quad (6)$$

The cascade continues until the energy of the shower particles drop below the critical energy for the material, E_c . Immediately before this occurs, the number of particles in the shower is at a maximum. Soon after it occurs, the shower dies. In this model, the shower ends immediately after the maximum number of particles is reached. The number of radiation lengths t_{max} at which the energy is equal to E_c and the number of particles is at a max is given by a special case of Equation 6 with $E(t_{max}) = E_c$:

$$\begin{aligned} E(t_{max}) = E_c &= \frac{E_0}{2^{t_{max}}}, \\ 2^{t_{max}} &= \frac{E_0}{E_c}, \\ t_{max} &= \log_2 \frac{E_0}{E_c}, \\ t_{max} &= \frac{\ln E_0/E_c}{\ln(2)}. \end{aligned} \quad (7)$$

The maximum number of particles N_{max} , then, is

$$\begin{aligned} N(t_{max}) &= N_{max} = 2^{t_{max}}, \\ N_{max} &= 2^{\log_2 \frac{E_0}{E_c}}, \\ N_{max} &= \frac{E_0}{E_c}, \end{aligned} \tag{8}$$

where an intermediate step from Equation 7 was used for the substitution of t_{max} instead of the final expression, to simplify the algebra. As mentioned in Section 3.1.1, the critical energy for electrons in lead is 7.43 MeV. For an incident particle of 50 GeV, this gives $t_{max} \simeq 12.7$ and $N_{max} \simeq 6729$. With an energy of 500 GeV, the values increase to $t_{max} \simeq 16.0$ and $N_{max} \simeq 67290$.

The model is easily derived and provides a fair description of some of the qualities of electromagnetic showers, giving a rough order-of-magnitude estimation for things like maximum shower depth and number of particles. It fails, however, to accurately model key features of real showers. In the model, the shower abruptly ends after N_{max} is reached, since this corresponds to the point at which the energy $E(t)$ of shower particles falls below the critical energy E_c . Observations of showers from experiment clearly show that the shower continues well beyond the point at which the number of particles is at a maximum. A more accurate shower model is available from Monte Carlo simulation.

Simulation Model

Figure 17 shows the longitudinal energy loss profile for EGS4 simulations [46] of electron-initiated showers in iron. Also shown are the electron and photon number profiles. The energy loss profile in Figure 17 is fit to an equation of the form [15, 36, 42]:

$$\frac{dE}{dt} = E_0 b \frac{(bt)^{a-1} e^{-bt}}{\Gamma(a)}, \tag{9}$$

with t defined as usual ($t = x/X_0$), a and b as fit variables, and $\Gamma(a)$ the standard gamma function: $\Gamma(a) = \int_0^\infty x^{a-1} e^{-x} dx$. b is roughly 0.5 across a wide range of common energies and absorber materials, and a is an energy-dependent term that is determined from a separate calculation. Equation 9 provides a more accurate description of the longitudinal shower development than the simple model developed previously. Defining a new variable $u = bt$ helps to illustrate the role of each term in the equation:

$$\frac{dE}{du} = E_0 \frac{u^{a-1} e^{-u}}{\Gamma(a)}, \quad (10)$$

The gamma function serves to normalize the total shower energy to the energy of the initial particle. At low t , exponential term e^{-u} is close to one, so the energy loss profile is dominated by the power term u^{a-1} . This corresponds to the initial phase of the shower, where the number of particles quickly increases via bremsstrahlung and pair production chain reactions. At sufficiently large t , the exponential term begins to dominate, and dE/dt falls. The depth at which the dominant term switches from u^{a-1} to e^{-u} corresponds to the shower maximum t_{max} . For this longitudinal shower model, t_{max} can be calculated as:

$$t_{max} = \frac{a-1}{b}. \quad (11)$$

Fits to shower energy loss profiles initiated by particles with energies from 1 to 100 GeV in a wide range of materials yield an additional set of closely related expressions for t_{max} [15]. One is appropriate for showers initiated by electrons (t_{max}^e), and the other is appropriate for showers initiated by photons (t_{max}^γ):

$$t_{max}^e = \ln \frac{E_0}{E_c} - 0.5, \quad t_{max}^\gamma = \ln \frac{E_0}{E_c} + 0.5. \quad (12)$$

Equations 11 and 12 can be used together to calculate the fit parameter a (assuming $b \simeq 0.5$

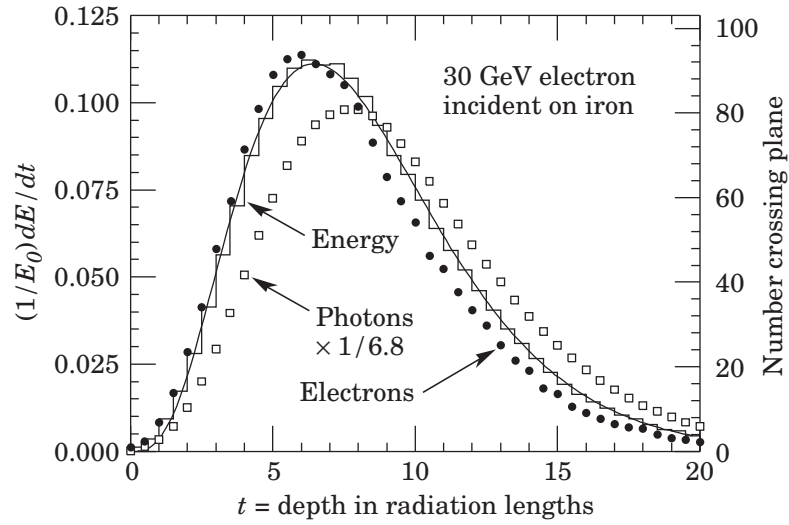


Figure 17: A number of quantities are shown for the EGS4 Monte Carlo simulation of an electromagnetic shower in iron as initiated by a 30 GeV electron. The histogram corresponds to the left y-axis, showing the energy loss (or energy deposition into the iron) per radiation length normalized to the energy of the inciting particle. The solid black line shows a fit (of the form given in Equation 9) to the energy loss histogram. The filled circles and hollow squares give particle number counts for electrons and photons, respectively, and are measured by the y-axis on the right. Particles are counted as they cross through imaginary planes, placed laterally to shower development at intervals of $0.5X_0$. The photon profile has been scaled down by a factor of 6.8 to match the area under its curve to the electron profile. The minimum energy threshold for detection is set at 1.5 MeV. Figure from [15].

or using a tabulated value). Using this model, t_{max} in lead for electron showers with $E_0 = 50$ and 500 GeV are 8.31 and 10.6, respectively. (Note that these values are lower than the values calculated for the same showers using the simplified model (Equation 7): 12.7 and 16.0.)

The lateral development of a shower is more straightforward to characterize. The standard scale length in material with radiation length X_0 and critical energy E_c is the Molière radius, R_M [15]:

$$R_M = X_0 \frac{1}{E_c} m_e \sqrt{4\pi/\alpha}, \quad (13)$$

$$R_M = X_0 \frac{21 \text{ MeV}}{E_c},$$

where $m_e \approx 0.511$ MeV is the rest mass of the electron and $\alpha \approx 1/137$ is the fine-structure

constant. A majority of the shower is contained within a short radius of the longitudinal shower axis. Specifically, 95% of the energy is, on average, deposited within $2R_M$ of the axis [36], whereas 99% is deposited within $3.5R_M$ [15]. For calorimeters that contain multiple elements⁶, the Molière radius is adjusted accordingly. Defining w_i as the weight fraction of the i th element in the calorimeter, R_M can be calculated as:

$$R_M = 21 \text{ MeV} \left(\sum_i \frac{w_i E_{c,i}}{X_{0,i}} \right)^{-1}, \quad (14)$$

where $E_{c,i}$ and $X_{0,i}$ are the critical energy and radiation length, respectively, of the i th element [15].

3.2 Electron and Photon Reconstruction

The ATLAS experiment uses several kinds of detectors in the precision measurement region $|\eta| < 2.47$ to identify particles and measure their kinematic quantities. The set of IBL, pixel, SCT, and TRT trackers in the inner detector region provide track measurements for charged particles. The electromagnetic and hadronic calorimeters record the energies of a wide variety of particles via destructive particle shower measurements. Highly penetrative muons continue past the calorimeters, only depositing a few GeV of energy, and are measured by the outer muon spectrometer. Information from a number of these subdetectors (specifically the inner trackers and electromagnetic calorimeter) is combined to identify electrons and photons.

A summary of the techniques used to identify and reconstruct these particles with varying degrees of confidence is given in Section 3.2.1. Three particle types are discussed:

⁶ The ATLAS electromagnetic calorimeter is an example of such a calorimeter, containing significant radiation lengths of lead and liquid argon. Lead contributes significantly more to the total number of X_0 in the calorimeter, but the effect of the liquid argon is non-negligible.

- **Electrons** (and positrons)
- **Converted photons:** Photons that have converted to an electron/positron pair somewhere in the inner detector. The electromagnetic calorimeter sees showers initiated by the daughter electron and positron, not the photon itself.
- **Unconverted photons:** Photons that have *not* converted to an electron/positron pair somewhere in the inner detector. The electromagnetic calorimeter sees a shower initiated by the photon itself.

Section (3.2.2) introduces the cut-based method of analysis and describes common methods used to select the reconstructed particles with qualities desired for the analysis.

3.2.1 Identifying Electrons and Photons

The reconstruction of both electrons and photons begins with first building inner detector particle tracks and calorimeter energy clusters. A set of algorithms uses these objects as inputs to search for electron and photon candidates, which are then evaluated against a number of additional criteria before being successfully reconstructed into particle objects for analysis. The cluster building algorithms for electrons and photons are very closely related, and so are discussed in general first (along with a discussion of electron track reconstruction) before covering the full reconstruction pipeline for each particle. The following discussion covers the reconstruction process for analysis software release version ‘20.7’.

Calorimeter Energy Clusters

Electrons and photons deposit energy in the calorimeter via interactions (e.g. ionization, compton scattering) undergone by the low energy particles that are produced at the ends of an electromagnetic shower. A single particle entering the calorimeter initiates a shower that

propagates through the detector longitudinally and laterally, depositing energy across several calorimeter cells along the way. A clustering algorithm is required to bundle individual cells with significant energy readings into larger clusters, which ideally contain all the energy necessary to accurately sample a particle shower.

As with all particle decays, the kinematics of any electron or photon produced in the shower are inherently probabilistic. As a result, there are variations in the overall shapes of the signals of interest that must be measured by the calorimeter. For some purposes in ATLAS, the cluster is built cell-by-cell, starting with a local energetic maximum and building the cluster outwards by including neighbouring energetic cells. Such clusters are used for specific signals (for example, where exceptionally low noise backgrounds are required) in the hadronic and forward calorimeters. For electromagnetic showers, an alternate "sliding-window" technique is used [47].

The sliding-window procedure begins with the formation of electromagnetic calorimeter "towers" of size $\Delta\eta \times \Delta\phi = 0.025 \times 0.025$ (defined by the second layer cell size, see Tables 3 and 4). Tower energies give the total energy deposited in a three-dimensional longitudinal slice of the electromagnetic calorimeter (in the radial direction, away from the LHC beam-line). These energies are used to perform a coarse sweep of the calorimeter, searching for potential shower signals by identifying large, high-energy signal regions. The sweep is performed by defining a 3×5 window of towers (window size is given in number of towers in η \times number of towers in ϕ) and sliding the window in units of tower size across the calorimeter. In each position, the total energy of the towers within the window is summed to give a total energy for the region. If a window is found to contain a local energy maximum above a set threshold (2.5 GeV in Run 2, defined to best screen out background from calorimeter noise), the window is identified as a likely candidate for containing a shower signal, and a *seed cluster* is formed.

The full calorimeter energy cluster is built around this seed cluster using information from each layer of the calorimeter. The final size of the cluster depends on which section of the calorimeter the signal is in (barrel or end-cap) and also on the hypothesis for the type of particle (electron, converted photon, or unconverted photon) under consideration.

Inner Detector Tracks

For most purposes in ATLAS, the procedure for reconstructing tracks from inner detector "hits" (i.e. successful position measurements in the IBL, pixel, SCT, or TRT) follows two steps: pattern recognition and track fitting [48, 49]. In the pattern recognition phase, hits are first assembled into groups of three roughly-aligned hits in the SCT or pixel detectors called track "seeds". After the seed has been tested against a number of quality checks, the seed is extended outwards to include hits in more ID layers using a track candidate building algorithm.

A track candidate is considered successful if a number of requirements on track kinematics and detector hits are met. For example, a candidate is rejected if it contains less than seven track hits, or measures a transverse momentum less than 400 MeV [48]. Successful candidates are fit with the ATLAS Global χ^2 Track Fitter to yield a full track [49]. The global track fitter χ^2 test selects the best fit by favouring low differences between measured and fit track positions, scattering angles, and energy loss due to interaction with material [50].

The standard candidate-building procedure includes corrections made to account for energy losses due to particle interactions with the inner detectors. By default, the energy losses are calculated with the assumption that the particle is a pion. For electrons, the energy loss due to bremsstrahlung interactions with inner detector material is much more significant than the equivalent energy loss for pions. Without taking these extra losses into account, the standard track building algorithms does not perform as well for electrons as it

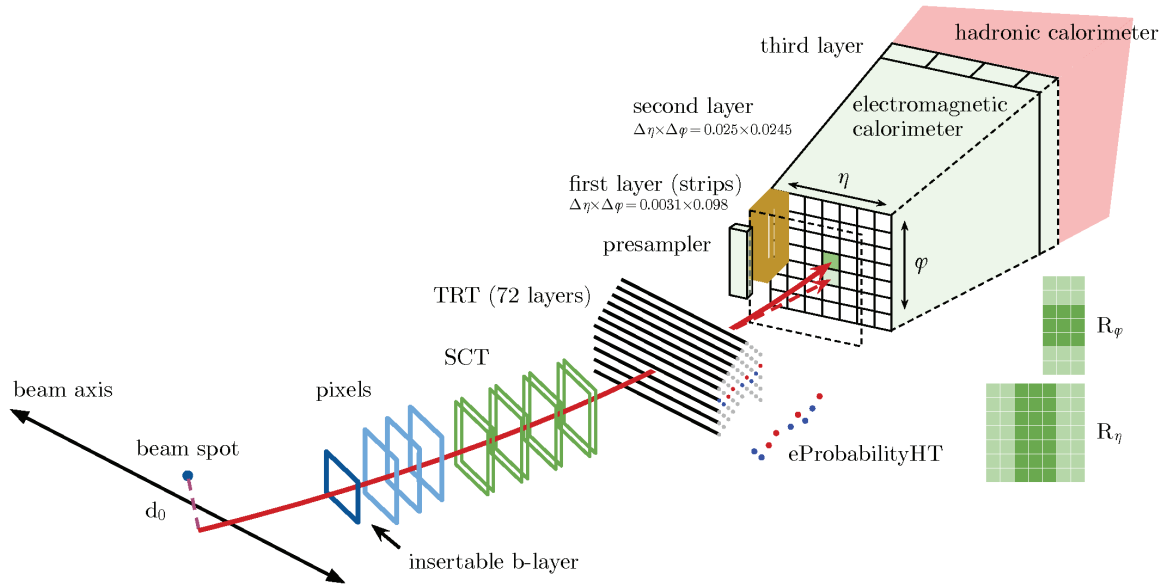


Figure 18: Schematic of the path taken by a common electron moving through the layers of the ATLAS detector. In this example, the electron (red line) is produced near the primary interaction point with a large transverse momentum. The electron first moves through the layers of the IBL, pixel, SCT, and TRT tracking detectors. If the detectors are successful in recording the passage of the electrons, the hits from each layer will be reconstructed together as a track. The particle continues on through the presampler and into the electromagnetic calorimeter. Since there is a non-trivial amount of material in the inner detector, the electron has likely initiated an electromagnetic shower by this point in its trajectory. The energy of the shower energy is absorbed by the calorimeter, and the resulting signal is reconstructed as a calorimeter cluster. Together, the reconstructed track and cluster objects are used to reconstruct the electron. R_ϕ and R_η are two discriminating variables used in electron identification (see Table 12 in the appendix). Figure from [51].

does for other particles. To account for this, the generic track building algorithm includes a set of alternate, electron-specific track building procedures that are triggered when the default fitting procedure fails and the track candidate falls within a calorimeter cluster region of interest. (More precisely, a fit is attempted with the electron hypothesis if the default pion hypothesis fails to successfully extend a track seed with $p_T > 1$ GeV to a track candidate with at least seven hits.)

Reconstruction of Electrons

Figure 18 shows the path of an electron from the interaction point to the electromagnetic calorimeter, emphasizing the various ATLAS subdetectors it encounters along the way. A

successfully reconstructed electron is built from both a reconstructed track, which describes the electron's path through the inner detector, and a reconstructed calorimeter cluster, which provides a good measurement of the electron's energy via the shower it initiates. To successfully reconstruct an electron, then, it is necessary to match the position of a calorimeter cluster to a successfully reconstructed track with suitable kinematics.

The matching of corrected tracks to calorimeter clusters is a complex subject that is not covered here. Essentially, given a suitable cluster seed, track candidates are loosely matched if they pass a set of detector-hit and η, ϕ proximity requirements and used with the cluster to reconstruct an electron. With the reconstruction finished, the resulting set of electrons can be pruned further by excluding electrons that do not meet specific "selection" criteria. This is covered in more detail in Section [3.2.2](#).

Reconstruction of Photons

Converted and unconverted photons (recall the definition given at the start of this chapter) leave very different signatures in ATLAS. The suite of inner detectors only detect charged particles, so unconverted photons are visible only as a result of the electromagnetic showers they induce in the calorimeter. In the language of reconstruction, that means they are identified by the presence of a calorimeter cluster without any matching tracks in the inner detector.

Converted photons undergo pair production before leaving the inner detector region. Provided that they are successfully measured by the inner detector and their trajectories are reconstructed accurately, the electron and positron leave tracks that originate at the same point and curve (due to the influence of the solenoid magnet surrounding the inner detector) in opposite directions. If such a pair of tracks is found, the pair is defined (along with the point where they meet) as a candidate for a conversion vertex. An attempt is made to match the vertex and its tracks to two clusters in the calorimeter, corresponding to the pair

of showers initiated by the electron and positron. If the requirements for a successful match are met, the track and cluster objects are reconstructed as a converted photon and excluded from reconstruction as electrons⁷. (Just as for electrons, the matching process is not trivial. See reference [52] for details.)

To summarize:

- Electrons (and positrons) are reconstructed by matching a calorimeter cluster to a track reconstructed using an electron-specific algorithm that correctly accounts for energy loss due to bremsstrahlung.
- Converted photons are reconstructed by identifying an electron/positron pair, confirming their tracks are consistent with originating from a photon conversion, and matching them with a pair of calorimeter clusters.
- Unconverted photons are reconstructed by identifying a calorimeter cluster with no matching track.

3.2.2 Selection Criteria

Once reconstructed, further requirements are placed on candidates to exclude particles that should not be used in a particular physics analysis. In a cut-based analysis, all of the particles of a given type in a dataset are tested sequentially against a set of strict selection criteria (or "cuts"). If any of the criteria are not met, the candidate is not used. Frequent selection criteria include restrictions on particle $|\eta|$, p_T , and *identification* quality. Particle

⁷ Occasionally, it is not possible to identify the two distinct tracks from a photon conversion. This can happen when the tracks are too close together, or when one of the products of the conversion is too low-energy to be properly reconstructed. For this reason, track candidates that meet certain criteria are used to reconstruct "single-track" conversion vertex candidates. Provided that there is a matching calorimeter cluster, these can be used to reconstruct converted photons.

identification and the frequently used concept of particle *isolation* are explained in more detail in the subsections below.

The pile-up in Run 2 is significantly greater than it was in Run 1. Interesting hard-scatter collisions are rare, so the pile-up collisions most often only contribute low-information noise to the event. In an effort to reduce background (i.e. to exclude the particles that aren't interesting to most physics analyzers in ATLAS) from increased pile-up, a few notable selection criteria have become fairly standard for electrons in Run 2. Requirements are applied that ensure the electron track origin is compatible with the position of the primary vertex corresponding to the hard-scatter interaction. These requirements apply restrictions to the track's transverse and longitudinal impact parameters, d_0 and z_0 , where d_0 is defined as the closest distance in the transverse plane between the particle's track and the measured position of the beam-line, and z_0 gives the distance in the z direction between the beam-spot and the point at which d_0 is measured.

Identification

In ATLAS, a distinction is made between "prompt" and "non-prompt" electrons and photons. In both cases, a prompt particle is a particle created relatively soon (*promptly!*) after the initial proton-proton collision. This is a useful concept because it distinguishes between the particles that are more likely to have been produced in the interesting, original hard-scatter interaction, from the particles that are produced plentifully in the detector from (for example) hadronic jets [52]. Both prompt and non-prompt particles can be classified using an appropriate reconstruction procedure.

Occasionally, the particle reconstruction algorithms will falsely interpret signals from other phenomenon as electrons or photons. Charged hadrons produced near the interaction point, for example, are tracked by the inner detector and can leave significant energy deposits

in the electromagnetic calorimeter. The reconstructed track and cluster objects may pass electron matching criteria, resulting in a "fake" reconstructed electron [49].

It is necessary, then, to distinguish the good, signal particles (prompt, correctly reconstructed particles) from the background particles (non-prompt or incorrectly reconstructed particles) so that the particle objects used in an analysis are overwhelmingly signal-like. Reconstructed particles are tagged with an identification quality that indicates how closely they behave like ideal signal particles. The particles are classified according to a set of identification *operating points*. For electrons, the operating points in order of increasing signal purity are *loose*, *medium*, and *tight*. Each step up in signal purity corresponds to an additional set of requirements on the reconstructed electrons, resulting in a more pure sample at the cost of a loss in efficiency. Thus, for example, all tightly identified electrons also pass the requirements for medium and loose identification. For photons, only two points are defined: *loose* and *tight*.

Particle identification relies heavily on a likelihood-based multivariate analysis of several discriminating variables [51, 52]. To give an idea of what quantities are under consideration when determining identification quality, discriminating variables include: the shower width in each layer of the electromagnetic calorimeter, the energy deposited by the particle in the first layer of the hadronic calorimeter, and the number of track hits in the inner detector. The full lists of discriminating variables for photons and electrons are given in the appendix in Table 11 and Table 12, respectively.

Background and signal probability density functions (PDFs) are generated from data for each discriminating variable. PDFs are generated in η and ϕ bins to account for differences in variable distributions due to the detector geometry. To classify a particle within one of the identification operating points, the probabilities $P_{i,S}(x_i)$ and $P_{i,B}(x_i)$ (the probabilities of measuring a value x_i for the i th discriminating variable in signal and background samples,

respectively) are calculated for each discriminating variable. A discriminant $d_{\mathcal{L}}$ is built from the probabilities [49]:

$$\mathcal{L}_S = \prod_i P_{i,S}(x_i), \quad \mathcal{L}_B = \prod_i P_{i,B}(x_i), \quad (15)$$

$$d_{\mathcal{L}} = \frac{\mathcal{L}_S}{\mathcal{L}_S + \mathcal{L}_B}. \quad (16)$$

A different requirement on the discriminant is defined for each operating point. The discriminant threshold varies slightly as a function of number of primary vertices in the event to account for noise from high pile-up [51].

Isolation

Another useful quantity for discriminating between background and signal particles is particle isolation. Selecting particles that are relatively isolated from others tends to exclude, just as for identification, non-prompt and hadronic backgrounds. The isolation is determined by summing up the total momentum or energy in a cone around the particle track or calorimeter cluster. (The energy of the original track or cluster is either subtracted away via corrective techniques or else never included in the sum in the first place.)

Two kinds of discriminating variables are used to define isolation requirements, one for cluster isolation and the other for track isolation. The precise definitions of the variables vary slightly for electrons and photons, but the general idea remains the same. An example here will be given for electrons. The cluster discriminant $E_T^{cone0.2}$ gives the sum of the transverse energies for all clusters within a $\Delta R = 0.2$ cone of the original cluster. Similarly, the track discriminant $p_T^{varcone0.2}$ gives the sum of transverse momenta for all suitable tracks in a cone around the original track. ("Suitable" tracks here pass a set of quality requirements and are compatible with the same primary vertex as the original electron

track.) For track isolation, the (variable) size of the cone ΔR is the minimum of either 0.2 or $10 \text{ GeV}/E_T$ [51].

Isolation operating points are then defined by applying requirements to the quantities $E_T^{cone0.2}/E_T$ and $p_T^{varcone0.2}/E_T$. In one approach to defining isolation criteria, limits on these discriminating variables are set in order to achieve a targeted isolation efficiency ε_{iso} (which, broadly speaking, is a measure of the proportion of isolated particles that successfully satisfy the isolation selection criteria. Efficiencies are discussed in more detail below.) The electron *tight* efficiency operating point, for example, requires 96% cluster isolation efficiency and 99% track isolation efficiency, whereas the energy-dependent *Gradient* operating point requires cluster and track isolation efficiencies of $0.1143\%(E_T) + 92.14\%$ [51].

Efficiencies

Using electrons as an example, the reconstruction efficiency ε_{reco} of a particle can be loosely defined as:

$$\varepsilon_{reco} = \frac{\text{Number of signal electrons successfully reconstructed}}{\text{Number of signal electrons}}. \quad (17)$$

Thus the electron reconstruction efficiency gives the percentage of signal electrons that are successfully reconstructed by ATLAS. For example, $\varepsilon_{reco} = 95\%$ would suggest that 1 in 20 prompt electrons from hard-scatter vertices do not qualify as electron object candidates by the set of reconstruction requirements. It is possible to define similar efficiencies for the post-reconstruction identification, isolation, and trigger selection of a particle. Together, a total efficiency for the particle can be calculated [49, 51]:

$$\varepsilon_{total} = \varepsilon_{reco} \times \varepsilon_{identification} \times \varepsilon_{iso} \times \varepsilon_{trigger}. \quad (18)$$

The efficiencies vary with the chosen operating points and triggers, and are calculated

sequentially in left-to-right order as arranged in Equation 18 using the subset of successful particles from the previous requirement [51]. (In other words, the identification efficiency only considers particles that have met reconstruction criteria, the isolation rate only considers particles that have met identification criteria, and so on.)

Efficiencies are calculated in both data and simulation. The data/simulation ratio of each efficiency is applied as a multiplicative statistical weight (or *scale factor*) to the simulation to correct for any differences between simulation and data.

3.3 Electron and Photon Calibration

The energy of a reconstructed electron or photon is measured by the electromagnetic calorimeter. The calorimeter must be carefully calibrated in order to ensure that it accurately reconstructs the shower-initiating particle [53]. The resolution with which the energy measurement can be made needs to be quantified as well. Since interpreting signals from the detector requires comparison with the Monte Carlo simulation, several calibration corrections are applied (to either data or simulation, depending on the correction) to achieve the best possible agreement between the two. Cell energy calibration is covered in brief detail here, before summarizing the procedure used to calibrate the data and simulation for the best possible agreement between the two.

3.3.1 Energy Reconstruction

Calibration of the electromagnetic calorimeter begins at the cell level, where the ionization current induced by a passing particle is translated into an energy measurement. When a particle of sufficient energy traverses a calorimeter cell, the ionized charges drift under the influence of the high voltage and are collected by readout electrodes in the liquid argon.

The current peaks immediately, then decreases linearly until all of the charge has been collected, creating a triangular ionization pulse. This ionization pulse serves as input for nearby front-end (on-detector) boards, which shape and digitize the signal before sending it off for further processing by back-end (off-detector) electronics. The digitization involves sampling the shaped curve at a 40 MHz rate (this gives a 25 ns interval between samples, corresponding to the LHC proton bunch spacing) with $N_{\text{samples}} = 4$ for a given curve during normal Run 2 operation.

The calorimeter needs to successfully measure particle energies across several orders of magnitude ($\lesssim 1$ GeV to $\gtrsim 1$ TeV). As part of the processing of the ionization signal, the signal is split into three gain channels with relative magnitudes 1 (low) / 9.3 (medium) / 93 (high). Using a relatively high gain in the case where a particle initiates a weak current allows for the signal to be processed with the same dynamic range of a more pronounced signal. A hardware selector identifies the most appropriate signal of the three to send along to further processing.

The energy of a cell is calculated by summing over the current samples and applying a set of conversion and correction factors according to the formula [53]:

$$E_{\text{cell}} = F_{\text{DAC} \rightarrow \mu\text{A}} \times F_{\mu\text{A} \rightarrow \text{MeV}} \times \frac{1}{\frac{M_{\text{phys}}}{M_{\text{cali}}}} \times G \times \sum_{i=1}^{N_{\text{samples}}} a_i (s_i - p). \quad (19)$$

The current samples are denoted s_i . Beginning with the term in the sum involving these measured samples and moving outwards to summarize the purpose of each additional term:

- $(s_i - p)$: Gives the difference between the current sample s_i and the noise or *pedestal*, p . The pedestal is determined by measuring calorimeter activity in the absence of

any physics events, i.e. it represents the background activity of the cell, which is effectively removed by taking the difference with the sample measurement s_i .

- a_i : The set of coefficients a_i are *optimal filtering coefficients* that are determined such that they minimize the spread of the reconstructed energy [53].
- G : Several aspects of the cell energy calibration make use of a "calibration pulse." A known current is injected (via separate calibration boards) early into the normal readout boards and allowed to propagate through the readout chain as a physics signal would. Since the calibration signal is precisely understood, it provides a way of correcting for any distortions introduced during the signal processing (specifically the digitization and subsequent conversion back into analog current measurement) on a representative current pulse. The coefficient G corrects for these effects.
- $\frac{M_{\text{phys}}}{M_{\text{cali}}}$: Corrects for slight differences between the injected shaped calibration and real physics pulses.
- $F_{\text{DAC} \rightarrow \mu\text{A}}$: Provides the conversion from digital set of samples to analog current. Determined from the calibration pulse.
- $F_{\mu\text{A} \rightarrow \text{MeV}}$: Provides the conversion from analog current to particle energy. Determined from electron test-beam measurements made prior to the installation of the calorimeters in ATLAS. (Electrons of known energy are fired into representative sections of the calorimeter and the resulting signal is measured.)

With the cell energy reconstructed, calorimeter cluster objects are built and used for the reconstruction of electron and photon objects as described in Section 3.2.1. The relative energy resolution of the reconstructed objects as a function of energy can be parameterized

as in Equation 20 [53]:

$$\frac{\sigma_E(E)}{E} = \frac{a}{\sqrt{E}} \oplus \frac{b}{E} \oplus \text{const.} \quad (20)$$

The \oplus symbol indicates addition in quadrature. The a coefficient is the *sampling* or *stochastic* term, which accounts for fluctuations in shower shape and the number of particles actually measured by the active calorimeter volume. This term increases in $|\eta|$ as the amount of material before the calorimeter increases. The noise term b also increases with $|\eta|$ and varies with the size of the window used to build the calorimeter cluster. Remaining uncertainties contribute to the final constant term, which gives the high-energy asymptotic limit of the relative energy uncertainty. The design value of the constant term is 0.7% [53].

3.3.2 Summary of EM Calibration

After the reconstruction of a calorimeter cluster, the cluster energy is further calibrated to correct for the fraction of particle energy that falls outside of a cluster and, additionally, to ensure the best possible agreement in energy measurement between data and simulation. An early step in this calibration procedure is the careful intercalibration of the zeroth (presampler), first, and second layers of the calorimeter. The relative energy deposition in each layer is frequently useful in detector studies (including the present material investigation), so it is important that the relative responses of each layer agree in data and simulation. Since it is directly relevant to the technique used to probe passive material, layer intercalibration of the first and second layers is covered in more detail in Section 4.1.1.

The heart of the calibration is a multivariate analysis (MVA) of numerous cluster properties in Monte Carlo [53]. The MVA aims to optimize agreement between the true energy E_{true} of a particle near the interaction point (prior to losing energy in the inner regions of the detector) and the energy as reconstructed by calorimeter measurements E_{meas} . After the MVA corrections, a number of "uniformity corrections" are also made to account for

regions of the calorimeter where there are small nonuniformities in detector response due to e.g. differences in high voltage or the widening of intermodule⁸ gaps in the calorimeter.

Following these corrections, two important final adjustments are made with corrections derived using electron-positron pairs (from real proton-proton collision data) that are consistent with coming from the decay of a Z boson. The parent Z boson can be reconstructed using an e^-e^+ pair that satisfies a restriction on the value of the combined invariant mass. (The electron-positron mass should fall within a reasonable window of the Z -boson invariant mass, ~ 91 GeV.) With a large enough sample, a very clean sample of electrons is obtained that can be used to compare the energy response in data and simulation. Since very similar responses are required in data and simulation, two final corrections are defined to bring the distributions into agreement. The purpose of the two corrections (defined using terms conventionally labeled α and c) are, roughly speaking, to adjust the mean position (α) and width (c) of the distributions for better agreement.

The energy scale factors α applied to electron and photon energies in data are defined via:

$$E^{data} = E^{MC}(1 + \alpha_i), \quad (21)$$

where α_i is the scale factor calculated for the i th η bin.

The resolution correction term c is defined via:

$$\left(\frac{\sigma_E}{E}\right)^{data} = \left(\frac{\sigma_E}{E}\right)^{MC} \oplus c. \quad (22)$$

This correction is applied in simulation to *smear* the energy resolution. After applying the calibration corrections, the mass distributions in data and simulation of a Z reconstructed

⁸ For ease of construction, the EM calorimeter was divided in ϕ into several identical modules. Each half-barrel is divided into 16 modules, and each end-cap is divided into 8 modules.

from two electrons should be nearly identical. Figure 19, from the Run 1 electron and photon calibration paper [53], shows the agreement between data and simulation distributions after corrections have been applied.

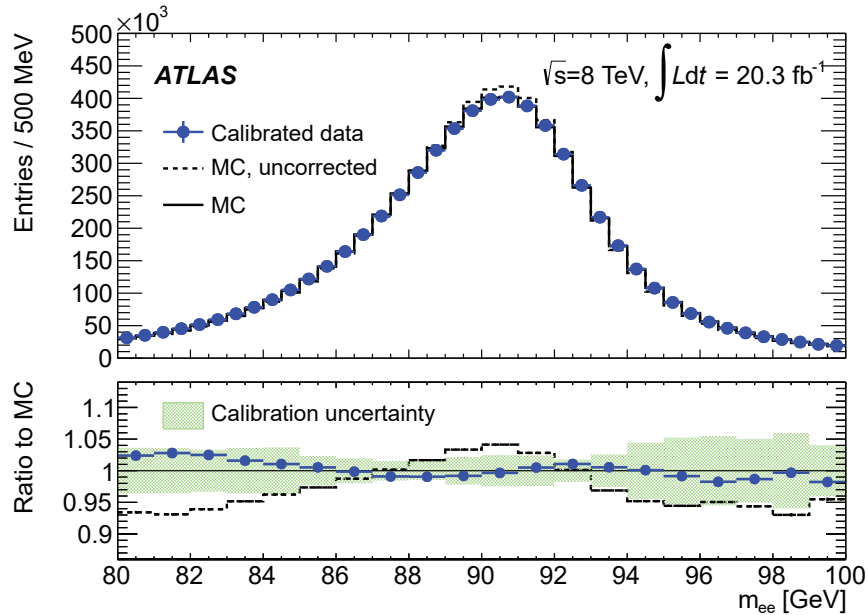


Figure 19: Plot from the Run 1 calibration paper [53] showing the effects of calibration. The **top** plot shows invariant mass distributions of a Z-boson reconstructed from an electron and positron. The blue dots show the distribution in data after calibration corrections have been applied. The dashed and solid black lines show the distributions in simulation before and after applying calibration corrections, respectively. The **bottom** plot gives the ratios of various quantities in the top plot. In the bottom plot, the blue line corresponds to the ratio "Calibrated data"/"MC", and the dashed black line corresponds to the ratio "MC, uncorrected"/"MC". The band in the bottom plot represents the total calibration uncertainty.

Passive Material Estimation

4.1 Passive Material Estimates with E_1/E_2

In order for the ATLAS simulation to be useful, the simulated detector layout needs to model the real detector geometry as closely as possible. The presence of unknown differences between real and simulated detector geometries would bias the simulation results in numerous ways. The MVA calibration described in Section 3.3.2, for instance, relies on a good description of detector material in order to accurately model electron energy losses due to interactions with material between the interaction point and calorimeter [53]. Passive materials like read-out cables, cooling systems, support infrastructure, and power supplies contribute a non-negligible source of material to the total material budget and can be difficult to model in fine detail due to their irregular shapes. See Figure 20, which shows Run 1 simulation material in the inner detector, and Figure 21, which shows the same for the region before the EM calorimeter, for an idea of how passive material contributes to the total material budget in ATLAS. (Since these plots correspond to the ATLAS detector as it was in Run 1, they do not include the modified beam-pipe, IBL, and additional service materials that were introduced in the long shutdown period.)

Careful studies are performed using hadronic and photon conversion vertices to investigate the material of the inner detector and check for possible discrepancies in ID simulation geometry [54], but particles will encounter significant amounts of additional material outside of the inner detector region (e.g. inner detector services and cryostat material) before

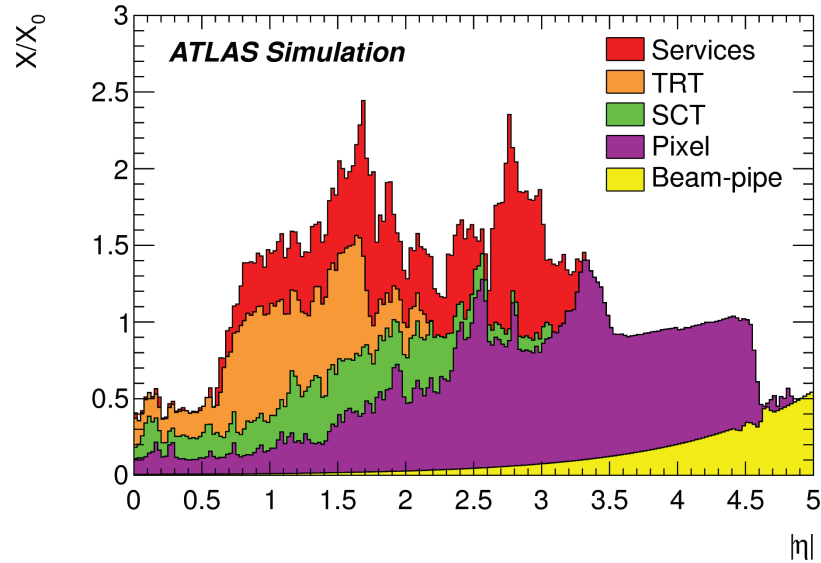


Figure 20: Run 1 simulation material budget in the inner detector, given in number of radiation lengths. Different colours indicate material contributions from different detector components. Significant changes have since been made to the ATLAS inner detector for Run 2. The effects of the new beam-pipe, IBL, and detector services are not shown here. Figure from [53].

entering the calorimeter. This passive material cannot be investigated using the same technique, so it is necessary to use another procedure for probing detector material.

The electromagnetic calorimeter is designed to absorb and measure the energy of electromagnetic showers initiated by the passage of electrons and photons through the detector. The likelihood for a particle to initiate a shower is directly related to the amount of material the particle traverses (recall the definition of the radiation length X_0 from Section 3.1.1). A region of the detector with a particularly high amount of material, for example, would tend to initiate earlier shower development. Conversely, then, observing relatively late shower development would imply that the particle has traversed a region with relatively low amounts of material. Thus the typical longitudinal profile of electromagnetic showers can be used to investigate the relative abundance of material in a region of the detector. Crucially, since longitudinal shower profiles are sensitive to the amount of material in the detector, typical shower behaviour in data and simulation can be used to check for possible material differences between the two.

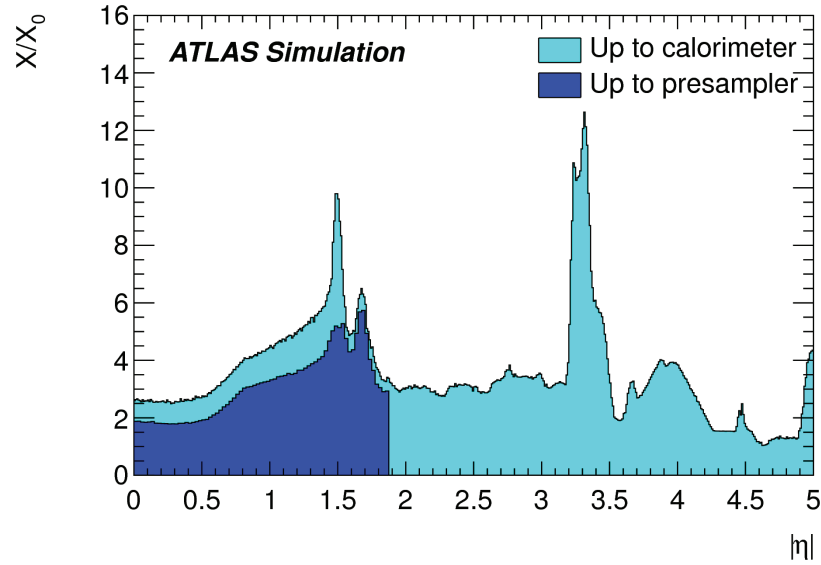


Figure 21: Run 1 simulation material budget up to the presampler and first layer of the EM calorimeter, given in number of radiation lengths. Significant changes have since been made to the ATLAS inner detector (which is included in both regions in shown in this plot) for Run 2. The effects of the new beam-pipe, IBL, and detector services are not shown here. Figure from [53].

The energy deposited in a given layer of the calorimeter can be used to analyze longitudinal shower development. The energy deposited by a particle in the first layer is denoted E_1 , the energy deposited in the second layer denoted E_2 , and so on. For most EM showers, the bulk of the particle energy is deposited into the second calorimeter layer. The third layer usually does not absorb a significant fraction of the energy and serves mostly to give an indication of the amount of energy "leaking" out into the hadronic calorimeter. The amount of energy deposited into the first layer, however, depends significantly on where the shower is initiated. (See Figure 17 for the longitudinal energy loss profile of a representative electromagnetic shower.) Previous studies have shown that the value of the ratio of energies in the first and second layers of the EM calorimeter (E_1/E_2 , or " $E_{1/2}$ ") is very sensitive to the amount of material encountered by a particle [8, 55]. This variable will be used as the main probe throughout the analysis.

Electrons interact with inner detector material, so the $E_{1/2}$ probe is sensitive to all material up to first layer of the EM calorimeter. Section 4.2.2 describes how distorted

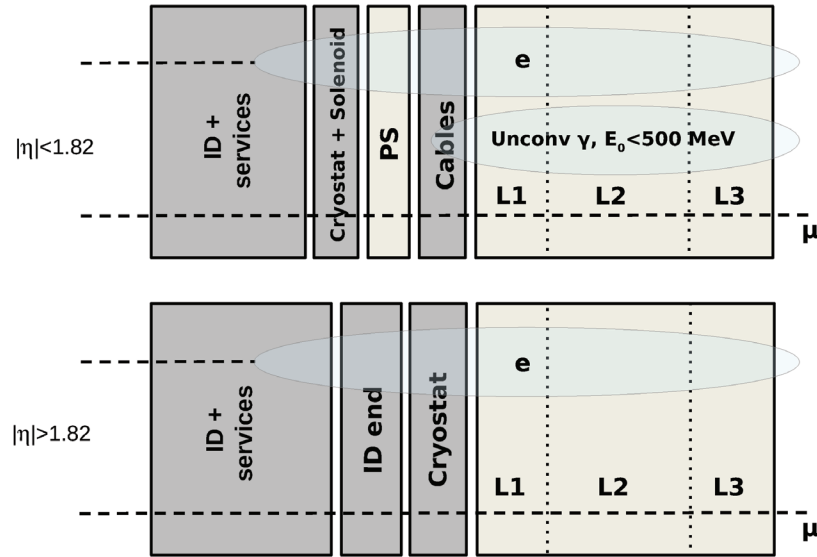


Figure 22: Sketch of the longitudinal profiles of electromagnetic showers initiated by electrons and unconverted photons with low presampler activity. The unconverted photons are only sensitive to material between the presampler and calorimeter accordion for $|\eta| \leq 1.8$. For $|\eta| > 1.8$ there is no presampler, electrons are used to probe all material before the calorimeter. The bottom dashed line in each region shows the passage of muons, which are highly penetrating leave only limited signals in the calorimeter. Figure from [53].

geometries are used to quantify this sensitivity and make an estimate of the material differences in this region.

Selecting unconverted photons by applying a restriction on presampler activity selects particles that have not initiated a shower until after the presampler. Since they have definitely initiated a shower *somewhere* (or else they could not be measured by the calorimeter) they must have initiated a shower via interaction with material after the presampler. This renders them sensitive to material in the narrow region after the presampler (which extends out to $|\eta| = 1.8$) but before the first layer of the EM calorimeter. Section 4.2.1 covers the technique used to make an estimate of material discrepancies in this region. Figure 22 shows a sketch of the showers formed by either type of particle and the regions of the detector that are probed. The results from electrons and photons are combined to divide the detector into two radial regions ("before" and "after" the presampler) and estimate data/simulation material difference in both as a function of $|\eta|$.

4.1.1 Layer 1 and 2 Intercalibration

The purpose of this work is to investigate the description of detector material in the ATLAS simulation and check for possible differences with the real detector. Since the primary probe $E_{1/2}$ is the ratio of energy deposited in the first and second layers of the calorimeter, it is crucial that the relative energy response of the layers in data is the same as in simulation. Layer intercalibration is a standard correction applied early in the calibration procedure (see Section 3.3.2) and relies on the layer energy depositions of muons from $Z \rightarrow \mu\mu$ decays.

Muons are highly penetrative and tend not to interact significantly with material. By extrapolating from muon tracks in the outer muon systems backwards into the first and second calorimeter layers, the energy deposited in each layer by the passing muon (usually localized to a small number of cells, with energies reconstructed with a signal:noise ratio of ~ 3) can be measured. Since muons are mostly insensitive to detector material and do not initiate showers in the same way that electrons and photons do, comparing the energy deposited in each layer provides a clean measurement of the relative energy response.

The $E_{1/2}$ distribution of muons is determined in data and simulation for 24 bins in $|\eta|$. In each bin, a representative quantity (e.g. the mean value) $\langle E_{1/2} \rangle$ is taken and used to calculate the ratio $\alpha_{1/2} = \langle E_{1/2}^{data} \rangle / \langle E_{1/2}^{MC} \rangle$. Two techniques ("truncated mean" and "most probable value" (MPV)) are used to determine the representative value. The final correction $\alpha_{1/2}$ is the average of the two, with the difference between them taken as an uncertainty (see Figure 23). (Additional uncertainties cover the difference in calorimeter response to muons and electrons/photons.) This correction factor is applied to electrons and photons in data to adjust the energy deposited in the second layer and correct for any differences in data/simulation layer intercalibration. In the following sections, quantities shown with and without these layer intercalibration corrections applied are labelled "corrected" and

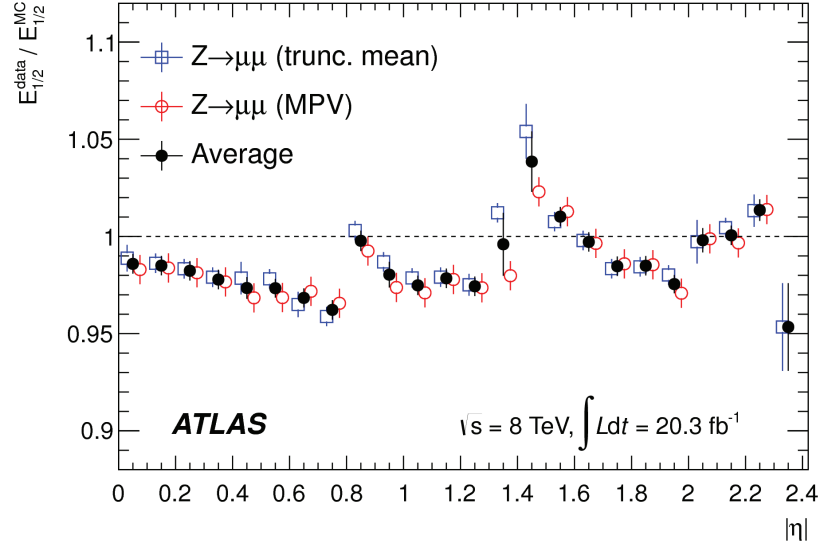


Figure 23: Electromagnetic calorimeter layer 1 and 2 muon intercalibration results from Run 1. The correction factor $\alpha_{1/2}$ is applied to layer 2 energies in data. The final $\alpha_{1/2}$ value is the average of two results calculated using "truncated mean" and "MPV" techniques for extracting a single representative $E_{1/2}$ value from the distribution in a given $|\eta|$ bin. Figure from [53].

"uncorrected", respectively.

4.2 Technique Using Distorted Geometries

This study makes use of a technique established in Run 1 to investigate the material before the EM calorimeter. The technique is detailed extensively in an internal support note [8], which includes full results from the investigation and describes how the simulation geometry was improved as a result. The most important results from this first study are summarized and presented in context (with similar detector performance studies) in a 2013 paper [53] summarizing the whole of the Run 1 calibration effort. The technique, which makes use of the previously discussed $E_{1/2}$ variable and a set of distorted simulation geometries, is outlined below for electrons and photons. In both cases, the general procedure is the same:

- 1. Find the difference in $E_{1/2}$ between data and simulation: $\Delta E_{1/2}^{data}$.
- 2. Determine sensitivity of $E_{1/2}$ to differences in material.
- 3. Use 1 and 2 to estimate differences in material: $\Delta X/X_0$.

For the estimate of the material up to the first layer of the electromagnetic calorimeter (using electrons), this procedure is sufficient. The photon studies require a few additional steps to complete the estimation (mostly due to limited Monte Carlo simulation sample availability). Two methods for calculating photon $E_{1/2}$ sensitivity are presented here, followed by a short summary of their performance after preliminary testing. For the final analysis, the method using inclusive photon samples with distorted geometries was used in favour of the "photon-gun" reweighting method.

4.2.1 Description of the Procedure Using Electrons

The bulk of this investigation is performed assuming reasonable material symmetry in ϕ and across $\eta = 0$. In other words, the detector geometry is frequently investigated solely as a function of $|\eta|$, i.e. averaging over the full 2π in ϕ and any potential material differences between the A- and C- sides of the detector. These are limitations required by some aspects of the available electron and photon calibrations. A particularly important example is the layer intercalibration discussed previously, which is required for an accurate measurement of $E_{1/2}$ and is only determined in $|\eta|$ (rather than η).

Figure 24 shows the distribution of $E_{1/2}$ for electrons from $Z \rightarrow ee$ samples averaged over all η and ϕ . This provides a representative example of the typical $E_{1/2}$ distribution encountered in this study (a prominent peak with a long right-side tail), but this plot is not localized to any particular detector area (i.e. it shows $E_{1/2}$ integrated over all η and ϕ in the

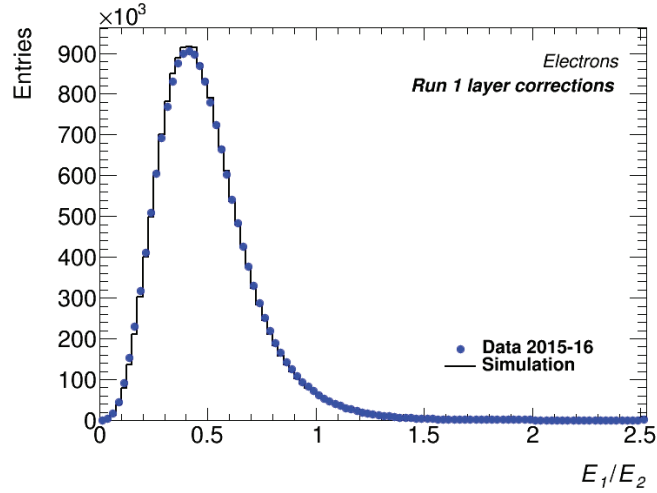


Figure 24: E_1/E_2 for electrons from simulation (black line) and 2015-2016 data (blue circles) $Z \rightarrow ee$ samples. No threshold cut on the tail has been applied. Layer corrections (applied to E_2) from Run 1 are applied to data here.

precision-measurement region), and so is not useful in itself as a way of probing for small regions of material difference. Instead, the region $0.0 \leq |\eta| < 2.5$ is divided into bins of size $|\eta| = 0.05$. Within each bin, the tail of the $E_{1/2}$ distribution is truncated at $E_{1/2} = 3.0$ (for electrons in both data and simulation) and the mean is plotted as a function of $|\eta|$. The profile distribution is shown in Figure 25 for both data (before and after applying the layer corrections described in Section 4.1.1) and simulation.

Taking the difference between $E_{1/2}$ in data and simulation, then normalizing by the latter, gives a useful measure of the relative difference in $E_{1/2}$ (Equation 23):

$$\Delta E_{1/2}^{data} = \frac{E_{1/2}^{data} - E_{1/2}^{MC}}{E_{1/2}^{MC}}. \quad (23)$$

Performing this computation bin-by-bin gives the distribution of the relative difference in $E_{1/2}$ as a function of $|\eta|$: $\Delta E_{1/2}^{data}(|\eta|)$. In order to turn this difference in $E_{1/2}$ into a measure of difference in material, it is necessary to determine how sensitive $E_{1/2}$ is to a change in material $\delta X/X_0$.

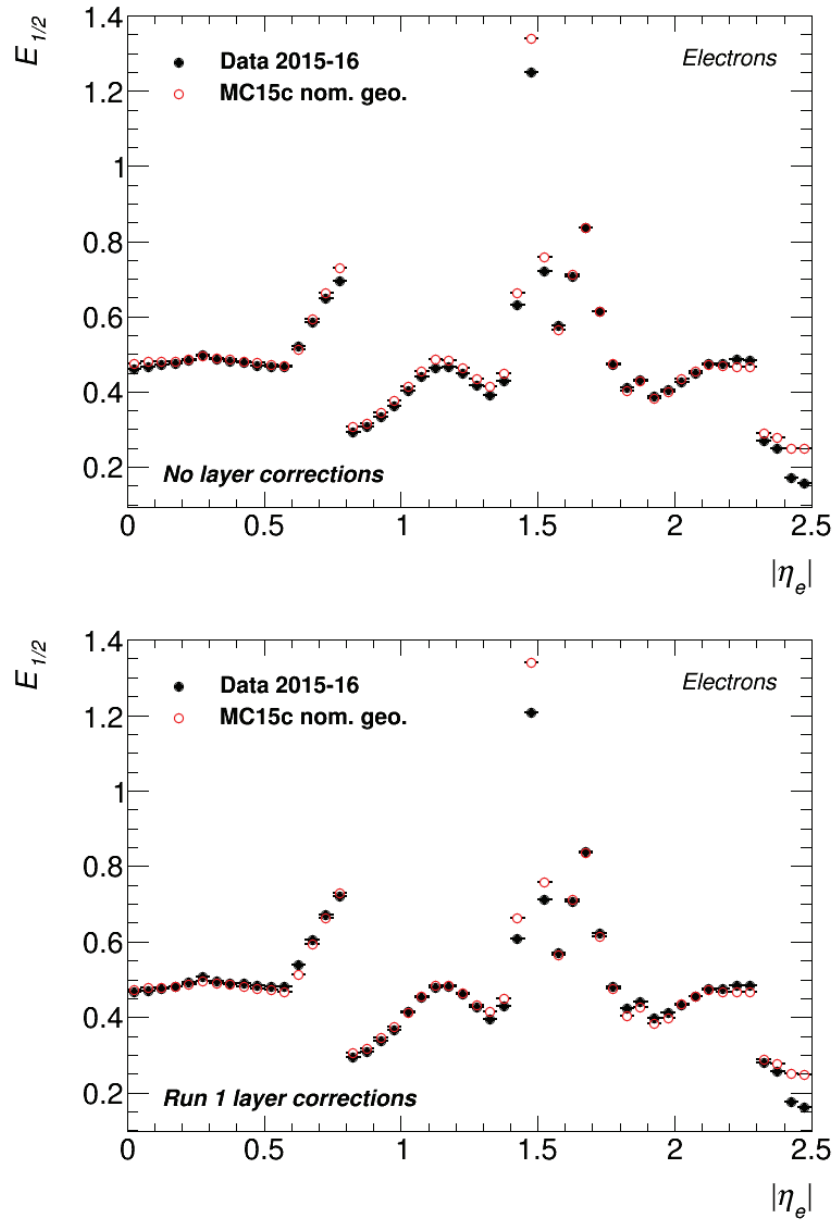


Figure 25: Comparison of E_1/E_2 ($E_{1/2}$) for electrons as a function of pseudorapidity in data and nominal geometry simulation. The top and bottom plots show, respectively, before and after Run 1 layer intercalibration corrections are applied to data. The effects of the layer corrections can be seen, for example, in the region $0.9 < |\eta| < 1.3$, which shows an improved agreement between data and simulation after applying the corrections. This is a profile distribution, i.e. each point gives the mean value of the $E_{1/2}$ distribution for a given bin in $|\eta|$. The full 2015 and 2016 datasets (3.2 fb^{-1} from 2015, 33.0 fb^{-1} from 2016) were combined for data measurements. Nominal geometry in MC15c is identified internally with geometry tag ATLAS-R2-2015-03-01-00.

To determine this sensitivity, alternate simulation geometries are created with known amounts of extra detector material added to the standard geometry (usually placed in regions where material is difficult to measure, i.e. in areas with significant amounts of passive material like read-out cables or support structures). By comparing $E_{1/2}$ distributions in these *distorted* geometries with the distribution in the standard, or *nominal* geometry, it is possible to quantify how $E_{1/2}$ changes as extra material is added to specific areas of the detector.

Sensitivity curves (sensitivity plotted as a function of $|\eta|$) are found by first building $E_{1/2}$ $|\eta|$ profiles with distorted geometry simulations and taking the relative difference with profiles from the nominal simulation.

$$\delta_{rel}E_{1/2} = \frac{E_{1/2}^{distorted} - E_{1/2}^{nominal}}{E_{1/2}^{nominal}}. \quad (24)$$

This relative difference $\delta_{rel}E_{1/2}$ is divided (again, bin-by-bin) into the change in passive material in number of radiation lengths $\delta X/X_0$ in the distorted sample, giving the sensitivity:

$$Sensitivity = \frac{\delta X/X_0}{\delta_{rel}E_{1/2}}. \quad (25)$$

Multiplying these quantities (Equation 23 and Equation 25) gives an estimate of the material difference ΔX between data and nominal geometry simulation in number of radiation lengths (as a function of $|\eta|$):

$$\Delta X/X_0 = \Delta E_{1/2}^{data} \left(\frac{\delta X/X_0}{\delta_{rel}E_{1/2}} \right). \quad (26)$$

While the formal material estimates and calculation of material uncertainties are limited in this study to functions of $|\eta|$, sensitivity results can be loosely extended out into ϕ and η to

(in the case of ϕ) provide a preliminary quantitative check of the material across geometry not yet explored by this method or (in the case of η) check for egregious differences between regions where η symmetry is assumed. Results from this investigation are presented in Section 4.5.4.

4.2.2 Description of the Procedure Using Photons

The procedure for using photons to study the region after the presampler is largely the same as the procedure used for electrons. The mean $E_{1/2}$ value for photons is calculated (per $|\eta|$ bin)⁹ in data and simulation to find the relative difference between the two, which is combined with sensitivity estimates calculated from distorted geometry samples in order to calculate the passive material difference. The η region under investigation is shortened to $0 \leq |\eta| < 1.8$ to limit the investigation to the region covered by the presampler, and the bin size is increased to compensate for a decrease in statistics. Further differences in the analyses are described below.

Combining Radiative and Inclusive Samples

Radiative Z processes ($Z \rightarrow \mu\mu\gamma$, specifically, used here) can provide clean photon samples with an appropriate selection. However, the energy of photons from this process is limited by the mass of the parent Z -boson, so selected particles cover only a small region in p_T . In order to extend the p_T region out to higher values, photons are also taken from a high-energy inclusive photon sample. Results from both samples are combined to give an estimate of photon behaviour over a wide p_T range. (Figure 33 will show the p_T distribution of both photon samples.) The radiative and inclusive results are combined by taking the weighted

⁹ Just as with electrons, the photon $E_{1/2}$ distributions in a given $|\eta|$ bin are truncated before taking the mean. The distributions were truncated at different values for each of the three particle probe types used in the analysis. For electrons: $E_{1/2} < 3.0$. For radiative photons: $E_{1/2} < 2.0$. For inclusive photons: $E_{1/2} < 1.6$ ($|\eta| < 0.8$) and $E_{1/2} < 3.0$ ($|\eta| \geq 0.8$) In each case, the same truncation value was used in data and simulation.

average, with the weight of a point defined as the inverse square of its error. Since the errors are purely statistical, the final measurement is biased heavily towards the sample with a higher number of photons, here the inclusive sample.

Running ATLAS Monte Carlo simulations with enough event statistics to be useful in an analysis is resource intensive. Priority for sample generation goes to simulations that are most useful to the collaboration as a whole. For electrons, the appropriate distorted geometry samples were available in simulation configurations that were otherwise identical to the nominal geometry simulations. Similar distorted geometry photon samples were available, but additional steps were required to determine photon $E_{1/2}$ sensitivities that were applicable to the nominal geometry simulations. The two methods presented here, the first making use of a large inclusive photon sample with significant geometry distortions and the second making use of unusual "photon-gun" samples, describe attempts to calculate a sensitivity curve for photons. The first technique was used in the final analysis. The second is presented here as an outline of a potentially useful method for further studies.

Determining Photon Sensitivity: 1) Distorted Inclusive Sample

Inclusive photon samples (large samples of photons produced inclusively, from which unconverted photons with $p_T > 145$ GeV are selected) were available with several geometry distortions applied to the simulated detector. As discussed previously, the photons used in this analysis are sensitive to material only in a small region of the detector. It is therefore possible to use a geometry configuration with any number of distortions, just as long as any distortion in the region probed by unconverted photons is accounted for. (The particulars of each geometry configuration used in this study are given in Section 4.3. For now, in an effort to provide a general outline of the procedure, the discussion is limited to general details.)

The distorted geometry sample is used with the otherwise identical nominal geometry sample to calculate a photon $E_{1/2}$ sensitivity curve. Applying the sensitivity curve to the combined radiative and inclusive $E_{1/2}$ profile yields the material estimate presented in the results of this analysis.

Determining Photon Sensitivity: 2) Photon-Gun Reweighting

Simulated single photon (or "photon-gun") samples allow for careful study of photons without messy background effects from the many other particles usually involved in proton-proton collisions. Individual photons are generated in the simulation near the detector interaction point with a range of trajectories and initial energies. They propagate outwards through the full ATLAS geometry as normal, leaving clean signals that can be used for careful detector or photon performance work. Just as with full simulation samples, photon-gun samples can be produced with distorted geometries. A measurement of photon $E_{1/2}$ sensitivity to differences in material can be calculated using these nominal and distorted geometry samples. This technique aims to apply these photon-gun derived sensitivities to photons in data and full simulation.

The $E_{1/2}$ quantity varies as a function of p_T . Comparing $E_{1/2}$ profiles from samples with different underlying p_T distributions is not a useful way to investigate differences in geometry, since then the material effects are indistinguishable from the effects due to differences in p_T . The radiative and inclusive photon samples have different p_T distributions, both of which are different from the native p_T distribution of the photon-gun samples. To correct for this, a set of weights can be applied to the photon-gun samples to alter the p_T distribution and match it to the p_T distribution of the inclusive or radiative samples. A sensitivity curve can then be calculated for each reweighting and applied to the respective sample's $E_{1/2}$ profile to yield a material estimate. (In the previous technique, a sensitivity curve generated from inclusive samples is applied to an $E_{1/2}$ profile calculated as the

average of radiative and inclusive profiles. The radiative contribution to the combined p_T distribution is two orders of magnitude less than the inclusive contribution, so using the native inclusive p_T distribution suitably represents the combined distribution.)

Monte Carlo truth p_T is used in the reweighting procedure in favour of reconstructed p_T . (Recall from Section 2.1.1 that "truth" quantities in simulation represent the *actual* quantity as determined by the particle generator. "Reconstructed" quantities are the values *as recorded by the simulated detector*.) By using the true p_T , various geometries can be reweighted using the same set of weights without biasing the distribution towards any particular geometry configuration.

The following example shows the calculation of a sensitivity curve for the radiative photon sample. The weights for $p_{T,\text{truth}}$ reweighting are calculated as the ratio of $p_{T,\text{truth}}$ in photon-gun simulation over $p_{T,\text{truth}}$ in full simulation in 100 $|\eta|$ bins from 0 to 90 GeV. Figure 26 shows both $p_{T,\text{truth}}$ distributions (with area normalized to 1) and the weights obtained by taking their ratio. These weights are applied to photon-gun samples with distorted geometries, correcting their p_T to more closely match the distribution in full simulation.

With the weights applied, the $E_{1/2}$ profile is determined for a number of distorted geometries and the relative difference is taken with a normal geometry simulation (not all results will be shown here- the purpose of this section is to summarize a technique that wasn't used in the final analysis but might prove useful for future work). With these relative differences and information about the distortions in the alternate geometry samples, a photon $E_{1/2}$ sensitivity curve is found, shown in Figure 27.

Using this sensitivity with the measured difference between data and simulation $E_{1/2}$ profiles yields an estimate for the difference in material. The large error bars are a problem when propagating uncertainties through to the material estimate, often giving relative errors

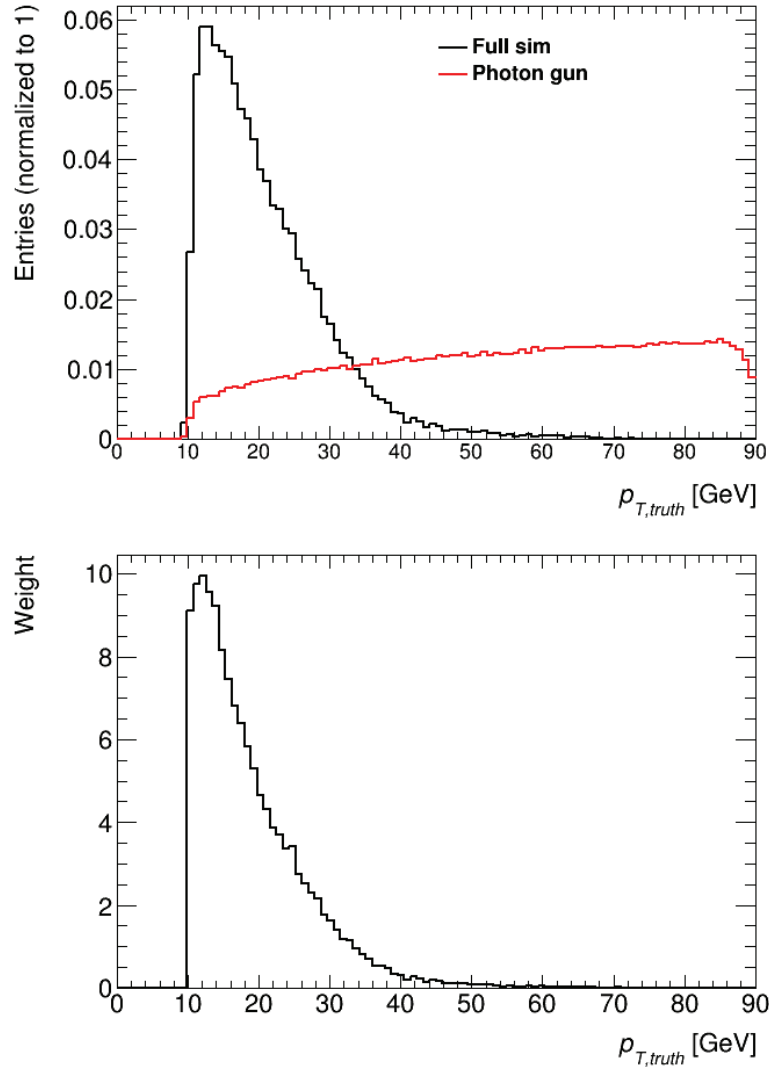


Figure 26: Demonstration of the $p_{T,\text{truth}}$ reweighting procedure. This example uses radiative photons. **Top:** $p_{T,\text{truth}}$ distributions for photons from photon-gun sample (red) and full simulation (black). **Bottom:** Weights to be applied to the photon-gun sample to make it look like the full simulation, calculated by taking the bin-by-bin ratio of the full and photon-gun simulation $p_{T,\text{truth}}$ values.

greater than 30%. This problem might be addressed in future attempts by seeking additional $Z \rightarrow \mu\mu\gamma$ and photon-gun sample production to increase statistics. Additionally, it became clear during the course of the analysis that, due to peculiarities of the ATLAS analysis tools and simulation pipeline, working with photon-gun samples can require a number of modifications to analysis code built for use with full simulation. After consultation with experts, it remained ambiguous whether or not the set of analysis tools was properly equipped

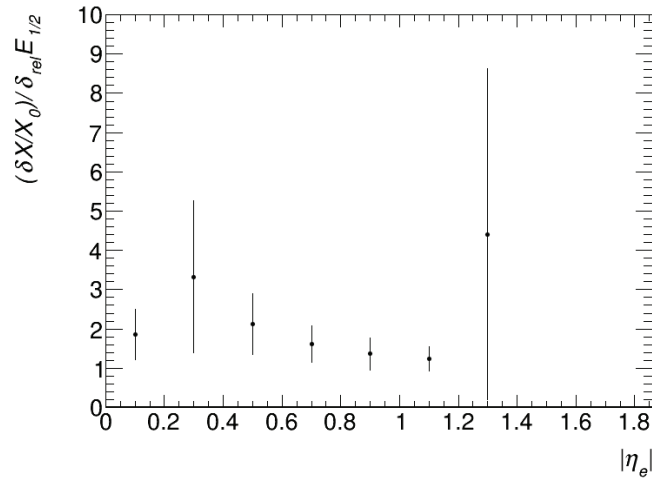


Figure 27: An example $E_{1/2}$ sensitivity curve built using the photon-gun technique. Only points with $|\eta| < 1.4$ are calculated, as the geometry configuration used in this instance does not include distortions outside of this region. The statistical error bars are too large here to be useful in making a material difference estimate, illustrating a key difficulty with this technique.

to reliably use the photon-gun samples. This, combined with the lack of statistics, was seen as suitable reason to use the first discussed technique ("Distorted Inclusive Sample", above) for determining photon $E_{1/2}$ sensitivity.

4.3 Description of Simulation Geometries

4.3.1 Nominal Run 2 Simulation Geometry

After the Run 1 material studies and a number of additional investigations aimed at determining precisely which detector structures were missing or mismodeled in simulation, a new geometry was proposed and implemented into the Monte Carlo code [8]. Figure 28 shows the material difference in data and simulation with this corrected geometry. A number of additional "fine-tuning" adjustments were made to the simulation material in an effort to further reduce material differences, the additional tuning resulting in decreases of "Run 1" material on the order of $0.2 - 0.4 X_0$ in the regions $|\eta| = 1.45 - 1.60, 1.65 - 1.70,$

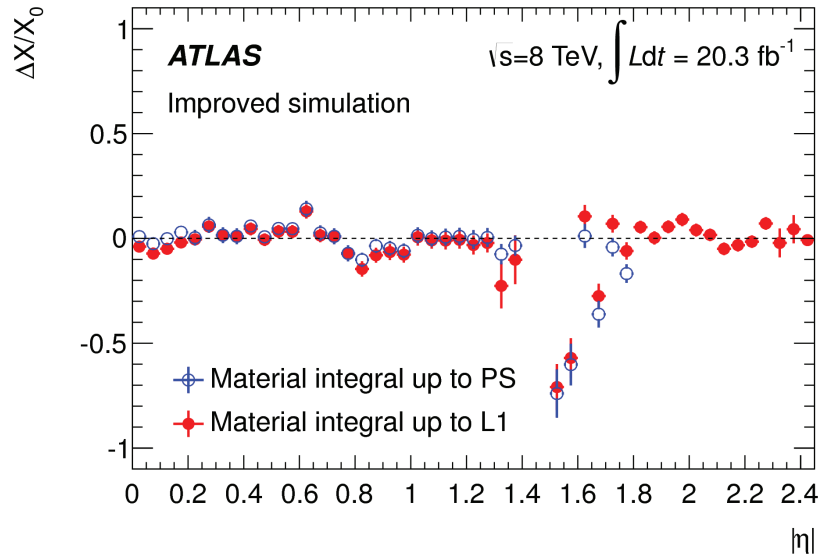


Figure 28: Material difference between data and simulation $\Delta X/X_0$ after applying corrections found in Run 1 study. The solid red points give the material difference up the first layer of the electromagnetic calorimeter, calculated using electrons. The hollow blue points show the material up the presampler, calculated by subtracting the unconverted photon estimation from the electron estimation. Figure from [53].

1.80 – 1.85, with slight increases of material ($< 0.1 X_0$) in between. These changes were made by adjusting the inner detector service material in the simulation crack region to align simulation and data $E_{1/2}$ as closely as possible.

This geometry (with the additional tuning applied) is used as the nominal geometry for Run 1 simulation. In Run 2, the detector saw a number of changes, including a brand new inner tracker layer (the IBL), a new beam-pipe, and several modifications to an inner detector service patch panel (the ‘PP0 region’). These examples are mentioned specifically because they noticeably change the material profile of the region of detector studied here. The nominal Run 2 simulation geometry as it was in the first two years of Run 2 operation (2015-16) includes a number of modifications intended to address these limited changes. It is otherwise identical to the Run 1 nominal geometry.

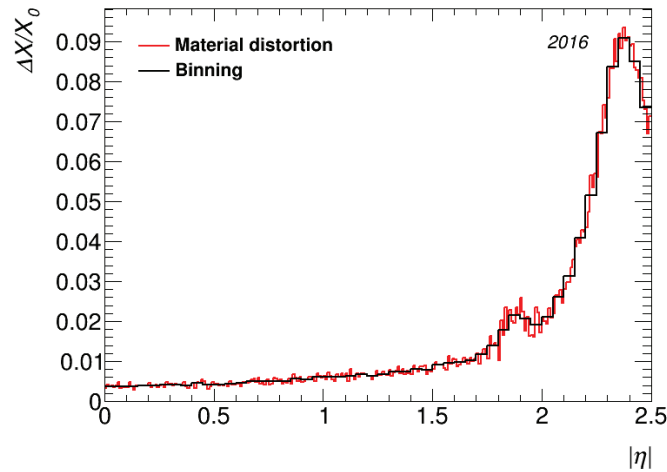


Figure 29: Material difference $\Delta X/X_0$ between the proposed 2016 geometry and nominal simulation geometry in early Run 2.

4.3.2 Development of "2016" Geometries

Before carrying out formal material studies, a few discrepancies in material were noticed early in Run 2 data collection. A preliminary "2016" geometry was constructed with a number of small corrections, mostly in the PP0 and forward regions, which saw the addition of IBL cases and services between Run 1 and Run 2. The study of material in the forward regions ($|\eta| > 2.5$) is a separate subject that is not addressed here. Similarly, additional modifications made to the muon spectrometer are not discussed, as they do not affect the measurements of interest here.

The most relevant features of the new geometry are a 40% increase to IBL material over $|\eta| < 2.5$ and a 50% increase in PP0 material, which dominates for $|\eta| > 1.8$. These increases in material covered the uncertainty (as determined by independent inner detector material investigations) on the simulation mismodelling of these two new detector features at the time. Figure 29 shows the difference in material between the proposed "2016" geometry and the nominal Run 2 geometry.

4.3.3 Distorted Geometry Configurations

Simulation samples with modified geometries are used to quantify the sensitivity of $E_{1/2}$ to variations in material. Given here in Table 6, along with the internal ATLAS geometry tag for each configuration, is a number giving the amount of additional material added in the configuration (usually in percentage of radiation lengths) and a description of the region over which the material was added. Also included are the configuration names (which relate Run 2 changes to similar Run 1 changes) and the production version "s-tags", which are used in dealing with the Monte Carlo samples produced using the distorted geometries. Schematics showing the location of these material distortions in the inner detector are included in the Appendix (Figures 53 – 57). The changes in material as a function of $|\eta|$ for the configuration listed here are plotted in Figure 30.

Table 6: Description of distorted geometries used to calculate sensitivity. Each variation is comprised of one or more distortion "configurations", which are described in the last column. Schematics showing where each geometry distortion is applied in the detector are available in the Appendix A.2 (Figures 53 – 57).

ATLAS geometry tag	Configurations	s-tag	Description
ATLAS-R2-2015-03-01-02	A	s2763	Config A: 5% scale increase to entire inner detector
ATLAS-R2-2015-03-01-11	N	s2764	Config N: +5% X_0 between the presampler and layer 1 in the end-cap region
ATLAS-R2-2015-03-01-12	C' + D'	s2765	Config C': +10% X_0 to pixel (and IBL) services Config D': +10% X_0 to SCT services
ATLAS-R2-2015-03-01-13	E' + L'	s2766	Config E': +7.5% X_0 to SCT/TRT end-cap Config L': +5% X_0 to cryostat in barrel region
ATLAS-R2-2015-03-01-14	F' + M + X	s2767	Config F': +7.5% X_0 to inner detector endplate Config M: +5% X_0 between the presampler and layer 1 in the barrel region Config X: +30% X_0 in the calorimeter end-cap region
ATLAS-R2-2015-03-01-15	G	s2768	Config G: Sum of all of the above configurations

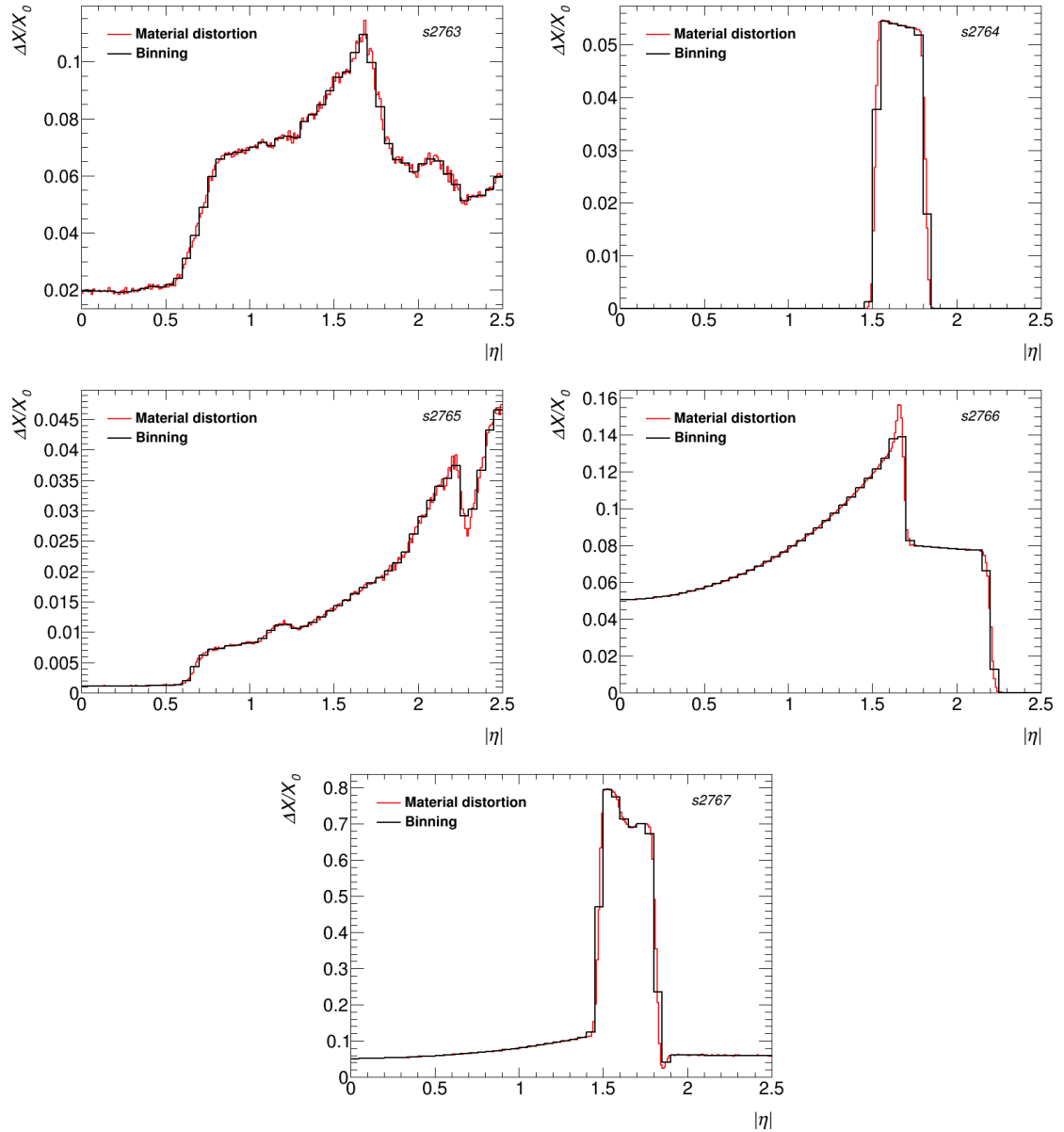


Figure 30: Summary of the material added to the nominal simulation geometry to create all of the distorted geometry configurations used for the electron studies (in red). The black overlay shows the binning used for the purposes of generating a sensitivity curve. A description of each geometry is given in Table 6. Note the different y-axis scaling throughout.

4.4 Selection and Samples

This study used 36.1 fb^{-1} of proton-proton collisions from the LHC (the full combined 2015-16 ATLAS datasets) for all ‘data’ calculations. The electron portion of the analysis was done using full proton-proton Monte Carlo ($Z \rightarrow ee$ samples using release tag 20.7 "MC15c" reconstruction) with normal and distorted geometries. Closely related samples ($Z \rightarrow \mu\mu\gamma$, also release tag 20.7 MC15c) were used for normal-geometry calculations with radiative photons. Higher energy photons were selected from large nominal and distorted geometry inclusive photon samples provided by an external analysis group.

4.4.1 Selection Criteria

Reconstructing the Z boson resonance peak with an electron and positron provides a very reliable check that the selected particles are indeed electrons. As a result, the selection criteria for the electron study is fairly standard for an ATLAS analysis aside from the Z-mass requirement. The full list of criteria is given in given in Table 7. (See Section 3.2.2 for a more detailed explanation of important selection principles like particle identification and isolation.) The requirements applied to the transverse and longitudinal impact parameters d_0 and z_0 are slightly more complicated than simple threshold cuts on the the parameters themselves. The d_0 requirement involves the calculation of a quantity called the d_0 *significance*, which takes into account the uncertainty on the precise point of interaction by considering the beam-spot spread in the transverse plane. Similarly, the z_0 requirement considers the z distance between the particle track and the primary vertex, with the vertex corrected for the reference location of the beam-spot.

Tables 8 and 9 summarize, respectively, the selections for radiative and inclusive photons. For both photon samples, there are two important selection criteria that facilitate

Table 7: Event and electron selection for the $Z \rightarrow ee$ analysis.

Event	
Primary vertex	Check for primary vertex in event
Trigger	2015: "HLT_2e12_lhloose_L12EM10VH" 2016: "HLT_2e17_lhvloose_nod0"
Electron	
p_T	$p_T > 25$ GeV
Cluster quality	Check that the calorimeter cluster passes quality checks
η	$ \eta < 2.47$
Likelihood	Medium
Isolation	Gradient
d_0	$d_0 \text{sig} < 5$
z_0	$ (z_{0,\text{track}} + z_{0,\text{beam-spot}} - z_{0,\text{vertex}}) * \sin(\theta_{\text{track}}) < 0.5$ mm
Z	
Two candidates	Exactly two opposite sign electrons
Mass	$66 < m_{ee} < 116$ GeV
Trigger match	Check that a selected electron fired the required trigger

the probing of the region between the presampler and first layer of the EM calorimeter: choosing only unconverted photons and requiring that the (raw) energy deposited in the presampler is less than 500 MeV (the ‘presampler veto’). Unconverted photons, reconstructed purely from their shower cluster in the electromagnetic calorimeter, show no evidence of interaction with the inner detector material. They are more sensitive to upstream material specifically than other photons. The presampler veto $E_{0,\text{raw}} < 500$ MeV screens out events where the photon shower is initiated by material before the presampler. Combining these two conditions selects photons that have little interaction with inner detector material and initiate a shower somewhere between the presampler and EM calorimeter. This allows for the probing of material in that region alone.

For the radiative process $Z \rightarrow \mu\mu\gamma$, selection requirements are necessary for muons, photons, and the parent Z particle. A notable feature of the selection is the restriction on the mass of the two muons $40 < m_{\mu\mu} < 81$ GeV. This restriction, paired with a tight

Table 8: Selection for radiative photons ($Z \rightarrow \mu\mu\gamma$ events).

Event	
Primary vertex	Check for primary vertex in event
Detector quality	Pass LAr, Tile, and core quality checks.
Trigger	2015: "HLT_mu18_mu8noL1" 2016: "HLT_mu22_mu8noL1"
Muon	
p_T	$p_T > 10$ GeV
η	$ \eta < 2.7$
Likelihood	Medium
Isolation	Loose
d_0	$d_0 sig < 10$
z_0	$ (z_{0,track} + z_{0,beam-spot} - z_{0,vertex}) * \sin(\theta_{track}) < 0.5$ mm
Photon	
Type	Unconverted
p_T	$p_T > 10$ GeV
η	$ \eta < 2.5$
Likelihood	Tight
Isolation	FixedCutTight
$E_{0,raw}$	$E_{0,raw} < 500$ MeV
Z	
Three candidates	One photon and two opposite sign muons
Mass	$40 < m_{\mu\mu} < 81$ GeV $81 < m_{\mu\mu\gamma} < 101$ GeV
Trigger match	-

window on the Z mass $81 < m_{\mu\mu\gamma} < 101$ GeV, helps to limit the selection of particles from non-radiative $Z \rightarrow \mu\mu$ decays. The photon selected in that case is often from final-state radiation of the muon pair, so the combined mass $m_{\mu\mu\gamma}$ does not yield the familiar Z peak.

4.4.2 Kinematic Distributions

Kinematic variable distributions provide a description of the phase space covered by the analysis and can be used to verify important aspects of the selection criteria.

Table 9: Selection for inclusive photons.

Photon	
Type	Unconverted
p_T	$p_T > 145 \text{ GeV}$
η	$ \eta < 2.5$
Likelihood	Tight
Isolation	FixedCutTight
$E_{0,raw}$	$E_{0,raw} < 500 \text{ MeV}$

Electron Distributions

The shape of the Z invariant mass resonance (Figure 31, top) is well understood in data and simulation, providing a useful way to validate the analysis code and check for successful $Z \rightarrow ee$ selection. The $Z \rightarrow ee$ selection defines the energy regime of electrons used in this analysis, which is corroborated by the single-electron p_T distribution (Figure 31, bottom).

Photon Distributions

With radiative photons selected correctly from a $Z \rightarrow \mu\mu\gamma$ decay, the combined invariant mass of the photon and muon pair returns the familiar Z resonance (Figure 32, top). The $m_{\mu\mu}$ distribution is given as well (Figure 32, bottom). Without a restriction on $m_{\mu\mu}$, this distribution would show a Z resonance peak from $Z \rightarrow \mu\mu$ muons, which should not be included in the analysis. (The radiative photon simulation sample is statistically limited for photons with $p_T > 70 \text{ GeV}$, and no additional simulated background samples are included, so some expected differences in $m_{\mu\mu}$ are visible between data and simulation.) Figure 33 highlights the difference in p_T between the radiative and inclusive photon samples.

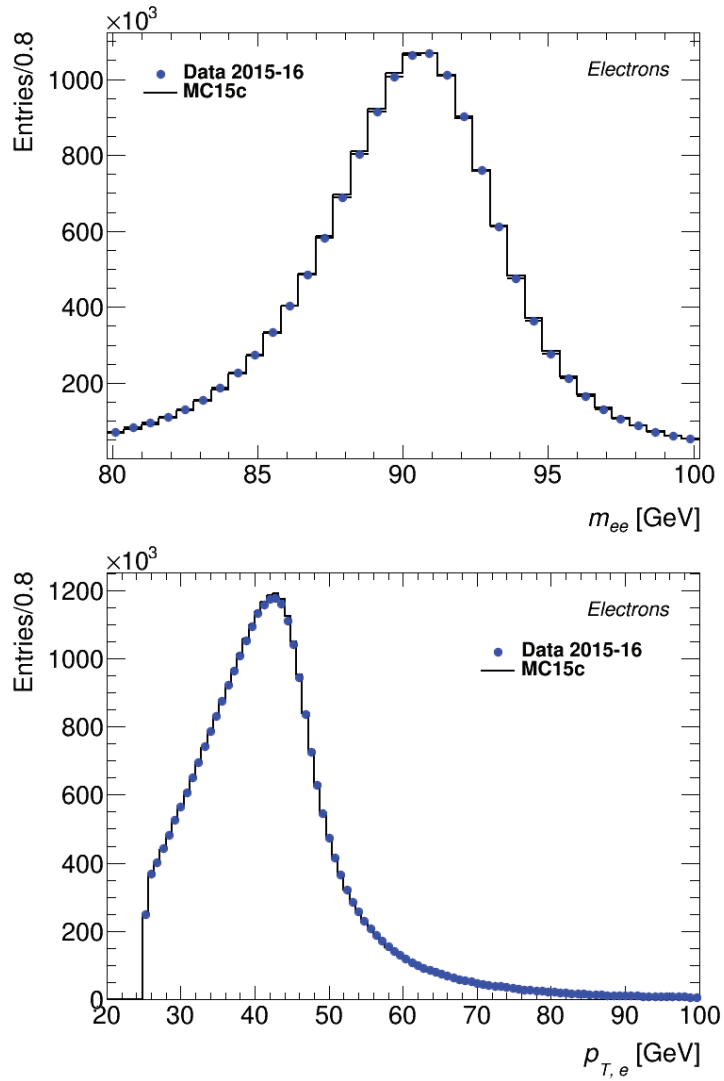


Figure 31: Combined invariant mass m_{ee} (**top**) and single-electron p_T (**bottom**) in data and simulation for the $Z \rightarrow ee$ electron selection.

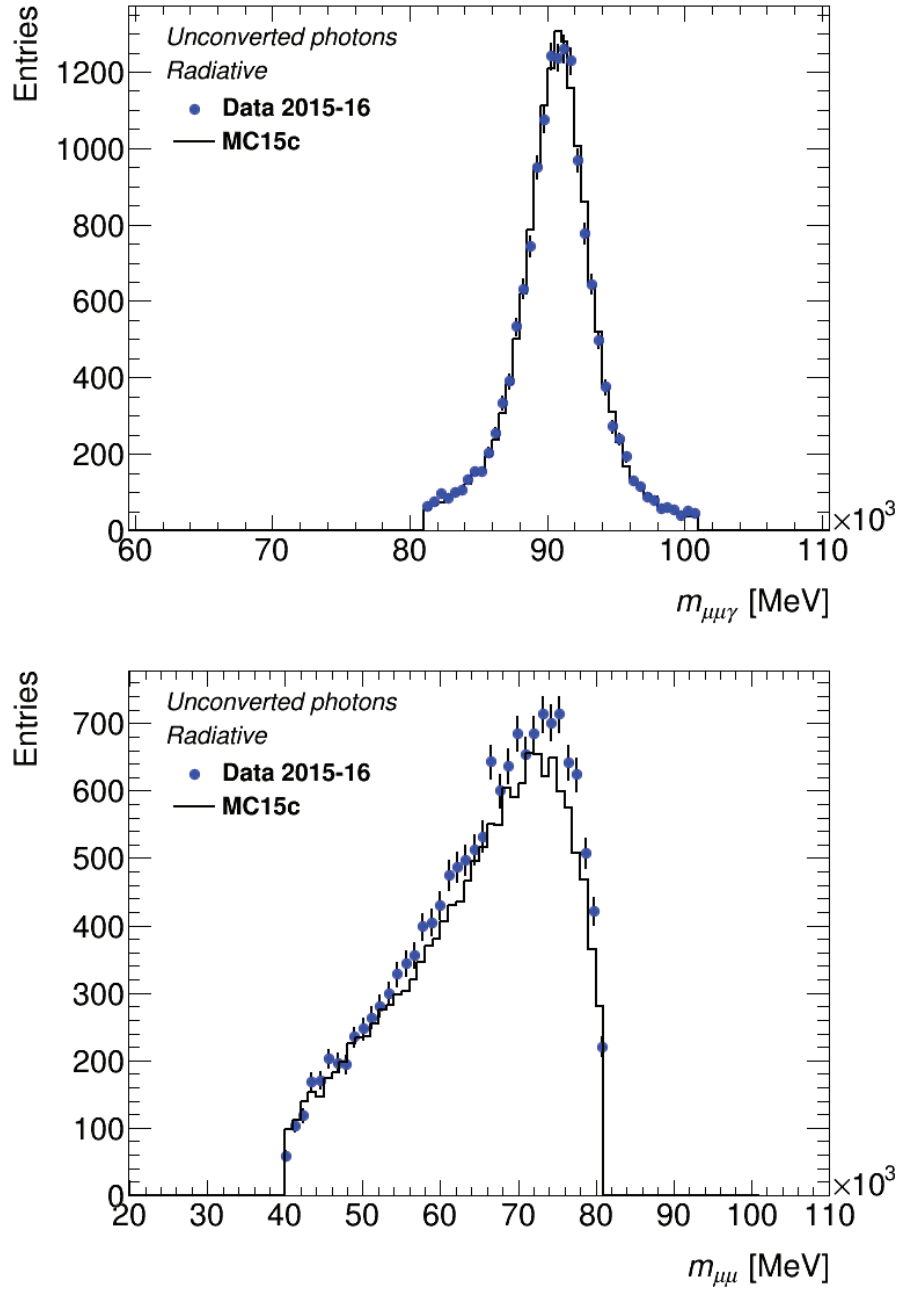


Figure 32: **Top:** $m_{\mu\mu\gamma}$ (invariant mass) in data and simulation for $Z \rightarrow \mu\mu\gamma$ radiative photon selection. **Bottom:** $m_{\mu\mu}$ for the same.

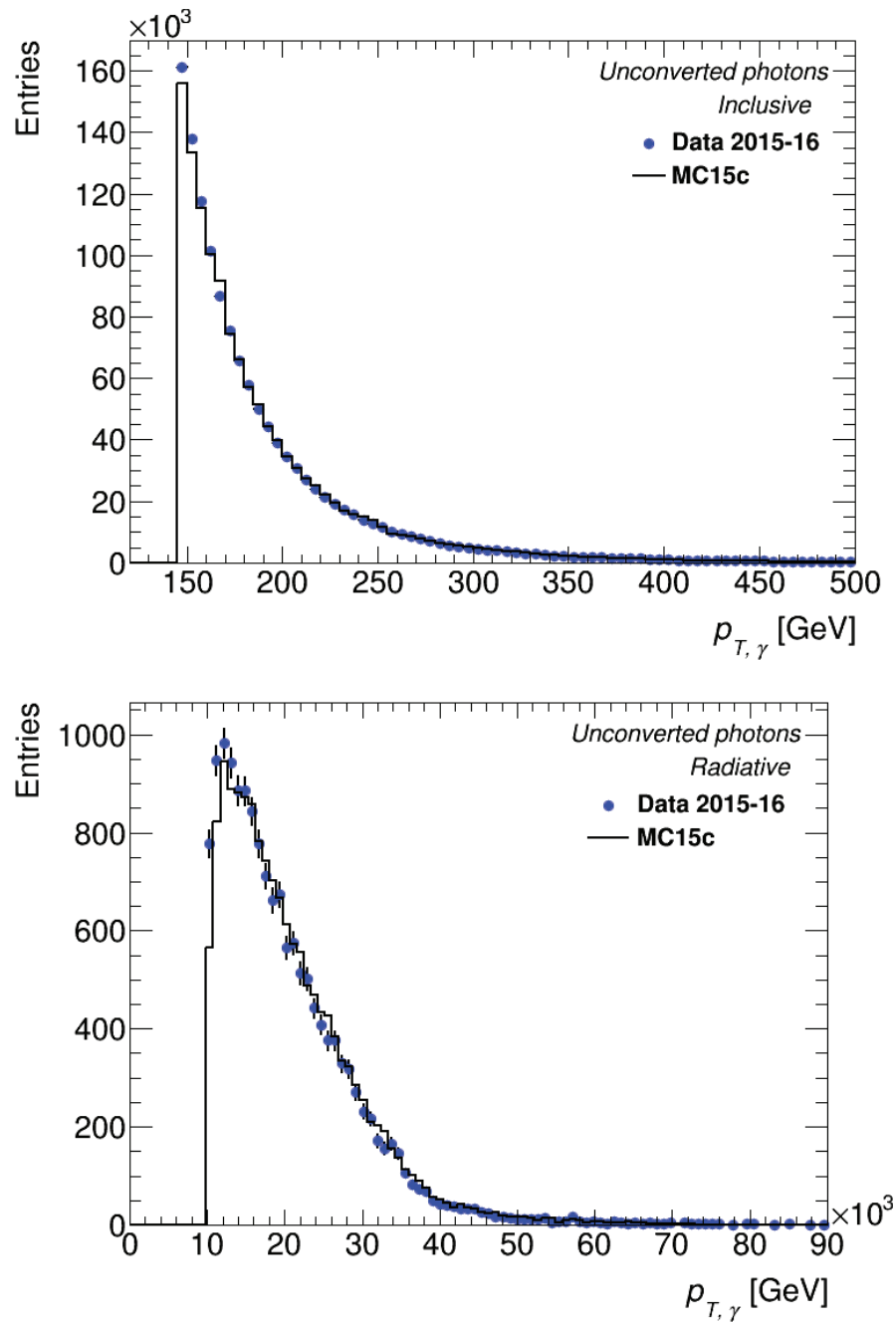


Figure 33: Photon p_T in data and simulation for inclusive (**top**) and $Z \rightarrow \mu\mu\gamma$ radiative (**bottom**) photon selection.

4.5 Passive Material Determination with Electrons

This section covers the primary material estimation results obtained using electrons. Also included are an investigation of the material discrepancies in ϕ and two brief studies related to previously established material systematic uncertainties. The next section (Section 4.6) covers the photon studies, including a combination of electron and photon estimates.

4.5.1 Sensitivity Results

The relative difference in electron $E_{1/2}$ between data and simulation is calculated via Equation 23. This quantity is shown in Figure 34 before and after applying layer corrections. To reiterate, this quantity represents the difference in $E_{1/2}$ (as a function of $|\eta|$) between the full 2015+2016 datasets and several million events in a full proton-proton collision simulation of the detector. (See Figure 25 for the data and simulation $E_{1/2}$ profiles from which the relative difference is calculated.)

Sensitivities are calculated (see Equation 25) as a function of $|\eta|$ for each of the geometries given in Table 6. The $E_{1/2}$ profile distributions from which the relative differences are calculated are included in the Appendix (Figures 58 – 62). For $|\eta|$ ranges where there is a very small change in material, it is expected that the change in $E_{1/2}$ will be negligible. This can cause unstable behaviour for the sensitivity, which contains the difference in $E_{1/2}$ in the denominator, and so diverges as the quantity approaches zero. To remove sensitivities that might have been impacted by this effect, only the regions where the expected change in material is greater than $0.015\%X_0$ are taken from a given distorted geometry. Figure 35 (top) shows the curve obtained with each distorted geometry after excluding points that do not satisfy this requirement. Differences can be observed in the curves produced by each geometry variation. In order build a single sensitivity curve that reasonably accounts for

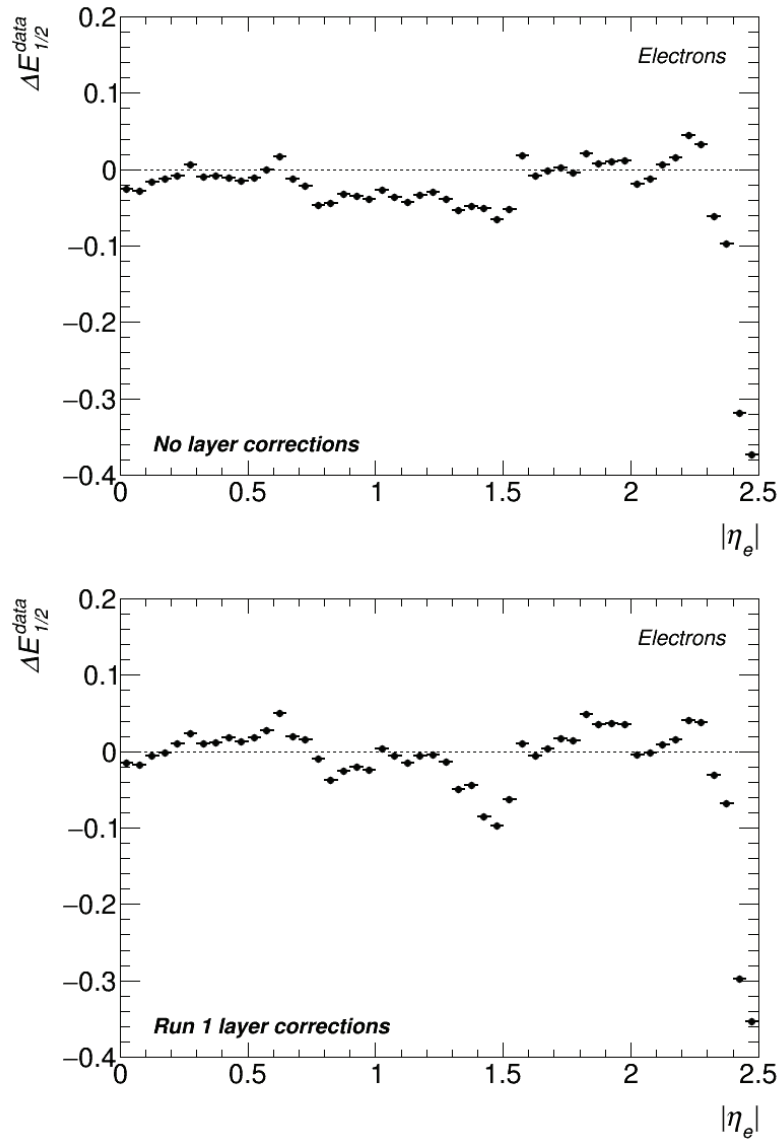


Figure 34: Relative difference of electron $E_{1/2}$ in data and simulation, shown before and after applying layer calibrations. The full 2015+2016 datasets are used. Note that this quantity is equivalent to the ratio of $E_{1/2}$ in data and simulation shifted down by one unit.

how $E_{1/2}$ changes with different kinds of material differences, the curves are averaged. The sensitivities are combined via a weighted average (calculated bin-by-bin, using the squared inverse of each point's error as its weight) to yield a final sensitivity. This average (bottom plot in Figure 35) is used to make the material estimate for electrons.

This sensitivity curve shows a steady increase from ~ 2.5 to ~ 4 in the region

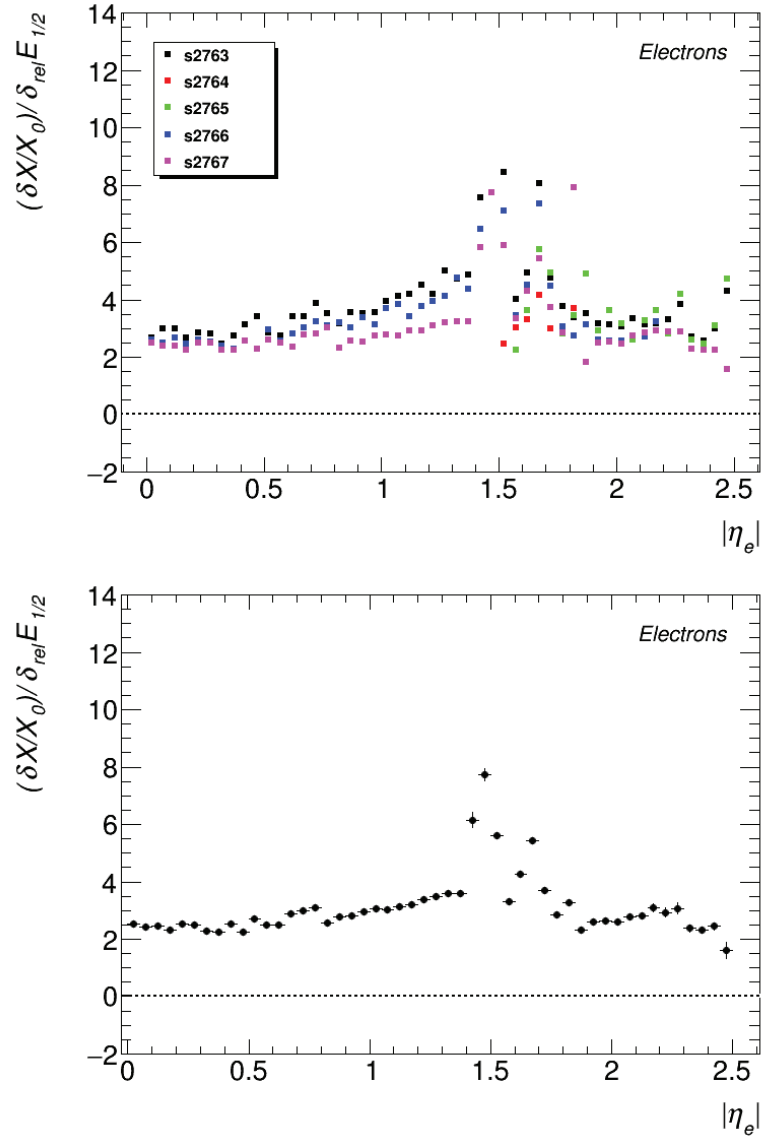


Figure 35: **Top:** Electron $E_{1/2}$ sensitivity to material differences, calculated as the ratio of change in material to relative difference in $E_{1/2}$. Sensitivity curves are given for five different distorted geometries, identified here by s-tag (see Table 6). The change in material is given in numbers of radiation lengths. **Bottom:** Electron $E_{1/2}$ sensitivity averages. Average is calculated over the five sensitivity curves shown in top plot, calculated bin-by-bin as a weighted average using the inverse-square of the error as the weight.

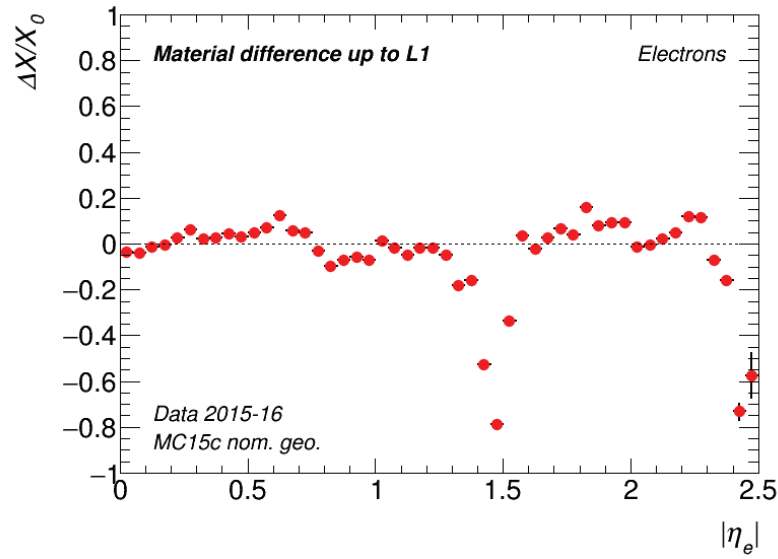


Figure 36: Estimate of the difference in detector material up to the first layer of the EM calorimeter (L1) between data and nominal simulation geometry. The material difference is given in numbers of radiation lengths. Y-axis error bars are present throughout. (In most cases the bars are obscured behind the width of the point.)

$0.0 \leq |\eta| < 1.4$ before plateauing at high values in the crack region, then dropping down to roughly 2.5 in the end-cap. This agrees well with the distribution obtained in previous studies (shown in parameterized form in Figure 19 of the Run 1 calibration paper [53]).

4.5.2 Passive Material Estimates

Combining the relative difference (Figure 34, top) with the averaged sensitivity (Figure 35, bottom) in the manner described in Section 4.2.1 gives an estimate of the material differences up to the first layer of the calorimeter. Figure 36 shows this estimate. Points below the zero line suggest a surplus of material in simulation at that $|\eta|$. Points above suggest a deficit. As an example, the small peak at $|\eta_e| = 0.6$ indicates a $0.15 X_0$ (roughly) excess of material in data. This estimate suggests discrepancies in material throughout, particularly in the crack region ($1.25 < |\eta| < 1.6$), which shows an excess of material in simulation, and in the region $|\eta| > 1.8$ where there are several additional variations.

Comparing with the material difference plot from Run 1 studies and taking into account the additional fine-tuning (see Section 4.3.1 for a description of the changes made by fine-tuning) provides a way of investigating the differences in measured material between Run 1 and Run 2 and checking against known differences in the detector. The comparison suggests differences primarily at high $|\eta|$, after the crack region. (The crack region itself shows a few differences, too. This is a region rich in passive material and is notoriously difficult to model well. It was also modified by the late fine-tuning.) The differences at high $|\eta|$ are expected, due to the installation of additional services material in the PP0 region of the detector.

4.5.3 Systematic Uncertainty Checks

A short study was performed to check if the material differences measured in Run 2 can be accounted for by known systematic uncertainties. The material systematic uncertainties from Run 1 studies include a combination of correlated and data-driven (uncorrelated) uncertainties addressed thoroughly in the Run 1 calibration efforts [53]. The primary contributions to the correlated aspects of the material systematic uncertainties are L1/L2 layer intercalibration uncertainties¹⁰ and Geant4 simulation uncertainties. The uncorrelated, data-driven contributions to the material systematic uncertainties are determined in material studies like that presented in this document. The determination of these uncertainties is covered in Section 4.7.2.

An additional source of systematic uncertainty has been established for Run 2 material studies, originating from known discrepancies in the PP0 region simulation geometry. The uncertainty is taken as the difference in material between ATLAS-R2-2015-03-01-00

¹⁰ Examples of sources of correlated systematic uncertainties in the Run 1 L1/L2 intercalibration include (but are not limited to) the reduced electric field between calorimeter layers, differences between muon and electron $E_{1/2}$, and the presence of cross-talk between calorimeter cells. See [53] for the complete list.

(MC15c nominal) and ATLAS-R2-2016-00-01-00 (proposed MC16, see Figure 29) with an additional 2.5 scaling factor for $|\eta| > 1.5$ to correct for an underestimate in the "proposed MC16" geometry.

Figure 37 shows the Run 2 material difference (from Figure 36) against systematic uncertainties from Run 1 and Run 2. The Run 1 systematic uncertainties are calculated such that, in $|\eta|$ bins where the material difference is large, the systematic uncertainty is defined as the material difference itself. It is important to note that these uncertainties were calculated prior to the introduction of the fine-tuning discussed in Section 4.3.1. The discrepancy at $|\eta| = 1.8$ is likely explained by this, since the fine-tuning at this $|\eta|$ includes a decrease in simulation material relative to the geometry configuration used in the generation of systematic uncertainties. This would lead to a increase in $E_{1/2}$ data/simulation ratio. It is reasonable to conclude, then, that the Run 2 material differences are well accounted for by known Run 1 and Run 2 systematic uncertainties.

Another study was completed to check the effect of switching to the new 2016 geometry (ATLAS-R2-2016-00-01-00, with s-tag s2984) on the $E_{1/2}$ agreement in data and simulation. This geometry distortion is closely related to the Run 2 systematic uncertainties checked above. The top plot in Figure 38 shows the relative difference between data and simulation for both MC15c and MC16 geometries. The plot on the bottom gives the difference between these two quantities. The updated geometry (which was created to correct for IBL and PP0-region material mismodelling in previous versions of the simulation geometry) shows improved agreement with $E_{1/2}$ in data, as expected.

4.5.4 Results in ϕ

Previous studies have not investigated possible material differences in ϕ . A careful investigation of this kind would require a great deal of additional calibration, as the current suite of

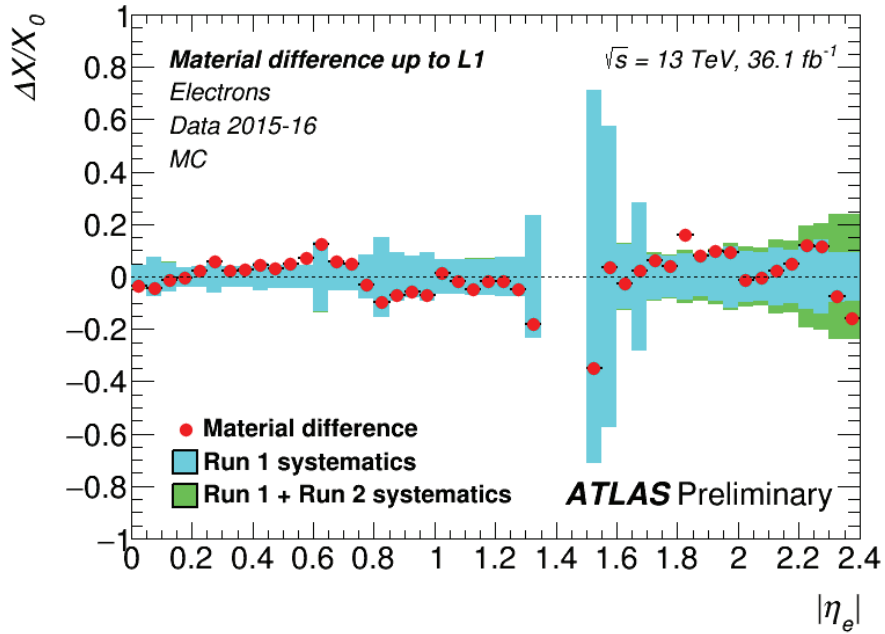


Figure 37: Measured Run 2 material difference between data and nominal simulation geometry against previously used systematic uncertainties. The blue band summarizes the set of correlated and data-driven uncorrelated material uncertainties established in previous Run 1 studies. These uncertainties are not available for $|\eta| > 2.4$. The green band includes a set of new systematics associated with increased PP0 material in Run 2. The study was not performed in the crack region (bins from 1.35 – 1.50), which is commonly excluded from physics analyses.

tools is equipped with corrections that are uniform across ϕ . Nevertheless, measurements of $E_{1/2}$ in η and ϕ combined with the averaged sensitivity curve (which is only calculated as a function of $|\eta|$) provides a first qualitative check for potential material differences in ϕ . Figure 39 shows the material difference as a function of both η and ϕ .

This plot shows, among other things, a periodic deficit in simulation material at $|\eta| = 0.6$. A candidate structure has been identified in the detector that is absent in simulation, possibly leading to these deficits. Work is in progress to determine if adding these to the simulation geometry accounts for the missing material.

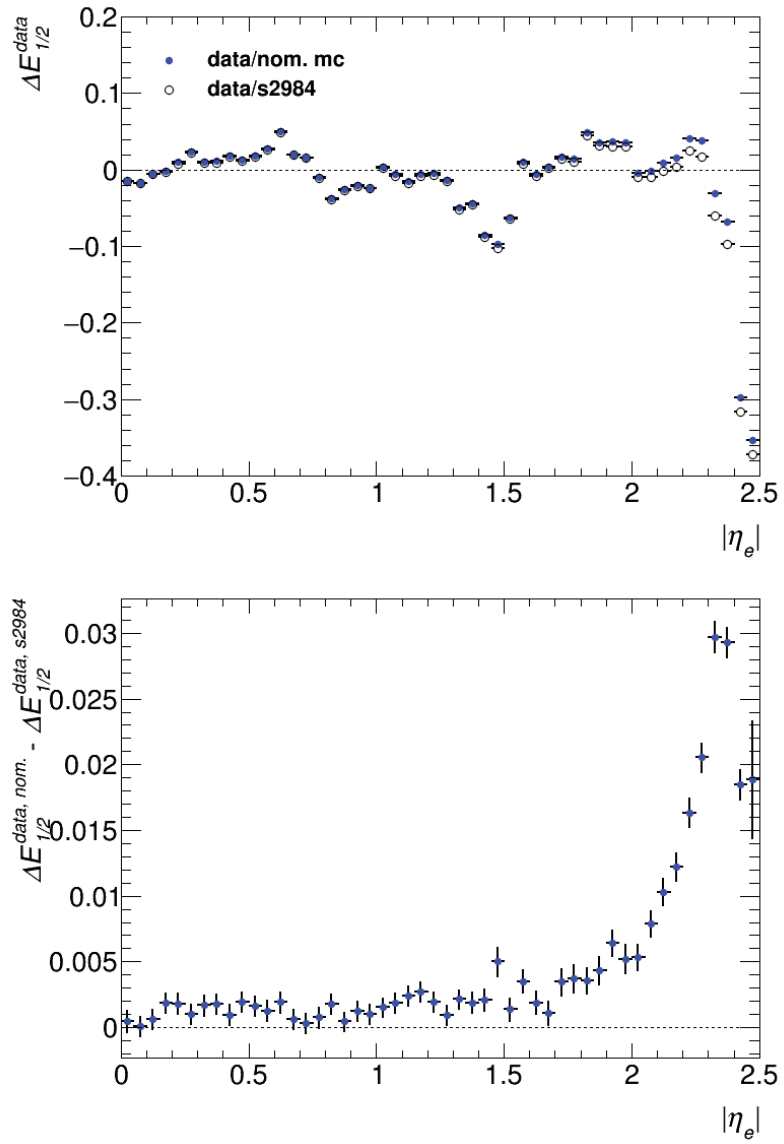


Figure 38: Comparison of nominal MC15c with an updated MC16 geometry (s2984). The top plot shows the $E_{1/2}$ ratio with data for each simulation geometry, and the bottom plot shows the difference in these quantities.

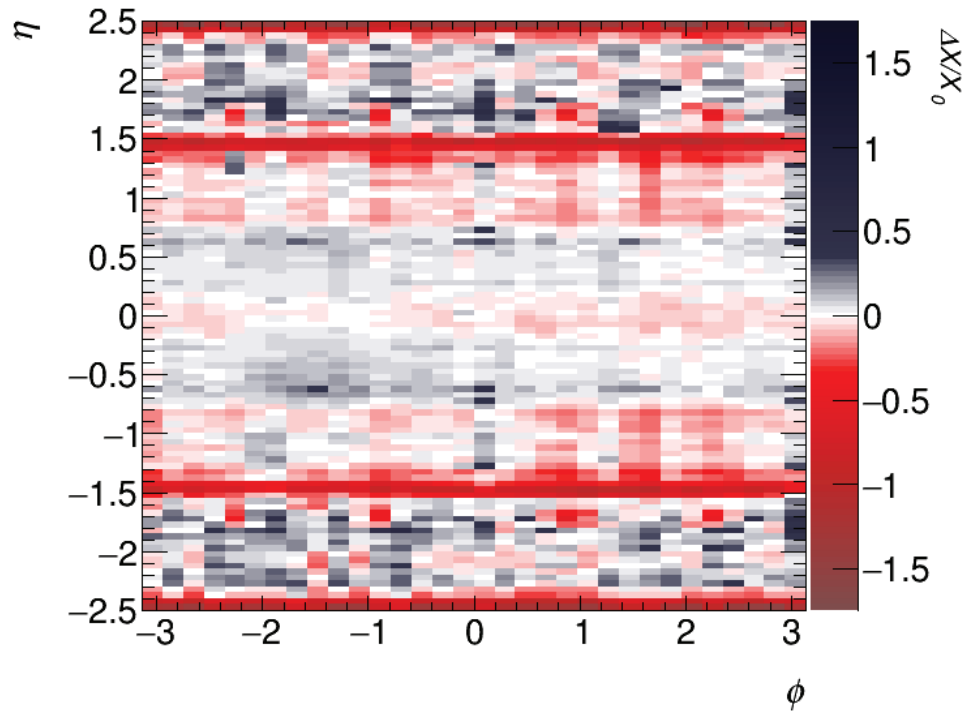


Figure 39: Passive material difference in ϕ and η between data and simulation before the EM calorimeter accordion. The sensitivity (Equation 25) is determined purely as a function of $|\eta|$, as in Figure 35. The colour scale represents the same quantity as the y-axis in Figure 36: negative (red) values indicate a surplus of material in simulation, positive (blue/black) a deficit.

4.6 Passive Material Determination with Photons

4.6.1 E_1/E_2 Results

To help mitigate the reduced statistics in the available photon samples, the $|\eta|$ bin size is increased relative to the size used in the electron studies. For most of the $|\eta|$ range, the bin size is increased from $\Delta|\eta| = 0.05$ to $\Delta|\eta| = 0.2$. The last three bins are adjusted to isolate the crack region, which is excluded from the analysis entirely due to a lack of statistics and useful distorted geometries. The last three bins are defined by boundaries at $|\eta| = 1.20, 1.35, 1.55,$ and 1.80 . Figure 40 gives the $E_{1/2}$ profiles for the inclusive (top) and radiative (bottom) unconverted photon samples.

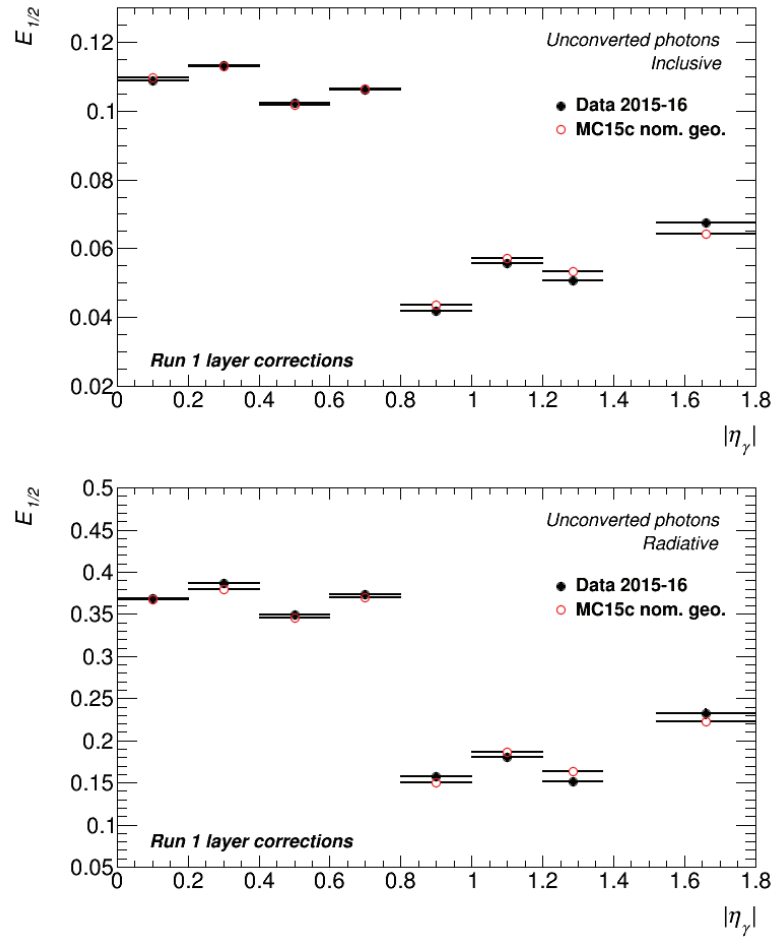


Figure 40: Comparison of $E_{1/2}$ profiles for unconverted photons in data and nominal geometry simulation. Each point gives the mean value of the $E_{1/2}$ distribution for a given bin in $|\eta|$. The plot on the top uses high p_T (>145 GeV) photons from a prepared inclusive single photon sample. The plot on the bottom uses photons from radiative Z decays. The nominal geometry in MC15c is identified internally with geometry tag ATLAS-R2-2015-03-01-00 (see Table 6).

The relative difference of these profiles is shown in Figure 41, along with their weighted average. The weight was taken as $1/error^2$. The errors are statistical here, so the average tends towards the inclusive photon sample, which has a significantly larger number of photons.

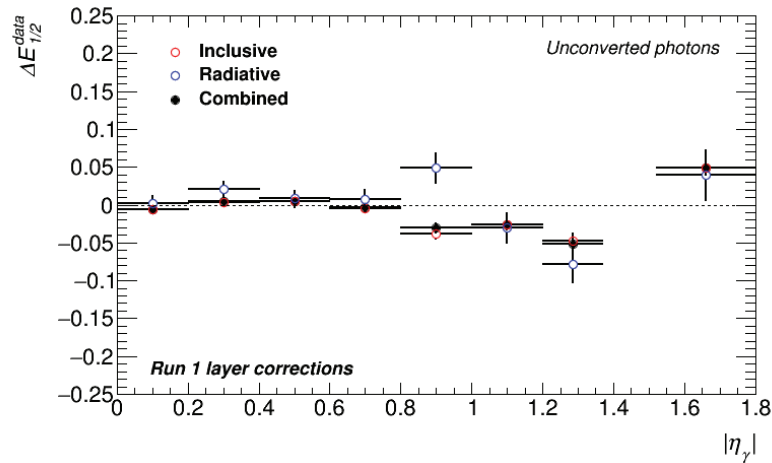


Figure 41: Relative difference of $E_{1/2}$ in data and simulation for both radiative and inclusive photons. The values from both are combined with a weighted average.

4.6.2 Sensitivity Results

The photon $E_{1/2}$ sensitivity to material differences is calculated using a distorted geometry inclusive photon sample as described in Section 4.2.2. The $E_{1/2}$ profile of the distorted sample is shown against the profile of the nominal sample in Figure 42 (top). Also shown is the relative difference of the two distributions (bottom).

To determine the sensitivity, this relative difference is divided into the difference in material between the nominal and distorted geometries. (Recall that the photons are all "unconverted" and subject to the presampler veto, so out of all the extra material added in the inclusive photon distorted geometry sample (configuration G) only configurations that add extra material between the presampler and first layer of the electromagnetic calorimeter (configurations M and N) will affect shower development.) Figure 43 shows the relevant difference in material between geometries with the photon $|\eta|$ binning.

Figure 44 shows the photon $E_{1/2}$ sensitivity curve. The curve was parameterized as a straight line using a least squares regression over the region $|\eta| < 1.37$. The fitted line is shown over the points used to perform the fit in Figure 44.

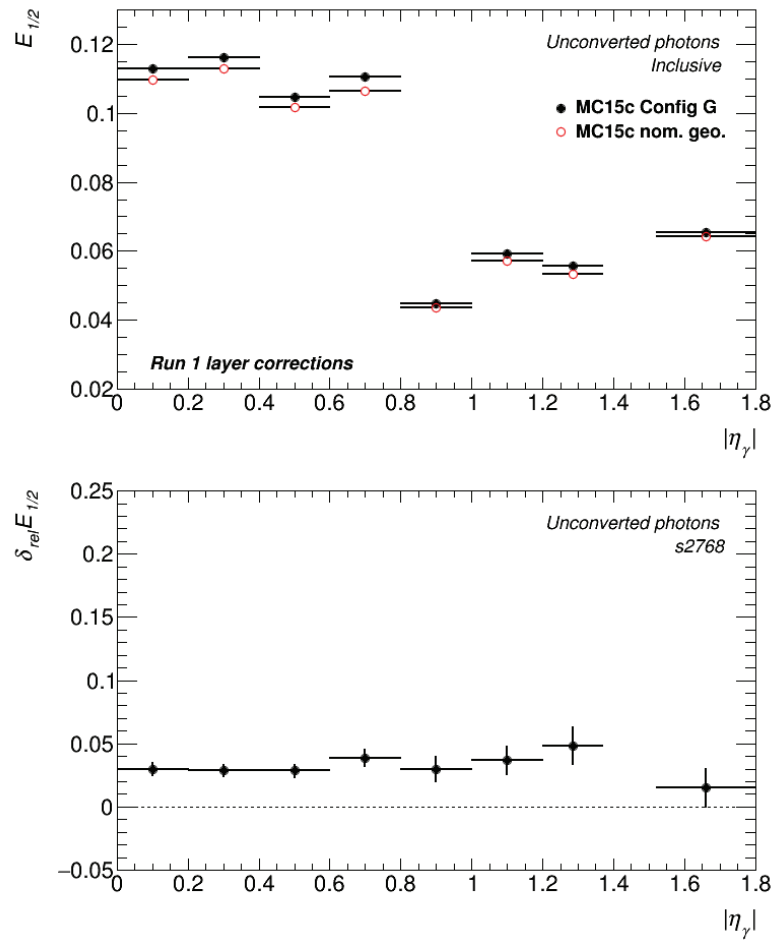


Figure 42: **Top:** $E_{1/2}$ for photons in distorted (s-tag s2768) and nominal geometry simulation (solid black and hollow red circles, respectively). **Bottom:** The relative difference in $E_{1/2}$ between these two simulation samples.

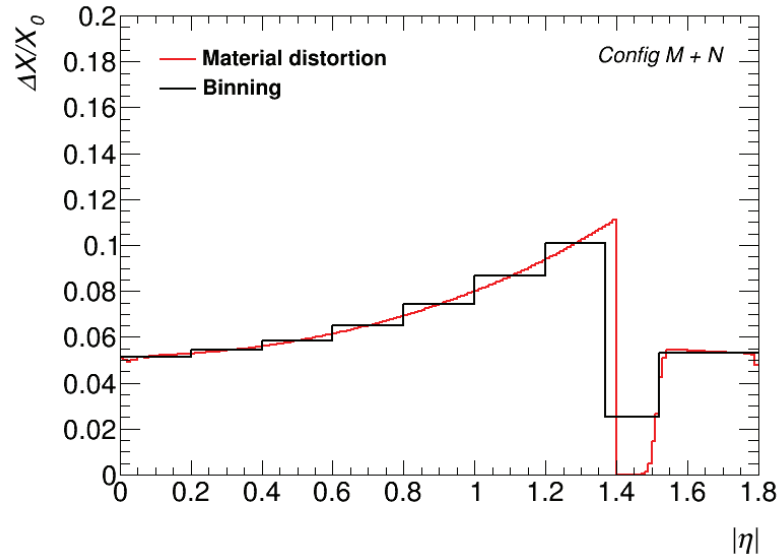


Figure 43: The material distortions in configuration G that are probed by unconverted photons with the $E_{0,raw} < 500$ MeV presampler veto: (configurations M and N). The crack region bin ($|\eta| = 1.37 - 1.52$) is not used in the analysis. The red line shows the increased material in the distorted geometries, and the black histogram gives the binning used in the analysis.

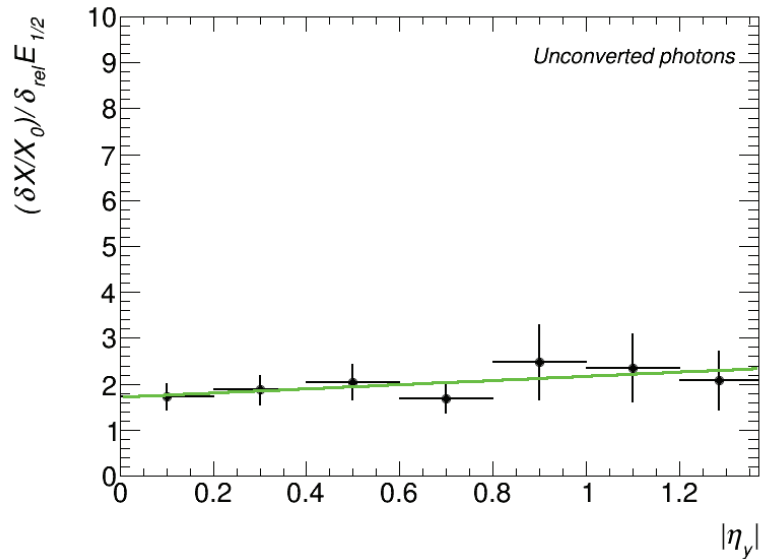


Figure 44: Photon $E_{1/2}$ sensitivity to material differences with a straight line parameterization overlaid (green). Values along this parameterization line are used as the sensitivity.

4.6.3 Passive Material Estimates

A material estimate is calculated as in Equation 26 using the relative difference and sensitivity results given in Figure 42 (bottom) and Figure 44. The fitted line in Figure 44 is used for bin sensitivities, with uncertainties propagated through from the errors on the linear fit parameters. The resulting estimate (Figure 45) showed statistically significant differences in material. Although very nearly accounted for by the uncertainties, the material estimate shows a slight deficit in simulation material in the region $|\eta| < 0.80$ and an excess over $0.8 < |\eta| < 1.37$. A large deficit is suggested at high $|\eta|$, but the uncertainty would need to be reduced before conclusively identifying it.

Unconverted photons are used to probe the region in between the presampler and accordion. Electrons are sensitive to all material before the accordion. Subtracting the photon result from the electron result, then, gives an estimate of the material in the region before the presampler. Figure 46 shows two material estimates, one for all the material up to (and including) the presampler and the other extending slightly further, covering all material up to the first accordion layer. The material difference estimates do suggest the existence of some material discrepancies in the region between the presampler and first layer of the EM calorimeter, but further work is required to reduce the uncertainties on the measurement and allow for confident distinction between the region up to the presampler and the region up to the first layer.

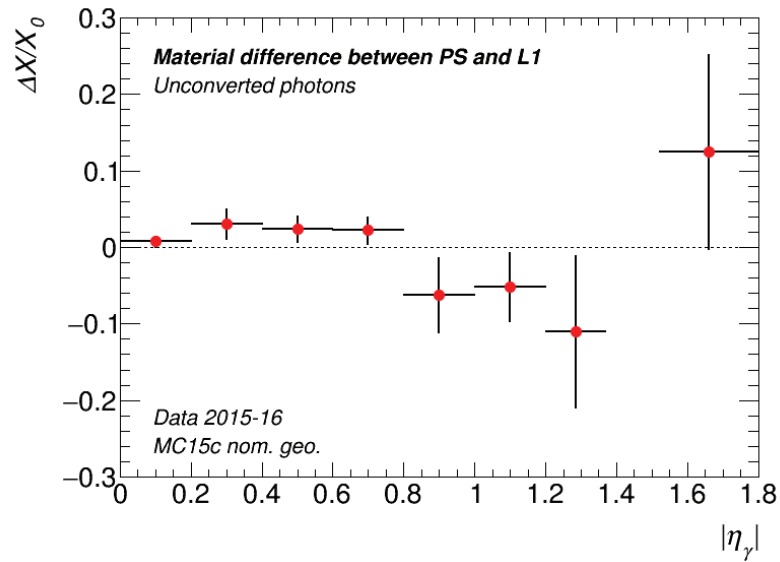


Figure 45: Estimate of the difference between data and nominal simulation geometry for material in the region between the presampler and the first layer of the EM calorimeter. The material difference is given in numbers of radiation lengths.

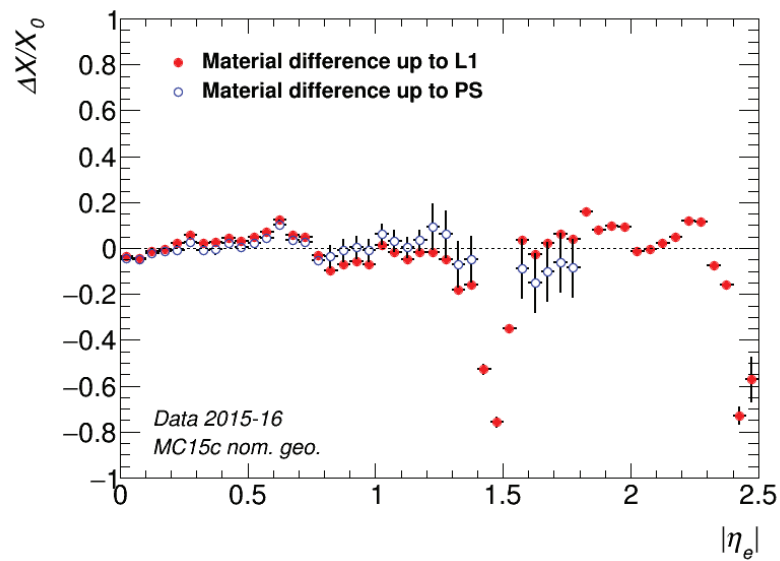


Figure 46: The electron and photon results are combined to estimate the material difference up to the presampler (blue). This estimate is presented along with the estimate of material difference up to the first layer of the electromagnetic calorimeter (red).

4.7 Impact on Energy Scale Uncertainty

4.7.1 Material Contribution to Uncertainties

Uncertainties in the material are most useful to an ATLAS physics analysis expressed as contributions to uncertainties on the energy scale α (recall Equation 21 in the discussion of energy calibration). A material uncertainty δX can be converted to an energy scale uncertainty $\delta\alpha$ using a simple proportionality relation

$$\delta\alpha = \delta X \left(\frac{\Delta\alpha}{\Delta X} \right). \quad (27)$$

The ratio $\frac{\Delta\alpha}{\Delta X}$ gives the rate at which the energy scale changes as the amount of material in relevant detector ranges changes. In a manner similar to the calculation of the $E_{1/2}$ sensitivity (Equation 25), α is calculated with a distorted geometry simulation and the result is compared with energy scales calculated from nominal geometries. The energy scale difference $\Delta\alpha$ is divided by the known material difference ΔX , yielding the energy scale sensitivity to differences in material. The calculation of these sensitivities is not covered in this study. (See e.g. reference [53] for a description of how energy scales are determined.)

A portion of the material uncertainty δX is calculated from the material difference estimates shown in Figure 46 (the procedure used in this study for determining them was also used in the Run 1 studies). The full material uncertainty δX also contains a number of correlated errors arising from the layer intercalibration studies and Geant4 simulation. These are not discussed here, as they are determined by other means. To simplify the following discussion, δX is taken as synonymous with the data-driven, uncorrelated portion of the full uncertainty.

A useful definition for the data-driven uncertainty δX would reflect the errors on the original difference estimate and also sufficiently cover the magnitudes of the differences in regions with large data/simulation discrepancies. With this in mind, the method used to determine the uncertainty differs depending on whether or not there is a statistically significant material difference (or in other words, whether or not the error bars of a point in Figure 46 include the zero line). If there is no statistically significant difference, the error on the point is taken as δX . If there is a significant difference, δX is defined as the difference between the point and the zero line.

To take advantage of previous material studies and allow for various simplifications in the formal calculations, the total material contribution to energy scale uncertainty is broken down into contributions from separate detector regions. For the purposes of calculating the uncertainties, the detector is broken down radially into the regions listed in Table 10. Due to the limited range of the presampler, the definitions of some regions vary in $|\eta|$. Specifically, the "Cryo" term describes different detector regions in and out of the presampler acceptance regions ($|\eta| \leq 1.8$ or $|\eta| > 1.8$, respectively). Where the distinction is important, an additional subscript (*PS* or *L1*, as defined in Table 10) indicates the specific region. The "Calo" term does not contribute outside of the presampler acceptance range.

The total energy scale uncertainty comes from the sum of individual contributions from material uncertainties in these regions. While the "Calo" material is probed separately using unconverted photons, the "ID" and "Cryo" regions are not measured independently, and so are assumed correlated. Thus the total energy scale uncertainty is given by Equation 28:

$$\delta\alpha_{tot}^2 = \delta\alpha_{ID}^2 + \delta\alpha_{Cryo}^2 + \delta\alpha_{Calo}^2 + 2cov(\delta\alpha_{ID}, \delta\alpha_{Cryo}). \quad (28)$$

¹¹ "Calo" is used to describe the region between the presampler and first layer of the calorimeter. Since the presampler only extends out to $\eta = 1.8$, there is no way to define this region for $1.8 < |\eta| < 2.5$. This means that in the pseudorapidity range $0.0 < |\eta| < 1.8$, there are three regions: "ID", "Cryo_{PS}", and "Calo". In the pseudorapidity range $1.8 < |\eta| < 2.5$, there are only two: "ID" and "Cryo_{L1}".

Table 10: Summary of detector regions for the calculation of uncertainties. The last column provides the names of the distorted geometry configurations that feature additional material in the named region of the detector. (Refer to Table 6 for descriptions of the geometry configurations.)

Region	Pseudorapidity	Description	Configurations
Inner Detector (ID)	$0.0 < \eta < 2.5$	From the interaction point out to the cryostat.	A
Cryostat (Cryo)	$0.0 < \eta < 1.8$	Between the envelope of the ID and the inner edge of the presampler. (<i>Cryo, PS</i>)	L', X
	$1.8 < \eta < 2.5$	Between the envelope of the ID and the first layer of the EM calorimeter. (<i>Cryo, L1</i>)	E', F'
Calorimeter (Calo)	$0.0 < \eta < 1.8$	Between the outer edge of the presampler and the first layer of the EM calorimeter.	M, N
	$1.8 < \eta < 2.5$	Undefined. ¹¹	

Using Equation 27, each contribution can be expressed in terms of a material uncertainty:

$$\begin{aligned} \delta\alpha_{tot}^2 = & \left(\delta X_{ID} \frac{\Delta\alpha_{ID}}{\Delta X_{ID}} \right)^2 + \left(\delta X_{Cryo} \frac{\Delta\alpha_{Cryo}}{\Delta X_{Cryo}} \right)^2 + \left(\delta X_{Calo} \frac{\Delta\alpha_{Calo}}{\Delta X_{Calo}} \right)^2 \\ & + 2 \frac{\Delta\alpha_{ID}}{\Delta X_{ID}} \frac{\Delta\alpha_{Cryo}}{\Delta X_{Cryo}} cov(\delta X_{ID}, \delta X_{Cryo}). \end{aligned} \quad (29)$$

Now the geometry configurations (see Table 10) used for determining each region's energy scale sensitivity are made explicit. For $|\eta| \leq 1.8$:

$$\begin{aligned} \delta\alpha_{tot}^2 = & \left(\delta X_{ID} \frac{\Delta\alpha_A}{\Delta X_A} \right)^2 + \left(\delta X_{Cryo,PS} \frac{\Delta\alpha_{L',X}}{\Delta X_{L',X}} \right)^2 + \left(\delta X_{Calo} \frac{\Delta\alpha_{M,N}}{\Delta X_{M,N}} \right)^2 \\ & + 2 \frac{\Delta\alpha_A}{\Delta X_A} \frac{\Delta\alpha_{L',X}}{\Delta X_{L',X}} cov(\delta X_{ID}, \delta X_{Cryo,PS}), \end{aligned} \quad (30)$$

while for $|\eta| > 1.8$:

$$\begin{aligned} \delta\alpha_{tot}^2 = & \left(\delta X_{ID} \frac{\Delta\alpha_A}{\Delta X_A} \right)^2 + \left(\delta X_{Cryo,L1} \frac{\Delta\alpha_{E',F'}}{\Delta X_{E',F'}} \right)^2 \\ & + 2 \frac{\Delta\alpha_A}{\Delta X_A} \frac{\Delta\alpha_{E',F'}}{\Delta X_{E',F'}} cov(\delta X_{ID}, \delta X_{Cryo,L1}). \end{aligned} \quad (31)$$

From detailed material studies of the inner detector [54], the material there is considered "known" and well described in simulation to within $5\%X_0$. Geometry configuration A differs from the normal geometry by a $5\%X_0$ increase in ID material, so we can take the material uncertainty in the "ID" region as equal to the material difference in configuration A, i.e. $\delta X_{ID} = \Delta X_A$. Considering this relation, and with $cov(\delta X_{ID}, \delta X_{Cryo}) = -\delta X_{ID}^2$, Equations 30 and 31 can be simplified as follows. For $|\eta| \leq 1.8$:

$$\delta\alpha_{tot}^2 = \left(\delta X_{ID} \frac{\Delta\alpha_A}{\Delta X_A} \right)^2 + \left(\delta X_{Cryo,PS} \frac{\Delta\alpha_{L',X}}{\Delta X_{L',X}} \right)^2 + \left(\delta X_{Calo} \frac{\Delta\alpha_{M,N}}{\Delta X_{M,N}} \right)^2 - 2 \frac{\Delta\alpha_A}{\Delta X_A} \frac{\Delta\alpha_{L',X}}{\Delta X_{L',X}} \delta X_{ID}^2, \quad (32)$$

$$\delta\alpha_{tot}^2 = \Delta\alpha_A^2 + \left(\delta X_{Cryo,PS} \frac{\Delta\alpha_{L',X}}{\Delta X_{L',X}} \right)^2 + \left(\delta X_{Calo} \frac{\Delta\alpha_{M,N}}{\Delta X_{M,N}} \right)^2 - 2\Delta\alpha_A \Delta X_A \frac{\Delta\alpha_{L',X}}{\Delta X_{L',X}}. \quad (33)$$

Similarly for $|\eta| > 1.8$:

$$\delta\alpha_{tot}^2 = \left(\delta X_{ID} \frac{\Delta\alpha_A}{\Delta X_A} \right)^2 + \left(\delta X_{Cryo,L1} \frac{\Delta\alpha_{E',F'}}{\Delta X_{E',F'}} \right)^2 - 2 \frac{\Delta\alpha_A}{\Delta X_A} \frac{\Delta\alpha_{E',F'}}{\Delta X_{E',F'}} \delta X_{ID}^2, \quad (34)$$

$$\delta\alpha_{tot}^2 = \Delta\alpha_A^2 + \left(\delta X_{Cryo,L1} \frac{\Delta\alpha_{E',F'}}{\Delta X_{E',F'}} \right)^2 - 2\Delta\alpha_A \Delta X_A \frac{\Delta\alpha_{E',F'}}{\Delta X_{E',F'}}. \quad (35)$$

Before simplifying further, extra notation is required. It is assumed that material in the inner detector is well modelled in simulation (within the $\delta X_{ID} = 5\%X_0$ error mentioned

previously). The measured material differences out to the presampler and first layer of the calorimeter (Figure 46), then, given information about differences in the "Cryo" region. The uncertainty on this measurement must still include the ID material uncertainties (since both are probed by electrons). The "Calo" region is measured independently by the photon studies. Designating the material difference measurements up to the presampler and first layer of the calorimeter as ΔX_{PS} and ΔX_{L1} , respectively, and the material difference in the "Calo" region as measured by photons as ΔX_γ , the material difference measurement ΔX and its uncertainty δX for each region can be summarized as:

$$\begin{aligned}\Delta X_{ID} \pm \delta X_{ID} &= 0 \pm \delta X_{ID}, \\ \Delta X_{Cryo} \pm \delta X_{Cryo} &= \Delta X_{PS} \pm (\delta X_{ID} \oplus \delta X_{PS}) \quad \text{for } |\eta| \leq 1.8, \\ \Delta X_{L1} \pm (\delta X_{ID} \oplus \delta X_{L1}) &\quad \text{for } |\eta| > 1.8, \\ \Delta X_{Calo} \pm \delta X_{Calo} &= \Delta X_\gamma \pm \delta X_\gamma.\end{aligned}\tag{36}$$

The uncertainties from these expressions can be used to further manipulate Equations 33 and 35 into their final forms. Once again, for $|\eta| \leq 1.8$:

$$\delta \alpha_{tot}^2 = \Delta \alpha_A^2 + \left(\delta X_{PS}^2 + \delta X_{ID}^2 \right) \left(\frac{\Delta \alpha_{L',X}}{\Delta X_{L',X}} \right)^2 + \left(\delta X_\gamma \frac{\Delta \alpha_{M,N}}{\Delta X_{M,N}} \right)^2 - 2 \Delta \alpha_A \Delta X_A \frac{\Delta \alpha_{L',X}}{\Delta X_{L',X}},\tag{37}$$

$$\delta \alpha_{tot}^2 = \Delta \alpha_A^2 + \left(\delta X_{ID} \frac{\Delta \alpha_{L',X}}{\Delta X_{L',X}} \right)^2 - 2 \Delta \alpha_A \Delta X_A \frac{\Delta \alpha_{L',X}}{\Delta X_{L',X}} + \left(\delta X_{PS} \frac{\Delta \alpha_{L',X}}{\Delta X_{L',X}} \right)^2 + \left(\delta X_\gamma \frac{\Delta \alpha_{M,N}}{\Delta X_{M,N}} \right)^2,\tag{38}$$

$$\delta \alpha_{tot}^2 = \left(\Delta \alpha_A - \delta X_{ID} \frac{\Delta \alpha_{L',X}}{\Delta X_{L',X}} \right)^2 + \left(\delta X_{PS} \frac{\Delta \alpha_{L',X}}{\Delta X_{L',X}} \right)^2 + \left(\delta X_\gamma \frac{\Delta \alpha_{M,N}}{\Delta X_{M,N}} \right)^2.\tag{39}$$

The same process for $|\eta| > 1.8$ yields:

$$\delta\alpha_{tot}^2 = \left(\Delta\alpha_A - \delta X_{ID} \frac{\Delta\alpha_{E',F'}}{\Delta X_{E',F'}} \right)^2 + \left(\delta X_{PS} \frac{\Delta\alpha_{E',F'}}{\Delta X_{E',F'}} \right)^2 \quad (40)$$

The terms are commonly grouped as follows to give the final, slightly modified definition of each region's contribution to the energy scale uncertainty:

$$\begin{aligned} \delta\alpha_{ID'} &= \Delta\alpha_A - \delta X_{ID} \frac{\Delta\alpha_{L',X(E',F')}}{\Delta X_{L',X(E',F')}}, \\ \delta\alpha_{Cryo'} &= \delta X_{PS(L1)} \frac{\Delta\alpha_{L',X(E',F')}}{\Delta X_{L',X(E',F')}}, \\ \delta\alpha_{Calo} &= \delta X_{\gamma} \frac{\Delta\alpha_{M,N}}{\Delta X_{M,N}}. \end{aligned} \quad (41)$$

These three terms represent the "ID", "Cryo", and "Calo" material contributions to the energy scale uncertainty. The prime notation is used to distinguish these definitions from the similar terms introduced in Equation 28.

4.7.2 Data-Driven Uncertainties

As derived, the ID term $\delta\alpha_{ID'}$ is based entirely on simulation. The material uncertainties δX in the "Cryo" and "Calo" terms are data-driven. The uncertainties are calculated from the uncertainties on difference estimates using the procedure outlined early in Section 4.7.1. (To reiterate an earlier point, δX is used here in an approximative sense to simplify the discussion. The full material uncertainties include a number of additional correlated uncertainties than are not discussed or determined here.) Figures 47 and 49 show δX_{PS} and δX_{L1} , uncertainties calculated from the material difference estimates up to the presampler and first layer of the calorimeter, respectively (Figure 46). Figure 51 gives the uncertainty associated with the calo measurement δX_{γ} as calculated from photons. The uncertainties

as measured are taken as absolute values, regardless of whether the material difference in that $|\eta|$ bin is an excess or deficit.

For ease of comparison with Run 1 results, Figure 48, Figure 50, and Figure 52 are included here showing the final Run 1 material systematic uncertainties (taken from the paper documenting the Run 1 calibration effort [53]). The uncertainties δX_{L1} are comparable in magnitude to the Run 1 results (see Figure 50). Several noticeable features in the graph (like at $|\eta| = 0.6$, or in the crack region) agree well with qualitative features in the Run 1 profile. Deviations from the established uncertainties are reasonably accounted for when considering the set of modifications made to the simulation geometry since that measurement. The measurements making use of the photon estimate, δX_{PS} and δX_{γ} , show a moderate increase due to the larger statistical and fit uncertainties on the estimate (see Figure 48 and Figure 52). The crack region is totally excluded due to limited statistics in this region and difficulties with using configuration G distortions to probe "Calo" material in this part of the detector (see Figure 43). In the absence of fully updated material systematic uncertainties for Run 2 (the work to determine the correlated uncertainties has not been completed yet), these data-driven uncertainty results provide a reassuring indication that detector material remains reasonably well-described (to levels that are mostly compatible with Run 1 uncertainties) in simulation.

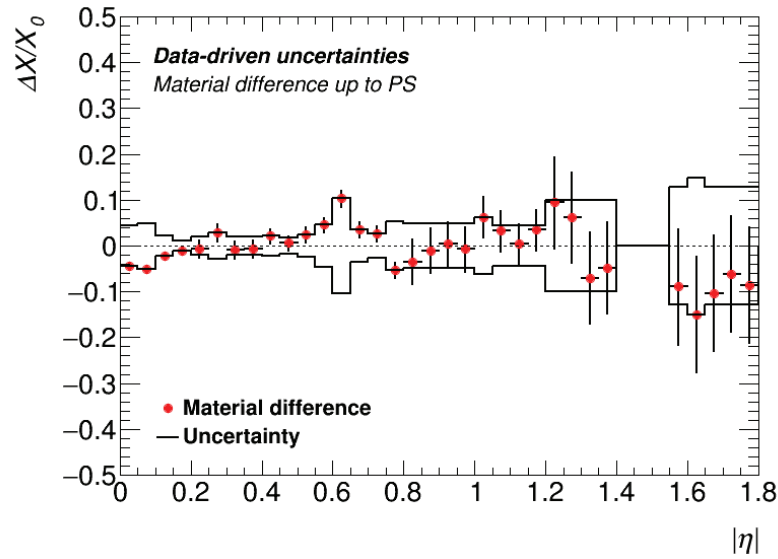


Figure 47: Data-driven uncertainties calculated using the material difference estimate for material up to the presampler. The uncertainty is taken as an absolute value, shown here as a solid black line mirrored about the horizontal axis. These uncertainties contribute to the total material uncertainty δX_{PS} which is used to calculate (using Equation 41) the energy scale uncertainty $\delta\alpha_{Cryo}$ for $|\eta| \leq 1.8$.

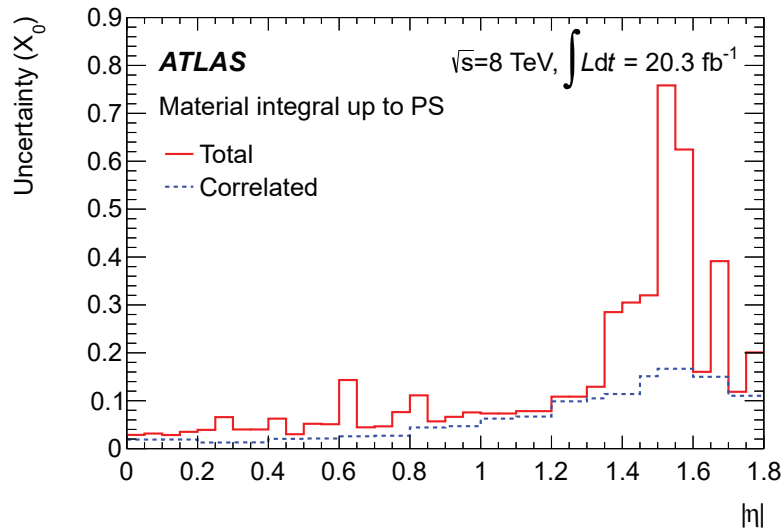


Figure 48: Run 1 material systematic uncertainties for the region up to the presampler, including both correlated and uncorrelated uncertainties. The data-driven (uncorrelated) contribution to the uncertainty can be isolated by taking the difference between the solid red (total) and dashed blue (correlated) lines. Figure 47 shows the data-driven uncertainties as calculated in Run 2. (Plot from [53].)

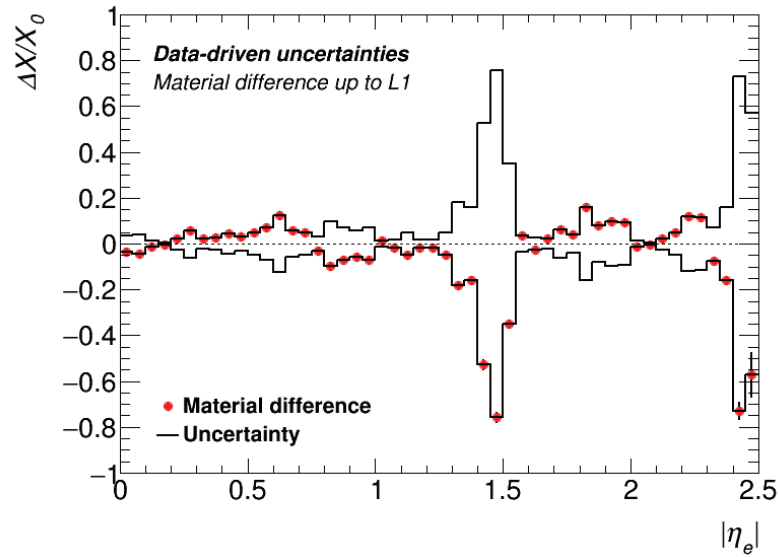


Figure 49: Data-driven uncertainties calculated using the material difference estimate for material up to the first layer of the calorimeter. The uncertainty is taken as an absolute value, shown here as a solid black line mirrored about the horizontal axis. These uncertainties contribute to the total material uncertainty δX_{L1} which is used to calculate (using Equation 41) the energy scale uncertainty $\delta\alpha_{Cryo}$ for $|\eta| > 1.8$.

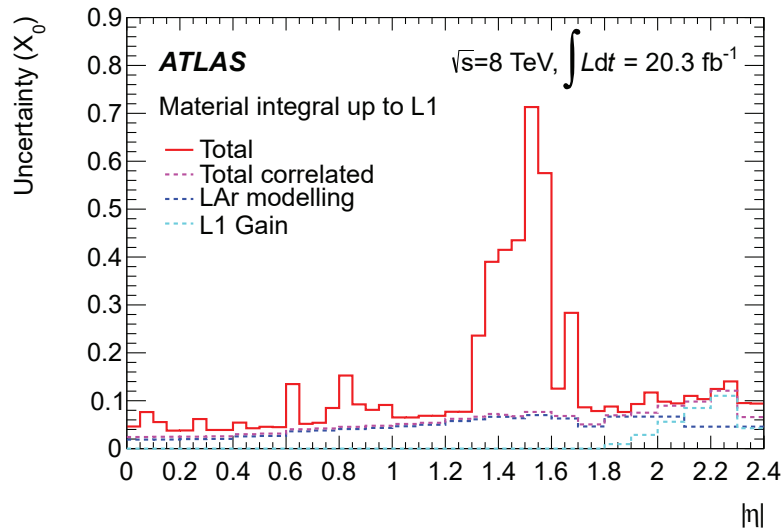


Figure 50: Run 1 material systematic uncertainties for the region up to the first layer of the calorimeter, including both correlated and uncorrelated uncertainties. The data-driven (uncorrelated) contribution to the uncertainty can be isolated by taking the difference between the solid red (total) and dashed pink (total correlated) lines. Figure 49 shows the data-driven uncertainties as calculated in Run 2. (Plot from [53].)

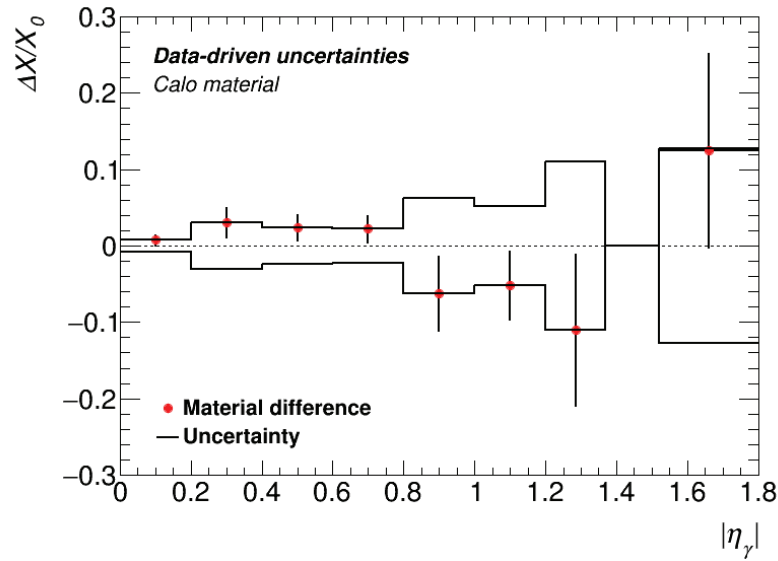


Figure 51: Data-driven uncertainties calculated using the material difference estimate for the region between the presampler and first layer of the EM calorimeter. The uncertainty is taken as an absolute value, shown here as a solid black line mirrored about the horizontal axis. These uncertainties contribute to the total material uncertainty δX_γ which is used to calculate (using Equation 41) the energy scale uncertainty $\delta\alpha_{Calo}$ for $|\eta| \leq 1.8$.

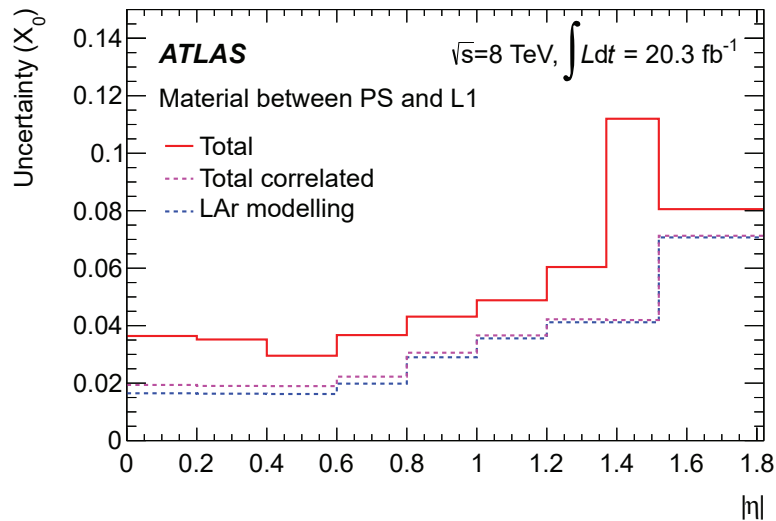


Figure 52: Run 1 material systematic uncertainties for the region between the presampler and the first layer of the calorimeter, including both correlated and uncorrelated uncertainties. The data-driven (uncorrelated) contribution to the uncertainty can be isolated by taking the difference between the solid red (total) and dashed pink (total correlated) lines. Figure 51 shows the data-driven uncertainties as calculated in Run 2. (Plot from [53].)

Summary and conclusions

There is great potential for discovery remaining at the Large Hadron Collider. With several more years of scheduled operation, the LHC is set to continue delivering record-breaking amounts of proton-proton (and heavy ion) collision data at the highest center-of-mass energies yet achieved by a collider. To continue making the most of the collisions produced by the LHC, it is critical that the major detector collaborations continue to not only maintain their detectors, but seek ways of improving them. The ATLAS detector saw a number of improvements during the long-shutdown period between the first and second LHC run periods. Most notably, a new subdetector (the IBL) was added to the inner detector. Since new material was introduced into the detector, the detector geometry in simulation was altered as well. This thesis documents work done to investigate this new simulation geometry, and to quantify the effects that differences in real and simulated geometry have on the energy scale calibration of electrons and photons. Specifically, the investigation is limited to the detector material in the precision-measurement region between the beam-line and electromagnetic calorimeter.

The ratio of energies deposited in the first and second layers of the electromagnetic calorimeter ($E_{1/2}$) was used as the main probe in the analysis. Electrons and photons from 2015-2016 proton-proton collision data and nominal-geometry Monte Carlo simulations were used to create profile distributions of mean $E_{1/2}$ values in bins of $|\eta|$. Using simulation geometries with extra material added, a sensitivity curve was built to quantitatively describe how $E_{1/2}$ varies with differences in detector material. This sensitivity curve was used with

the $E_{1/2} |\eta|$ profile distributions to estimate the material differences between data and nominal-geometry simulation.

The material difference results from electrons were compared with previous studies done in Run 1. The results from the Run 2 estimation fell within the systematic uncertainties of the previous measurement except in regions where significant amounts of material were added to the detector in Run 2. A check was performed using a model of additional Run 2 material uncertainties. The additional uncertainties proved successful in covering the measured material differences in regions with new material, confirming their validity as a model of new Run 2 systematic uncertainties. This check was used to confirm the reasonable applicability of existing Run 1 material systematic uncertainties to Run 2 results, just as long as they are used in addition to the new Run 2 uncertainties.

Exploratory studies investigating asymmetries in ϕ were used to identify a possible detector support structure that is missing from the simulated detector geometry. At the time of the analysis, several energy calibrations were determined only as a function of η (not ϕ), so the study as-is should be interpreted as a mostly qualitative search. A rigorous check for simulation material discrepancies in ϕ has not been performed, so this should be considered for future material studies work.

Following the technique used in Run 1, photons were used in an effort to divide the area before the calorimeter into two distinct regions (from the beam-line to the presampler, and from the presampler to the first layer of the EM calorimeter). The photon analysis showed statistically significant discrepancies in material in the region between the presampler and accordion calorimeter, but the two regions could not be probed with the same degree of precision as in Run 1. Further work and more data (including additional Monte Carlo simulations) are required to reduce the uncertainties on this measurement in Run 2.

Finally, the passive material estimates are used to calculate the contributions of Run 2 data-driven material uncertainties to the systematic uncertainty on the total energy scale α . The calculated uncertainties are found to be comparable to the Run 1 values.

Results presented in this thesis were used to provide recommendations on energy calibration systematic uncertainties for the ATLAS physics analyses targeting high-energy physics summer 2017 conferences. A publication is underway to document several aspects of the current Run 2 electron and photon calibration efforts, including this work.

Appendix

A.1 Discriminating Variables

Tables 11 and 12 summarize the discriminating variables used in photon and electron (respectively) identification. The likelihood identification technique is summarized in Section 3.2.

Table 11: Discriminating variables used used in photon likelihood identification. Table modified from [52].

Category	Description	Name
Acceptance	$ \eta < 2.37$, with $1.37 < \eta < 1.52$ excluded	–
Hadronic leakage	Ratio of E_T in the first sampling layer of the hadronic calorimeter to E_T of the EM cluster (used over the range $ \eta < 0.8$ or $ \eta > 1.37$)	R_{Had1}
	Ratio of E_T in the hadronic calorimeter to E_T of the EM cluster (used over the range $0.8 < \eta < 1.37$)	R_{Had}
EM middle layer	Ratio of $3 \times 7 \eta \times \phi$ to 7×7 cell energies	R_η
	Lateral width of the shower	$w_{\eta 2}$
	Ratio of $3 \times 3 \eta \times \phi$ to 3×7 cell energies	R_ϕ
EM strip layer	Shower width calculated from three strips around the strip with maximum energy deposit	w_{s3}
	Total lateral shower width	w_{stot}
	Energy outside the core of the three central strips but within seven strips divided by energy within the three central strips	F_{side}
	Difference between the energy associated with the second maximum in the strip layer and the energy reconstructed in the strip with the minimum value found between the first and second maxima	ΔE
	Ratio of the energy difference associated with the largest and second largest energy deposits to the sum of these energies	E_{ratio}

Table 12: Discriminating variables used in electron likelihood identification. Table from [51].

Type	Description	Name
Hadronic leakage	Ratio of E_T in the first layer of the hadronic calorimeter to E_T of the EM cluster (used over the range $ \eta < 0.8$ or $ \eta > 1.37$)	R_{Had1}
	Ratio of E_T in the hadronic calorimeter to E_T of the EM cluster (used over the range $0.8 < \eta < 1.37$)	R_{Had}
Back layer of EM calorimeter	Ratio of the energy in the back layer to the total energy in the EM accordion calorimeter	f_3
Middle layer of EM calorimeter	Lateral shower width, $\sqrt{(\sum E_i \eta_i^2)/(\sum E_i) - ((\sum E_i \eta_i)/(\sum E_i))^2}$, where E_i is the energy and η_i is the pseudorapidity of cell i and the sum is calculated within a window of 3×5 cells	$w_{\eta 2}$
	Ratio of the energy in 3×3 cells to the energy in 3×7 cells centred at the electron cluster position	R_ϕ
	Ratio of the energy in 3×7 cells to the energy in 7×7 cells centred at the electron cluster position	R_η
Strip layer of EM calorimeter	Shower width, $\sqrt{(\sum E_i (i - i_{\text{max}})^2)/(\sum E_i)}$, where i runs over all strips in a window of $\Delta\eta \times \Delta\phi \approx 0.0625 \times 0.2$, corresponding typically to 20 strips in η , and i_{max} is the index of the highest-energy strip	w_{stot}
	Ratio of the energy difference between the maximum energy deposit and the energy deposit in a secondary maximum in the cluster to the sum of these energies	E_{ratio}
	Ratio of the energy in the strip layer to the total energy in the EM accordion calorimeter	f_1
Track quality	Number of hits in the b-layer (discriminates against photon conversions)	n_{Blayer}
	Number of hits in the pixel detector	n_{Pixel}
	Total number of hits in the pixel and SCT detectors	n_{Si}
	Transverse impact parameter	d_0
	Significance of transverse impact parameter defined as the ratio of the magnitude of d_0 to its uncertainty	d_0/σ_{d_0}
	Momentum lost by the track between the perigee and the last measurement point divided by the original momentum	$\Delta p/p$
TRT	Likelihood probability based on transition radiation in the TRT	eProbabilityHT
Track-cluster matching	$\Delta\eta$ between the cluster position in the strip layer and the extrapolated track	$\Delta\eta_1$
	$\Delta\phi$ between the cluster position in the middle layer and the extrapolated track	$\Delta\phi_2$
	Defined as $\Delta\phi_2$, but the track momentum is rescaled to the cluster energy before extrapolating the track to the middle layer of the calorimeter	$\Delta\phi_{\text{res}}$
	Ratio of the cluster energy to the track momentum	E/p

A.2 Distorted Geometry Schematics

Figures 53 – 57 show the ATLAS inner detector (without IBL), highlighting the approximate locations (in blue) where extra material is added in the distorted geometries used to generate the $E_{1/2}$ sensitivity curves. The base schematic (from [2]) does not extend out to the presampler, so configurations with extra material between the presampler and first layer of the electromagnetic calorimeter (configuration N in Figure 54 and configuration M in Figure 57) are represented by highlights along the outer edge of the diagram. The distorted geometries are summarized in Table 6.

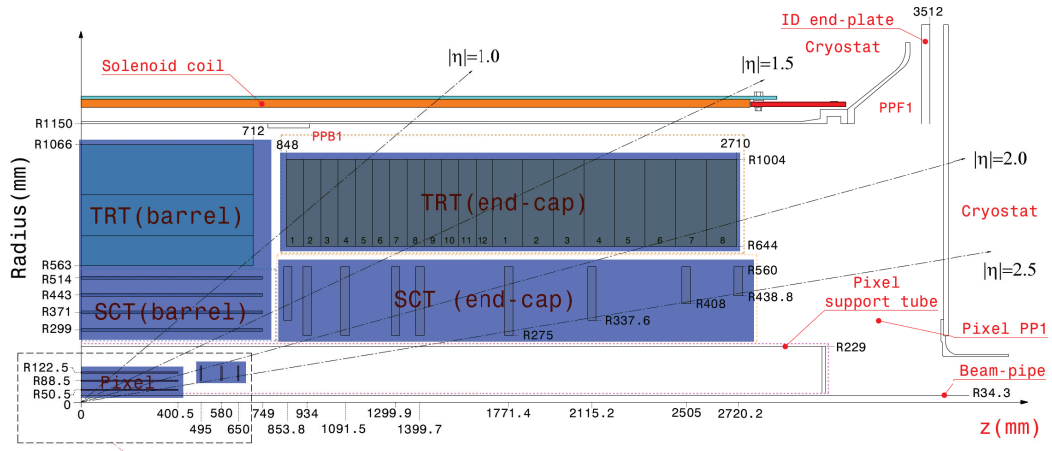


Figure 53: Extra material added in the distorted geometry with s-tag **s2763**. The configuration used in this distorted geometry is **Config. A** (5% scale increase to entire inner detector).

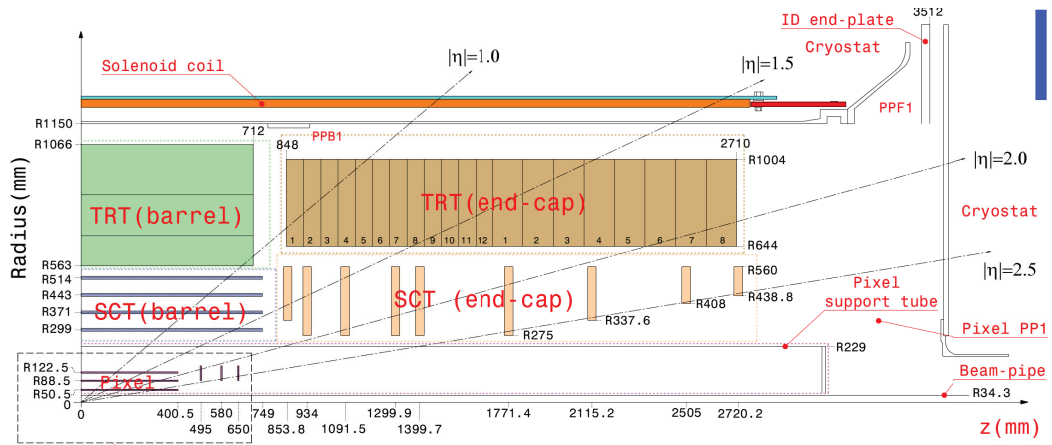


Figure 54: Extra material added in the distorted geometry with s-tag **s2764**. The configuration used in this distorted geometry is **Config. N** (+5% X_0 between the presampler and layer 1 in the end-cap region).

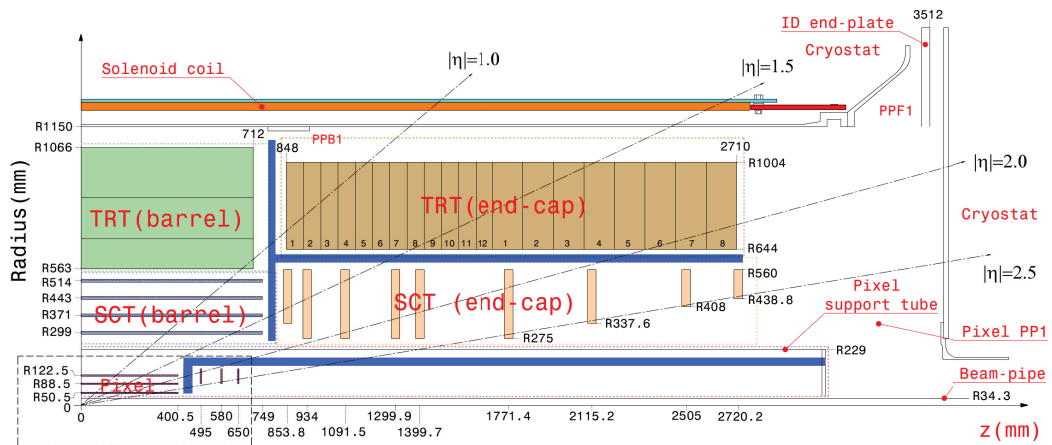


Figure 55: Extra material added in the distorted geometry with s-tag **s2765**. Configurations used in this distorted geometry are: **Config. C'** (+10% X_0 to pixel (and IBL) services) and **Config. D'** (+10% X_0 to SCT services).

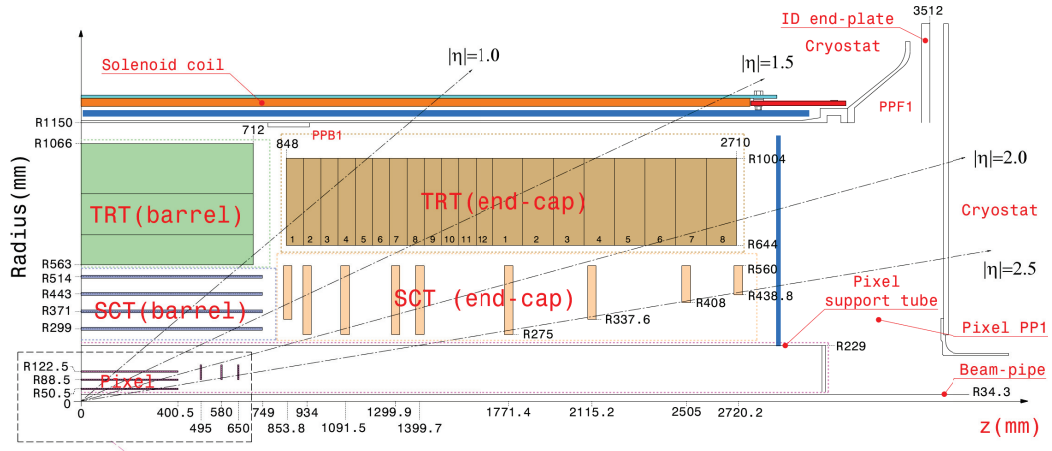


Figure 56: Extra material added in the distorted geometry with s-tag **s2766**. Configurations used in this distorted geometry are: **Config. E'** (+7.5% X_0 to SCT/TRT end-cap) and **Config. L'** (+5% X_0 to cryostat in barrel region.).

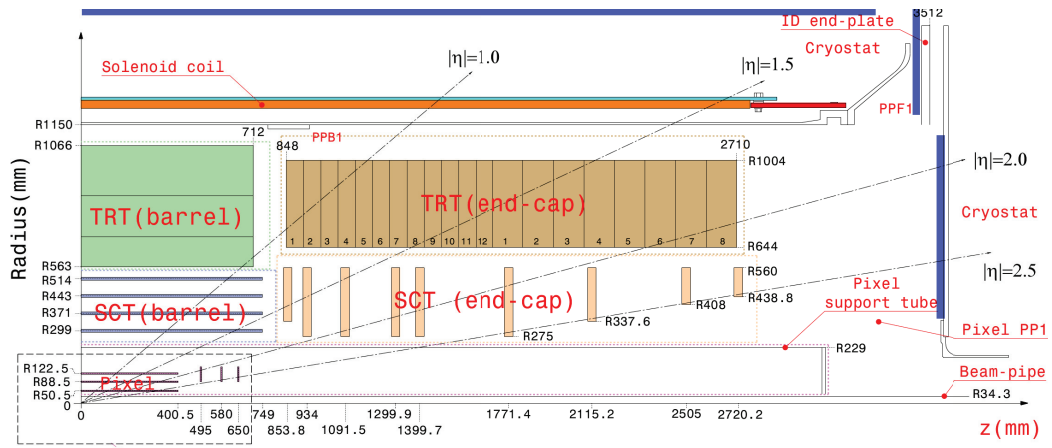


Figure 57: Extra material added in the distorted geometry with s-tag **s2767**. Configurations used in this distorted geometry are: **Config. F'** (+7.5% X_0 to inner detector endplate), **Config. M** (+5% X_0 between the presampler and layer 1 in the barrel region), and **Config. X** (+30% X_0 in the calorimeter end-cap region).

A.3 Distorted Geometry $E_{1/2}$ Profiles

Five distorted geometries (with s-tags s2763 – s2767, see Table 6) were used to calculate the electron $E_{1/2}$ sensitivity curve shown in Figure 35. The process of calculating the sensitivity for a given distorted geometry began by building a profile distribution of $E_{1/2}$ using the distorted geometry. For each bin in $|\eta|$, the relative difference was taken between the distorted and nominal simulation distributions (Equation 24). This relative difference were divided into the change in material associated with the distorted geometry (see the plots in Figure 30), yielding the sensitivity (Equation 25). Figures 58 – 62 show the $E_{1/2}$ (or "E1/E2" here) profile distributions calculated for each of the distorted geometries in comparison with the profile distribution calculated for the nominal geometry (identified here by s-tag: s2576). The bottom plot in each figure shows the relative difference between distorted and normal distributions.

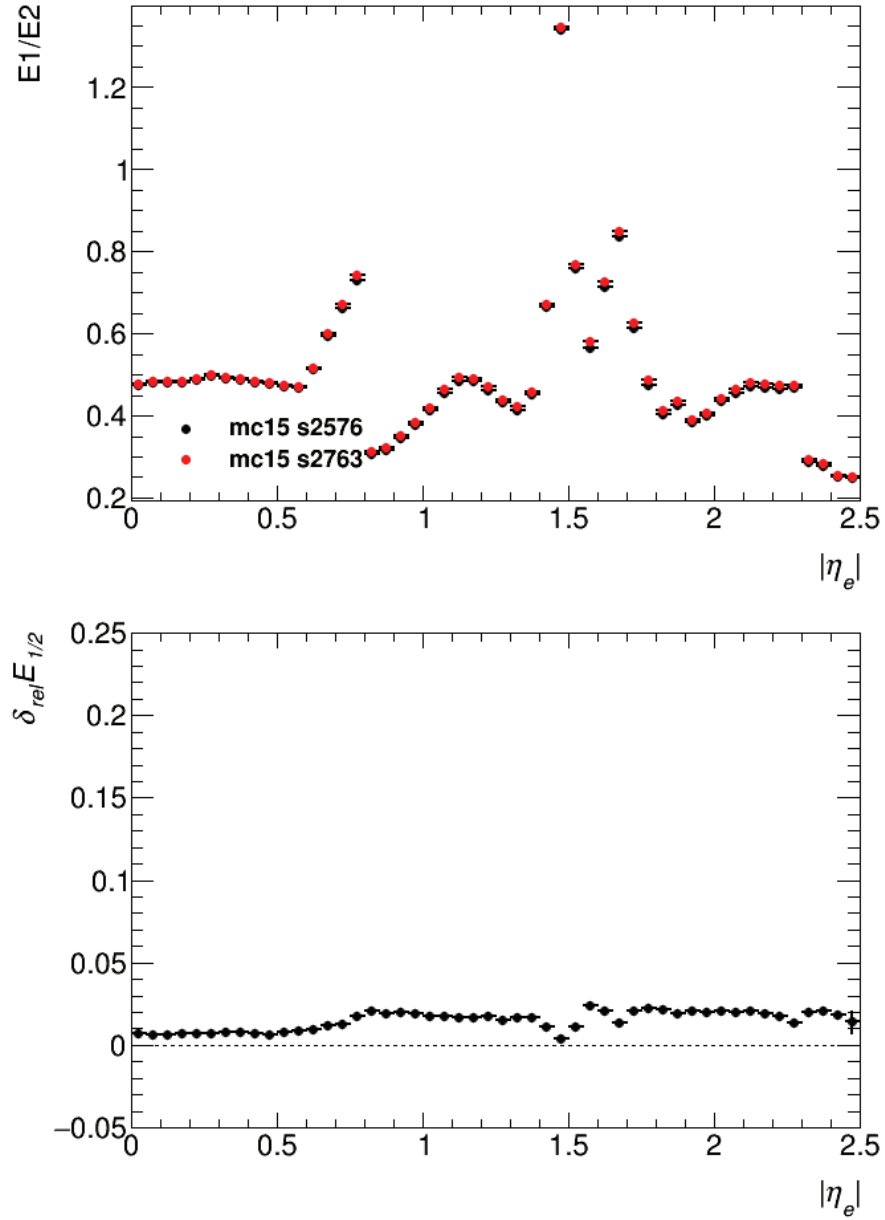


Figure 58: **Top:** $E_{1/2}$ profile distributions calculated for the distorted geometry (red points) with s-tag 2763 shown in comparison with the profile distribution calculated for the nominal geometry (black points) identified here by s-tag 2576. **Bottom:** Relative difference between distributions (calculated using Equation 24).

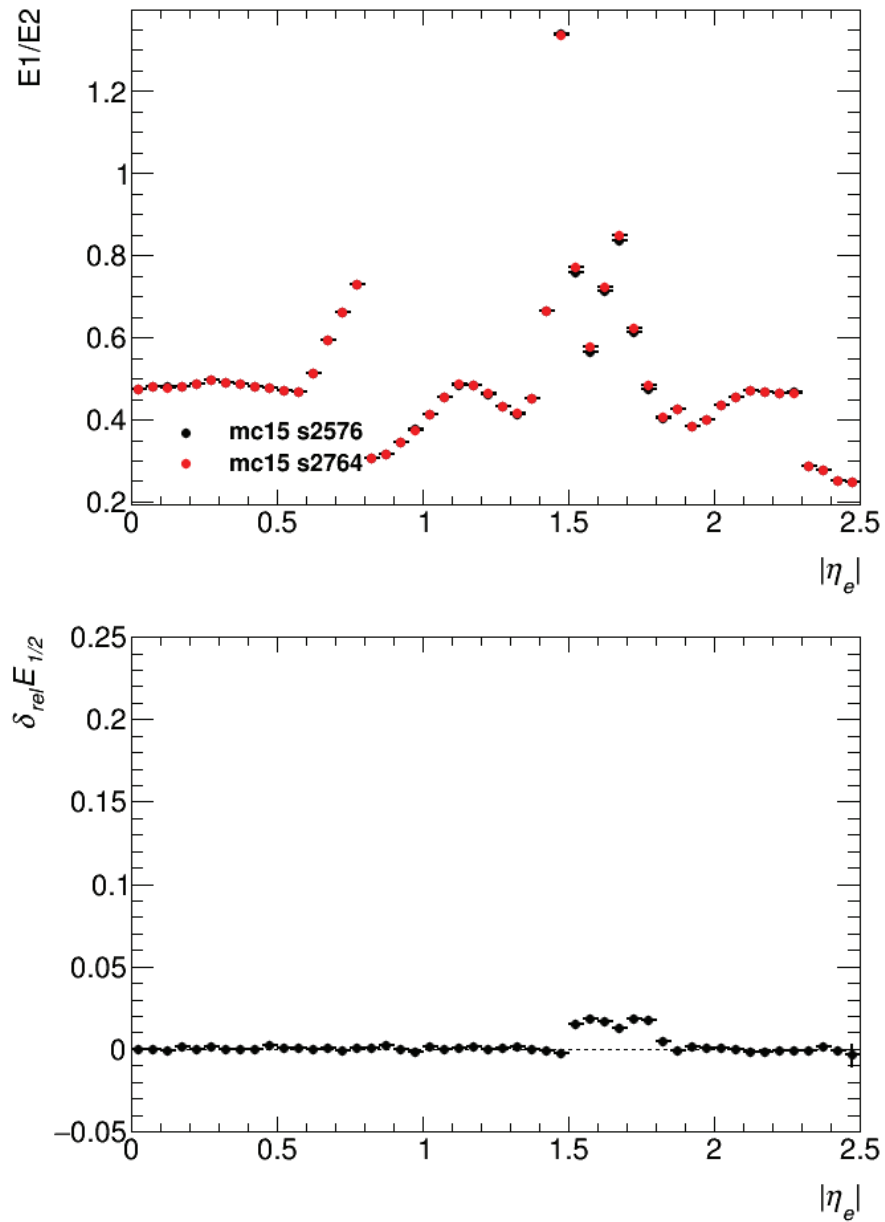


Figure 59: **Top:** $E_{1/2}$ profile distributions calculated for the distorted geometry (red points) with s-tag 2764 shown in comparison with the profile distribution calculated for the nominal geometry (black points) identified here by s-tag 2576. **Bottom:** Relative difference between distributions (calculated using Equation 24).

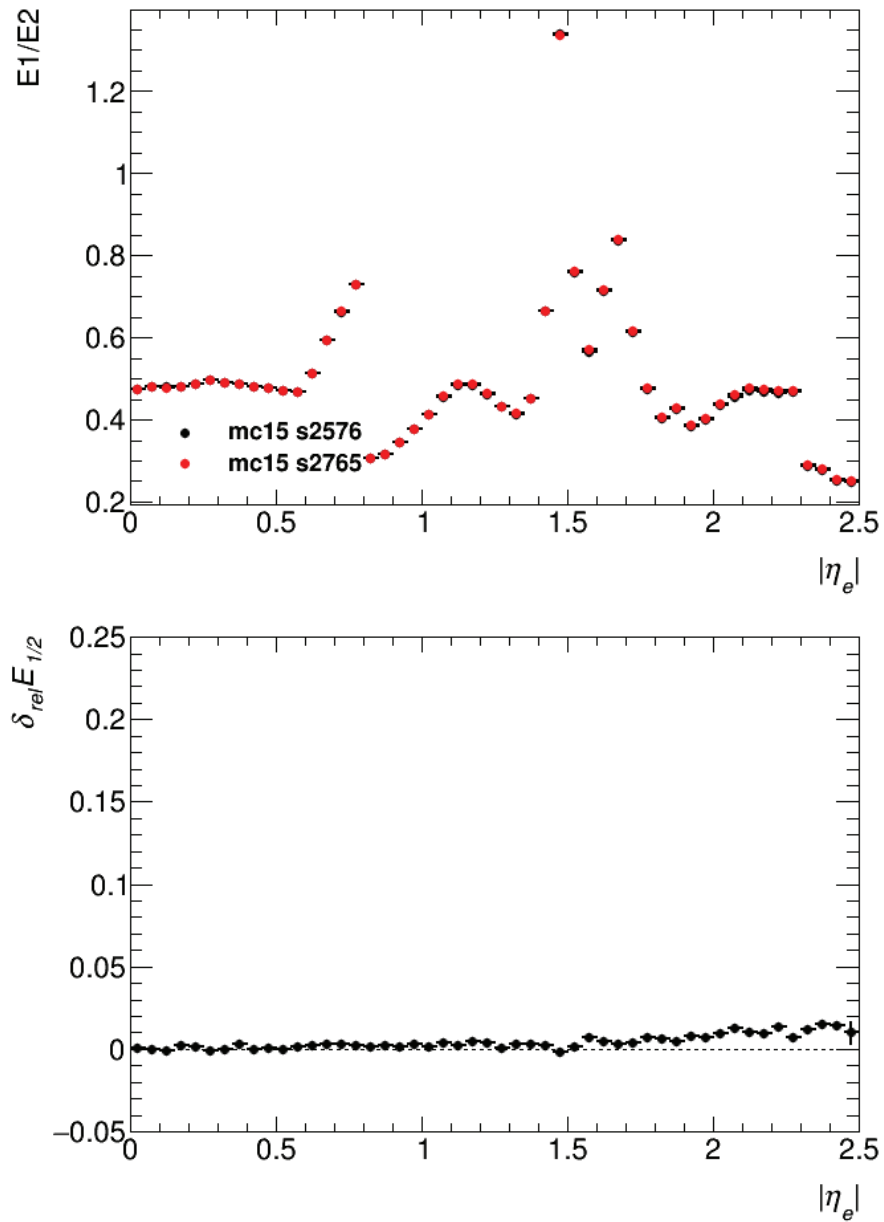


Figure 60: **Top:** $E_{1/2}$ profile distributions calculated for the distorted geometry (red points) with s-tag 2765 shown in comparison with the profile distribution calculated for the nominal geometry (black points) identified here by s-tag 2576. **Bottom:** Relative difference between distributions (calculated using Equation 24).

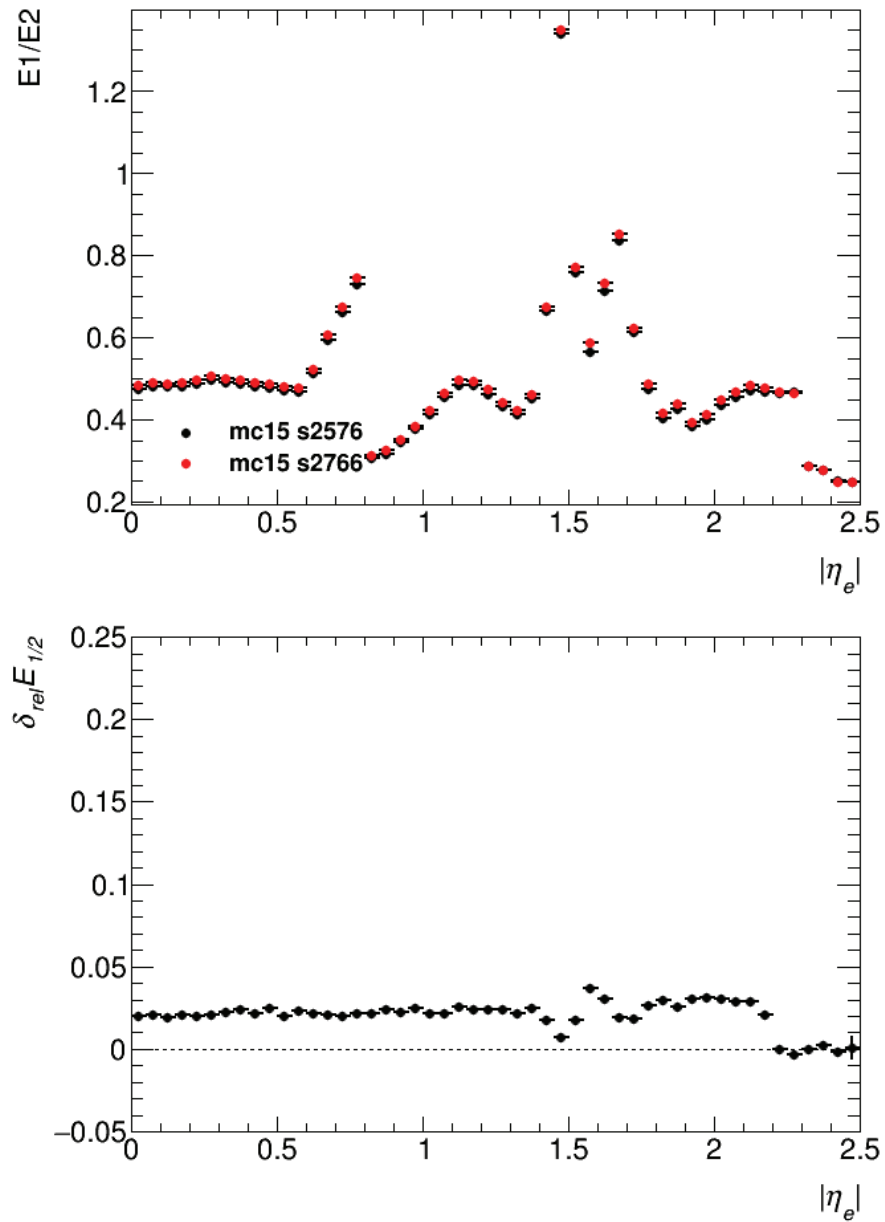


Figure 61: **Top:** $E_{1/2}$ profile distributions calculated for the distorted geometry (red points) with s-tag 2766 shown in comparison with the profile distribution calculated for the nominal geometry (black points) identified here by s-tag 2576. **Bottom:** Relative difference between distributions (calculated using Equation 24).

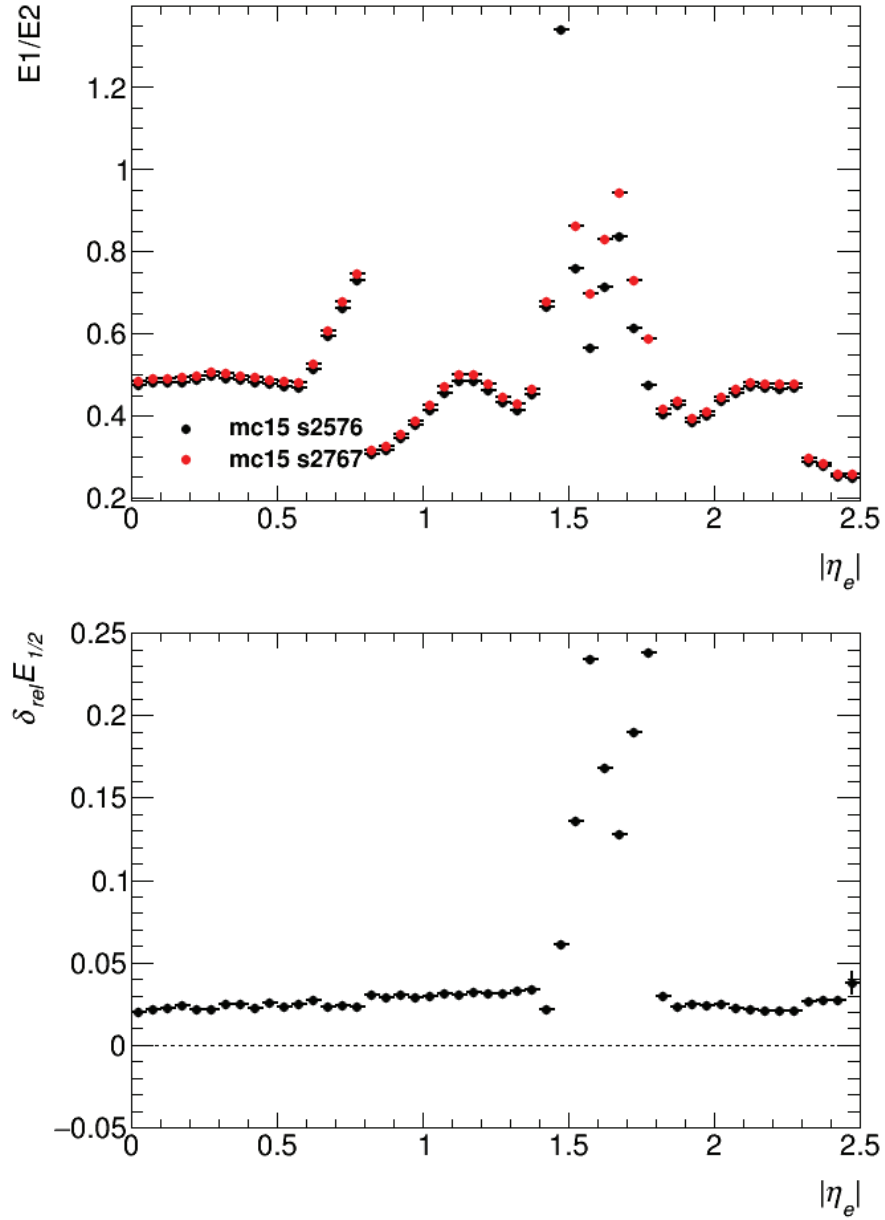


Figure 62: **Top:** $E_{1/2}$ profile distributions calculated for the distorted geometry (red points) with s-tag 2767 shown in comparison with the profile distribution calculated for the nominal geometry (black points) identified here by s-tag 2576. **Bottom:** Relative difference between distributions (calculated using Equation 24).

References

- [1] S. Falke, *Electron and photon energy calibration with the ATLAS detector*, (2017),
URL: <http://cds.cern.ch/record/2274069>.
- [2] ATLAS Collaboration,
The ATLAS Experiment at the CERN Large Hadron Collider,
[JINST 3 \(2008\) S08003](#).
- [3] L. Evans and P. Bryant, *LHC Machine*, *Journal of Instrumentation* **3** (2008) S08001.
- [4] P. W. Higgs, *Broken Symmetries and the Masses of Gauge Bosons*,
Phys. Rev. Lett. **13** (1964) 508.
- [5] F. Englert and R. Brout, *Broken Symmetry and the Mass of Gauge Vector Mesons*,
Phys. Rev. Lett. **13** (1964) 321.
- [6] ATLAS Collaboration, *Observation of a new particle in the search for the Standard Model Higgs boson with the ATLAS detector at the LHC*,
Phys. Lett. B **716** (2012) 1, arXiv: [1207.7214 \[hep-ex\]](#).
- [7] CMS Collaboration, *Observation of a new boson at a mass of 125 GeV with the CMS experiment at the LHC*, *Phys. Lett. B* **716** (2012) 30,
arXiv: [1207.7235 \[hep-ex\]](#).
- [8] M. Boonekamp, O. Fedin, D. Froidevaux and G. Unal,
'Passive material determination using electrons and photons',
ATL-COM-PHYS-2013-1644, ATLAS Internal Note, 2013,
URL: <https://cds.cern.ch/record/1636887>.
- [9] D. J. Griffiths, *Introduction to electrodynamics*, 4th ed., Pearson, 2013.
- [10] *The quantum theory of the electron*, *Proceedings of the Royal Society of London A: Mathematical, Physical and Engineering Sciences* **117** (1928) 610.

-
- [11] *Quantised singularities in the electromagnetic field*,
Proceedings of the Royal Society of London A: Mathematical, Physical and
Engineering Sciences **133** (1931) 60.
- [12] C. D. Anderson, *The Positive Electron*, *Phys. Rev.* **43** (1933) 491.
- [13] G. Zweig,
An SU(3) model for strong interaction symmetry and its breaking. Version 2,
Developments in the Quark Theory of Hadrons, Volume 1. Edited by D. Lichtenberg
and S. Rosen. pp. 22-101 (1964) 22, ed. by D. Lichtenberg and S. P. Rosen.
- [14] M. Gell-Mann, *A schematic model of baryons and mesons*,
Physics Letters **8** (1964) 214.
- [15] C. Patrignani et al., *Review of Particle Physics*, *Chin. Phys. C* **40** (2016) 100001.
- [16] C. de Rham, *Massive Gravity*, *Living Rev. Rel.* **17** (2014) 7,
arXiv: [1401.4173 \[hep-th\]](https://arxiv.org/abs/1401.4173).
- [17] K. Hinterbichler, *Theoretical Aspects of Massive Gravity*,
Rev. Mod. Phys. **84** (2012) 671, arXiv: [1105.3735 \[hep-th\]](https://arxiv.org/abs/1105.3735).
- [18] M. E. Peskin and D. V. Schroeder, *An Introduction to quantum field theory*,
Addison-Wesley, 1995, ISBN: 9780201503975, 0201503972.
- [19] W. N. Cottingham and D. A. Greenwood,
An introduction to the standard model of particle physics,
Cambridge Univ. Press, 1998.
- [20] R. C. Fernow, *Introduction to Experimental Particle Physics*, 1st ed.,
Cambridge University Press, 1986.
- [21] R. Assmann, M. Lamont and S. Myers, *A brief history of the LEP collider*,
Nuclear Physics B - Proceedings Supplements **109** (2002) 17, Proceedings of the
7th Topical Seminar.

-
- [22] H. T. Edwards, *The Tevatron Energy Doubler: A Superconducting Accelerator*, *Annual Review of Nuclear and Particle Science* **35** (1985) 605.
- [23] CMS Collaboration, *The CMS Experiment at the CERN LHC*, *JINST* **3** (2008) S08004.
- [24] LHCb Collaboration, *The LHCb Detector at the LHC*, *JINST* **3** (2008) S08005.
- [25] ALICE Collaboration, *The ALICE experiment at the CERN LHC*, *JINST* **3** (2008) S08002.
- [26] ‘ATLAS Public Run 2 Luminosity Results’, Obtained on November 04, 2017, URL: <https://twiki.cern.ch/twiki/bin/view/AtlasPublic/LuminosityPublicResultsRun2>.
- [27] A. R. Martínez, *The Run-2 ATLAS Trigger System*, *J. Phys. Conf. Ser.* **762** (2016) 012003.
- [28] ATLAS Collaboration, *Performance of the ATLAS Trigger System in 2015*, (2016), arXiv: [1611.09661](https://arxiv.org/abs/1611.09661) [hep-ex].
- [29] Z. Marshall and the ATLAS Collaboration, *Simulation of Pile-up in the ATLAS Experiment*, *Journal of Physics: Conference Series* **513** (2014) 022024.
- [30] ATLAS Collaboration, *Topological cell clustering in the ATLAS calorimeters and its performance in LHC Run 1*, *Eur. Phys. J. C* **77** (2017) 490, arXiv: [1603.02934](https://arxiv.org/abs/1603.02934) [hep-ex].
- [31] ATLAS Collaborations, *The ATLAS Simulation Infrastructure*, *Eur. Phys. J. C* **70** (2010) 823, arXiv: [1005.4568](https://arxiv.org/abs/1005.4568) [physics.ins-det].
- [32] S. Agostinelli et al., *Geant4—a simulation toolkit*, *Nuclear Instruments and Methods in Physics Research Section A: Accelerators, Spectrometers, Detectors and Associated Equipment* **506** (2003) 250 .

-
- [33] J. M. Campbell, J. W. Huston and W. J. Stirling,
Hard Interactions of Quarks and Gluons: A Primer for LHC Physics,
Rept. Prog. Phys. **70** (2007) 89, arXiv: [hep-ph/0611148](#) [[hep-ph](#)].
- [34] M. Backhaus, *The upgraded Pixel Detector of the ATLAS Experiment for Run 2 at the Large Hadron Collider*, *Nuclear Instruments and Methods in Physics Research Section A: Accelerators, Spectrometers, Detectors and Associated Equipment* **831** (2016) 65, Proceedings of the 10th International “Hiroshima” Symposium on the Development and Application of Semiconductor Tracking Detectors.
- [35] ATLAS Collaboration, *The ATLAS Inner Detector commissioning and calibration*, *Eur. Phys. J. C* **70** (2010) 787, arXiv: [1004.5293](#) [[hep-ex](#)].
- [36] C. Grupen and B. Shwartz, *Particle Detectors*, 2nd ed.,
Cambridge University Press, 2008.
- [37] E. Hines, ‘Performance of Particle Identification with the ATLAS Transition Radiation Tracker’, *Particles and fields. Proceedings, Meeting of the Division of the American Physical Society, DPF 2011, Providence, USA, August 9-13, 2011*, 2011, arXiv: [1109.5925](#) [[physics.ins-det](#)].
- [38] ATLAS Electromagnetic Liquid Argon Endcap Calorimeter Group, *Construction, assembly and tests of the ATLAS electromagnetic end-cap calorimeters*, *Journal of Instrumentation* **3** (2008) P06002.
- [39] ATLAS Collaboration, *Measurement of the Higgs boson mass from the $H \rightarrow \gamma\gamma$ and $H \rightarrow ZZ^* \rightarrow 4\ell$ channels in pp collisions at center-of-mass energies of 7 and 8 TeV with the ATLAS detector*, *Phys. Rev. D* **90** (2014) 052004, arXiv: [1406.3827](#) [[hep-ex](#)].
- [40] ATLAS Collaboration, *ATLAS liquid argon calorimeter: Technical design report*, (1996), CERN-LHCC-96-41.

-
- [41] J. D. Jackson, *Classical Electrodynamics*, 3rd ed., Wiley, 1998.
- [42] D. Green, *The Physics of Particle Detectors*, 1st ed., Cambridge University Press, 2000.
- [43] H. Bethe and W. Heitler,
On the Stopping of Fast Particles and on the Creation of Positive Electrons,
Proceedings of the Royal Society of London. Series A, Containing Papers of a
Mathematical and Physical Character **146** (1934) 83,
URL: <http://www.jstor.org/stable/2935479>.
- [44] S. Klein,
Suppression of bremsstrahlung and pair production due to environmental factors,
Rev. Mod. Phys. **71** (1999) 1501.
- [45] L. Gerhardt and S. R. Klein, *Electron and photon interactions in the regime of
strong Landau-Pomeranchuk-Migdal suppression*, *Phys. Rev. D* **82** (2010) 074017.
- [46] A. F. Bielajew, H. Hirayama, W. R. Nelson and D. W. O. Rogers,
'History, overview and recent improvements of EGS4', *Conference on Radiation
Transport Calculations Using the EGS4 Capri, Italy, June 28-July 1, 1994*, 1994.
- [47] W. Lampl et al., *Calorimeter clustering algorithms: Description and performance*,
(2008), ATL-LARG-PUB-2008-002, ATL-COM-LARG-2008-003.
- [48] ATLAS Collaboration, *Performance of the ATLAS Track Reconstruction Algorithms
in Dense Environments in LHC run 2*, (2017), arXiv: [1704.07983](https://arxiv.org/abs/1704.07983) [hep-ex].
- [49] ATLAS Collaboration, *Electron efficiency measurements with the ATLAS detector
using 2012 LHC proton-proton collision data*, (2016),
arXiv: [1612.01456](https://arxiv.org/abs/1612.01456) [hep-ex].
- [50] T. G. Cornelissen et al., *The global χ^2 track fitter in ATLAS*,
J. Phys. Conf. Ser. **119** (2008) 032013.

-
- [51] ATLAS Collaboration, *Electron efficiency measurements with the ATLAS detector using the 2015 LHC proton-proton collision data*, ATLAS-CONF-2016-024, 2016.
- [52] ATLAS Collaboration, *Measurement of the photon identification efficiencies with the ATLAS detector using LHC Run-1 data*, (2016), arXiv: [1606.01813 \[hep-ex\]](#).
- [53] ATLAS Collaboration, *Electron and photon energy calibration with the ATLAS detector using LHC Run 1 data*, *Eur. Phys. J. C* **74** (2014) 3071, arXiv: [1407.5063 \[hep-ex\]](#).
- [54] ATLAS Collaboration, *Study of the material of the ATLAS inner detector for Run 2 of the LHC*, (2017), arXiv: [1707.02826 \[hep-ex\]](#).
- [55] K. Whalen, ‘Study of Extra Material in Front of the ATLAS Electromagnetic Barrel Calorimeter using High- p_T Electrons’, MSc Thesis: Carleton University, 2009, URL: <https://curve.carleton.ca/e32c46a2-91f4-4ec7-a829-fac86d4b915e>.

"...never fixed, nor stable, but always just a passing, temporary energy-burst."

— George Saunders (as Abraham Lincoln as experienced by
the ghost of Hans Vollman), *Lincoln in the Bardo*